The Dissertation Committee for Longjun Li Certifies that this is the approved version of the following dissertation:

HIGH-PERFORMANCE HYBRID LITHIUM-AIR BATTERIES: FROM BATTERY DESIGN TO CATALYSTS

Committee:

Arumugam Manthiram, Supervisor

John B. Goodenough

Charles Buddie Mullins

Paulo J. Ferreira

Donglei Fan

HIGH-PERFORMANCE HYBRID LITHIUM-AIR BATTERIES: FROM BATTERY DESIGN TO CATALYSTS

by

Longjun Li, B.E.

Dissertation

Presented to the Faculty of the Graduate School of

The University of Texas at Austin

in Partial Fulfillment

of the Requirements

for the Degree of

Doctor of Philosophy

The University of Texas at Austin

May, 2014

Dedication

Dedicated to my beloved Zu and family

Acknowledgements

Foremost, I would like to convey my sincere gratitude to my supervisor, professor Arumugam Manthiram for his continuous support and guidance through the course of my study and research. This project was a new project and underwent a lot of difficulties at the initial stages. Professor Manthiram provided all kinds of resources to help me go through the hardest time and develop this project successfully. In addition, I would like to thank my committee members, Professor John B. Goodenough, Charles Buddie Mullins, Paulo J. Ferreira, and Donglei Fan, for kindly serving on my committee and providing useful suggestions during my preliminary oral examination.

I am grateful to many people who have provided assistance in building the hybrid lithium-air battery. Professor Goodenough and Dr. Yuhao Lu were very kind to let me learn from the protected lithium anode in their Li^+-ion cathode-flow battery. Dr. Xinsheng Zhao was always there to provide help when I faced difficulties. He introduced me to fuel cells and catalysis, which are the basis of hybrid lithium-air batteries. Dr. Yongzhu Fu was a great mentor in the lab. I learned a lot from him. He also polished many of my manuscripts. I would also like to thank former and current members in the group, specially Dr. Wei Li, Dr. Thomas Cochell, Dr. Zhongqing Jiang, Dr. Zicheng Zuo, Dr. Guang He, Dr. Yu-Sheng Su, James Knight, Dr. Katharine Chemelewski, Dr. Il Tae Kim, Dr. Veronica Augustyn for their kind help and support. Additionally, I would like to thank the financial support by the U.S. Department of Energy, Office of Basic Energy Sciences, Division of Materials Science and Engineering.

Above all, I feel lucky to have my beloved Zu and family for their infinite love and support, which grant me the strength to overcome all kinds of difficulties.

HIGH-PERFORMANCE HYBRID LITHIUM-AIR BATTERIES: FROM BATTERY DESIGN TO CATALYSTS

Longjun Li, Ph.D.

The University of Texas at Austin, 2014

Supervisor: Arumugam Manthiram

Growing environmental concerns and increasing demand for energy have stimulated extensive interest in electrical energy storage. Li-air batteries are appealing in this regard as they offer much higher energy density than the current Li-ion batteries, but the nonaqueous Li-air batteries suffer from poor cycle life arising from electrolyte decomposition and clogging of the air electrode by insoluble discharge products. Interestingly, hybrid Li-air batteries in which a solid electrolyte separates the lithium-metal anode in an aprotic electrolyte from the air electrode in an aqueous catholyte could overcome these problems. Lots of efforts have been made on developing efficient bifunctional catalysts to lower the overpotential and improve the stability of hybrid Li-air batteries, but the cycle life is still limited. This dissertation focuses on the development of advanced cell configurations and high-performance catalysts for hybrid Li-air batteries.

First, a buffer catholyte solution with a moderate pH, based on phosphoric acid and supporting salts, has been developed to keep the solid electrolyte stable and reduce the internal resistance and overpotential. With a high operating voltage and the utilization of all the three protons of phosphoric acid, the buffer catholyte enables a Li-air cell with high energy density. Further increase in power density has been realized by increasing the solid-electrolyte conductivity and operating temperature to 40 ^{o}C.

The biggest challenge with Li-air cells is the large overpotentials associated with the oxygen reduction reaction (ORR) and oxygen evolution reaction (OER). Noble-

metal-free $NiCo_2O_4$ nanoflakes directly grown onto a nickel foam (NCONF@Ni) has been found to exhibit high OER activity that is comparable to that of the expensive, noble-metal IrO_2 catalyst. Furthermore, a novel 3-D O- and N-doped carbon nanoweb (ON-CNW) has been developed as an inexpensive, metal-free catalyst for ORR. With a hybrid Li-air cell, the ON-CNW exhibits performance close to that of commercial Pt/C.

In addition, a novel hybrid Li-air cell configuration with decoupled ORR and OER electrodes has been developed. The hybrid Li-air cell with decoupled ORR and OER electrodes eliminates the degradation of ORR catalysts and carbon support in the highly oxidizing charge process and leads to high efficiency with good cycle life.

Table of Contents

List of Tables

List of Figures

Chapter 1: Introduction

1.1 NEED FOR HYBRID LI-AIR BATTERIES

Li-ion batteries have enjoyed great success in the field of portable electronics due to their higher energy densities as compared with other rechargeable battery systems such as nickel-cadmium or lead-acid.[1, 2] They are currently being intensively pursued for electric vehicles and storage of electricity produced from renewable sources such as solar and wind energies. However, the charge-storage capacity and energy density of current Li-ion batteries are limited by the cell voltage and the charge-storage capacities of insertion-compound cathodes and anodes. For example, currently available liquid electrolytes tend to decompose beyond ~ 4.3 V and the capacity of insertion-oxide cathodes reach a limit of ~ 250 mA h g^{-1}. New battery chemistries beyond Li-ion technology are needed to develop the next generation of electrochemical energy storage systems.

Lithium metal is the most promising anode material for high energy density batteries because it has the highest specific capacity (3,860 mA h g^{-1}) and the lowest reduction potential (-3.04 V vs. NHE). Table 1.1 lists the cell voltage, theoretical capacity, and energy density of a few battery systems based on the total mass of the anode and cathode. Li-S (Li_2S as the discharge product) and aprotic Li-O_2 (Li_2O_2 as the discharge product) batteries possess comparable capacities due to the similar molecular weights of S and O_2 and a two-electron redox reaction in both systems. However, the voltage of the Li-O_2 couple (3.0 V) is higher than that of the Li-S couple (2.2 V), which results in a higher energy density. The hybrid Li-air batteries utilize lithium-metal anode in aprotic electrolyte and air-electrode cathode in aqueous catholyte. Although water is introduced during the reduction of O_2, the theoretical specific capacity (1,119 mA h g^{-1}) of the hybrid Li-O_2-H_2O couple is not significantly lower than that of the aprotic Li-air battery. This high capacity occurs because in the Li-O_2-H_2O couple, 4 electrons are transferred per oxygen molecule. In addition, the cell voltage of the hybrid Li-O_2-H_2O

cell is even higher (3.2 V), leading to a higher energy density of 3,581 Wh kg^{-1}. For a hybrid Li-O_2-HCl cell with the acidic catholyte (HCl), the theoretical energy density is reduced to 2,190 Wh kg^{-1} due to the heavier molecular weight of HCl as compared to H_2O. Overall, as seen in Table 1.1, the theoretical energy density of hybrid Li-air batteries is on the same order of magnitude as aprotic Li-air batteries. However, a higher practical energy density is anticipated with hybrid Li-air batteries because the hybrid Li-air batteries can be operated in an ambient environment, eliminating excess battery components needed to keep the batteries operating in a pure oxygen environment.[3] The special battery chemistry of hybrid Li-air batteries also enables the development of a flow-through mode of the catholyte, which further increases the practical energy density of the hybrid Li-air batteries.

Table 1.1. Theoretical data for several battery systems based on their battery chemistry.

Battery Chemistry	Voltage (V)	Capacity (mAh g^{-1})	Energy density (Wh kg^{-1})
Li-ion $3C + LiCoO_2 \leftrightarrow 0.5C_6Li + Li_{0.5}CoO_2$	3.8	100	380
Li-S $2Li + S \leftrightarrow Li_2S$	2.2	1168	2570
Aprotic Li-O_2 $2Li + O_2 \leftrightarrow Li_2O_2$	3.0	1168	3503
Hybrid Li-O_2-H_2O $4Li + O_2 + 2H_2O \leftrightarrow 4LiOH$	3.2	1119	3581
Hybrid Li-O_2-HCl $4Li + O_2 + 4HCl \leftrightarrow 4LiCl + 2H_2O$	4.2	521.4	2190

1.2 BATTERY CHEMISTRY

It is generally understood that the battery chemistry of the hybrid Li-air batteries consists of the reversible four-electron reduction/evolution of oxygen at the cathode and the Li/Li^+ redox couple at the anode. Depending upon the pH of the aqueous electrolyte, the overall cell reactions are as follows:

$$4\ Li + O_2 + 4\ H^+ \leftrightarrow 4\ Li^+ + 2\ H_2O \quad pH < 7$$

$$4\ Li + O_2 + 2\ H_2O \leftrightarrow 4\ LiOH \quad pH \geq 7$$

There are very few reports on studies of the discharge/charge mechanisms of hybrid Li-air batteries. This is probably due to the fact that the ORR and OER in aqueous solutions have been studied for a long time. In addition, the discharge products of hybrid Li-air batteries are mostly soluble in the catholyte mixed with the supporting salt, making them difficult to collect and analyze. In some cases, only visual examination was utilized to determine that discharge products are deposited on the solid electrolyte or the air electrode.[4]

Stevens *et al.*[4] passed a current through a symmetric cell with 5 M LiOH solution on each side of the solid electrolyte. It works like a "lithium pump" that increases the concentration of LiOH on one side; LiOH solid precipitates on one side of the solid electrolyte after the saturation point is reached. As can be seen from Figure 1.1a, the cell voltage increases sharply at the end of discharge as the deposited LiOH blocks Li^+-ion transport. After taking the solid electrolyte out, a dense layer of white powder was found on the solid electrolyte as shown in Figure 1.1b. The white powder was believed to be LiOH and the ceramic surface provided the nucleation points for the crystallization of LiOH.

A recent study reported that Li_2O_2 may also be produced during the discharge process in hybrid Li-air batteries.[5] The authors utilized a Li^+-ion saturated solution as the catholyte and Ketjen black as the catalyst. After a long-term discharge in a pure oxygen atmosphere, the air electrode was subjected to *ex-situ* X-ray diffraction (XRD) analysis. They found that the main reaction product of the discharge process was Li_2O_2. This might

have been due to the low catalytic activity of the Ketjen black catalyst, which could lead to a two-electron ORR process that produced Li_2O_2. In addition, the high concentration of Li^+ ions in the electrolyte could have suppressed the hydrolysis of Li_2O_2, and a high content of PTFE in the air electrode could have created a water-insufficient environment in the air electrode.

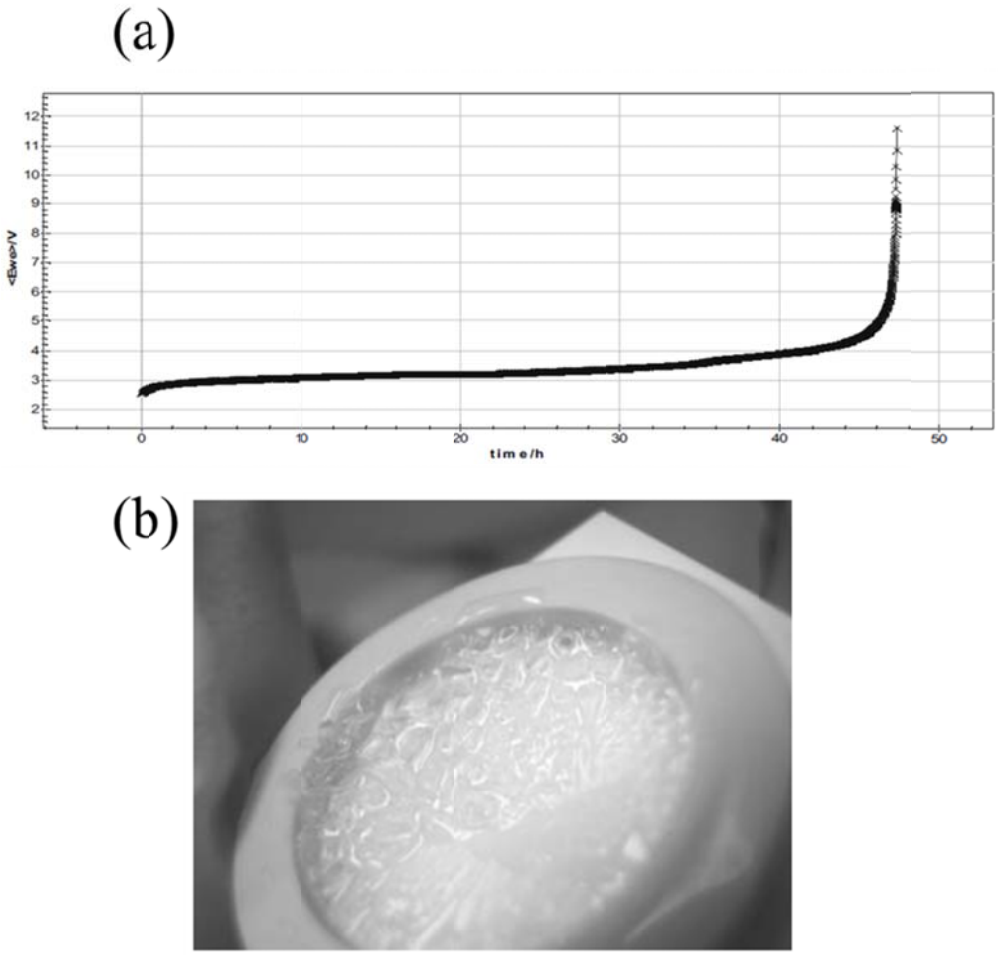

Figure 1.1. (a) Galvanostatic operation of lithium ion pump with a solid electrolyte. (b) Photograph of LiOH crystals on the solid electrolyte. Reprinted from ref. 4.

1.3 CHALLENGES OF HYBRID LI-AIR BATTERIES

Since the pioneering work of Visco *et al*.,[6] tremendous efforts have been made on solving the persistent problems associated with hybrid Li-air batteries. The challenges facing the rechargeable hybrid Li-air batteries are summarized in Figure 1.2.

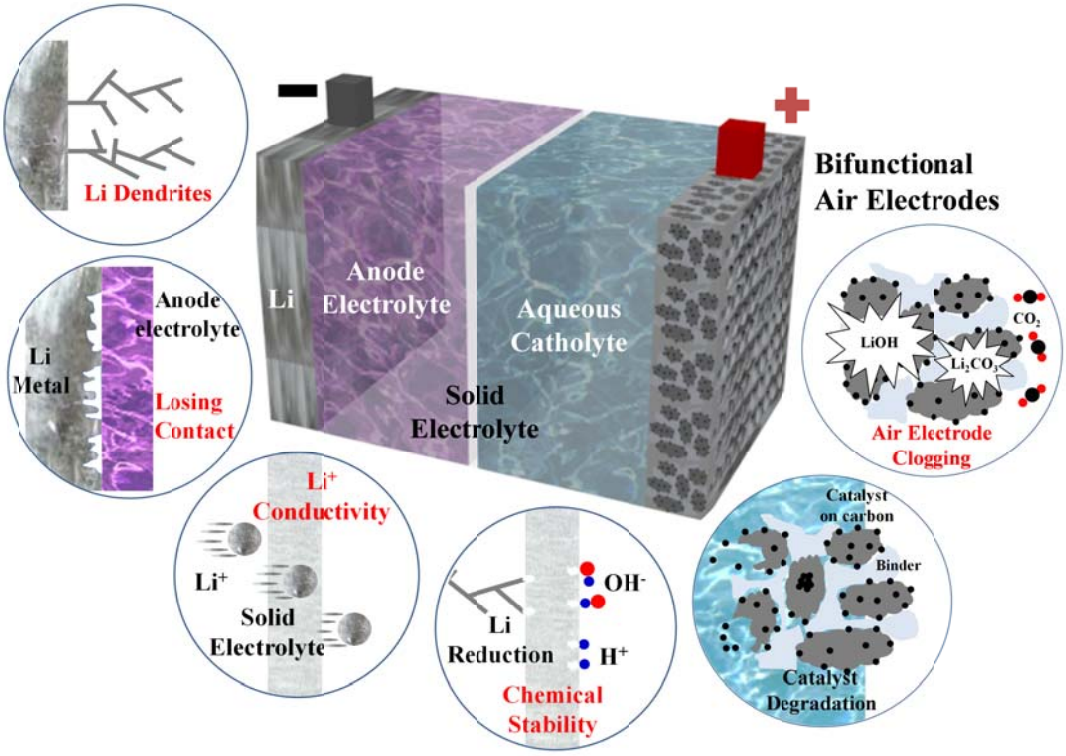

Figure 1.2. Challenges facing the hybrid Li-air battery.

1.3.1 Lithium metal anode

The lithium-metal anode is a persistent problem for rechargeable batteries utilizing lithium metal. For hybrid Li-air batteries with a liquid organic electrolyte on the anode side, lithium dendrites will easily develop upon cycling. Although there will not be an internal short-circuit problem since the solid electrolyte can block the dendrites, the solid electrolyte can be reduced and damaged by contacting lithium metal due to the facile reduction of ions like Ti^{4+} or Ge^{4+} in the solid electrolyte.[7] For hybrid Li-air batteries with Li^+-ion conducting polymer buffer layer at the anode side, dendrites can

easily form without proper additives to suppress them.[8] For hybrid Li-air batteries with a Li^+-ion conducting ceramic buffer layer, dendrite growth has not been reported, which may be due to the rigid solid-solid interface between the lithium metal and the buffer layer. However, the interfacial contact area is prone to decrease due to the repeating inhomogeneous delithiation and lithiation of the lithium metal surface.[4] Furthermore, the cycling efficiency of the lithium-metal anode is affected by the formation of a solid-electrolyte interface (SEI) on the lithium-metal surface.[9, 10]

1.3.2 The solid electrolyte

The solid electrolyte is the key component that enables the hybrid Li-air batteries. Several types of possible solid electrolytes are summarized here including their crystalline states, compositions, Li^+-ion conductivity, and stability in contact with lithium metal and aqueous electrolytes. Currently, the most successful solid electrolyte in Li-air battery research is the commercial NASICON-type glass-ceramic $Li_{1+x+y}Al_xTi_{2-x}Si_yP_{3-y}O_{12}$ (or LTAP, Ohara Inc., Japan). The popularity of the LTAP solid electrolyte is due to its high Li^+-ion conductivity and mechanical strength, as well as its chemical stability in water, mild acids, and mild bases. We will see in this dissertation that the glass-ceramics LTAP is not the ultimate solid electrolyte possessing the highest Li^+-ion conductivity and chemical stability of all usable solid electrolytes. The instability of LTAP in contact with lithium metal necessitates the addition of a buffer layer between the lithium metal and solid electrolyte. This buffer layer causes many technical issues that affect the performance and stability of hybrid Li-air batteries.

1.3.3 The bifunctional air electrodes

A shared problem of all metal-air batteries lies in the efficiency and stability of the bifunctional air electrode. The air cathode utilizes air as the active material. The reversibility of hybrid Li-air batteries requires high activity and durability of the bifunctional air electrodes for both the oxygen reduction reaction (ORR) during discharge and the oxygen evolution reaction (OER) during charge. There are several reviews

summarizing the status of bifunctional ORR/OER catalysts for regenerative fuel cells and traditional metal-air batteries.[11-14] This chapter will summarize only the current status of the bifunctional air-electrode research for hybrid Li-air batteries.

1.4 LITHIUM ANODE

In order to utilize the ultra-high theoretical capacity of the lithium-metal anode in hybrid Li-air batteries, several technical issues need to be addressed. First, during the charge of Li-air batteries, the electrodeposited Li has a dendritic morphology. The lithium dendrites grow from the lithium metal and approach the solid electrolyte. Once these dendrites make contact, the solid electrolyte (which contains Ti^{4+} or Ge^{4+}) will be reduced and its conductivity will drastically drop. Secondly, the lithium-metal anode suffers from a low-cycling efficiency. During charge and discharge, lithium deposition and dissolution, respectively, occur through the SEI, which is a product of the reaction of lithium metal and the electrolyte. As the lithium anode changes shape and volume during cycling, the SEI breaks down and a new SEI forms on any freshly exposed lithium surface. By this process, both the lithium metal and the electrolyte are consumed, leading to the need for excess lithium and electrolyte in the battery. Third, in Li-air batteries that use a solid ceramic buffer layer between the lithium anode and the solid electrolyte, the loss of contact between the lithium metal and ceramic buffer layer deactivates parts of the cell.

1.4.1 Dendrite growth

Dendrite growth can cause many problems in hybrid Li-air batteries because the most widely used solid electrolyte, LTAP, is unstable in direct contact with lithium metal. Although a buffer layer (*e.g.* a liquid organic electrolyte soaked in a polymeric separator or a polymer) can be placed between the lithium metal anode and the solid electrolyte, dendrites will grow and penetrate this buffer layer, especially after many cycles. Studies have shown that the dendrites could be effectively suppressed by additives in the polymer electrolyte. Imanishi *et al.*[8] studied the electrical conductivity and Li^+-ion transport

properties of polyethylene oxide (PEO) (with the lithium salt $Li(CF_3SO_2)_2N$,LiTFSI) as a function of the amount of N-methyl-N-propylpiperidinium-bis(fluorosulfonyl)imide (PP13FSI), an ionic liquid addictive. They found that the conductivity of PEO_{18}LiTFSI-*x*PP13FSI increased with *x* and the lowest interface resistance was achieved with $1.2 \leq x \leq 1.44$. The lithium dendrite growth was suppressed by the addition of PP13FSI into PEO_{18}LiTFSI as confirmed by an *in situ* optical visualization cell, as shown in Figure 1.3. The addition of SiO_2 nanoparticles as a buffer layer filler in the PEO_{18}LiTFSI-PP13FSI polymer electrolyte has been shown to further suppress Li dendrite formation.[15] Furthermore, the ionic conductivity increased and the interfacial resistance decreased as a result of the incorporation of SiO_2 nanoparticles. The nanoparticle fillers improved interfacial compatibility due to (1) reduced reactivity of Li with the electrolyte, (2) increased stiffness and compressibility of the buffer layer, which inhibit dendrite growth, and (3) an even current distribution upon charge and discharge.[10]

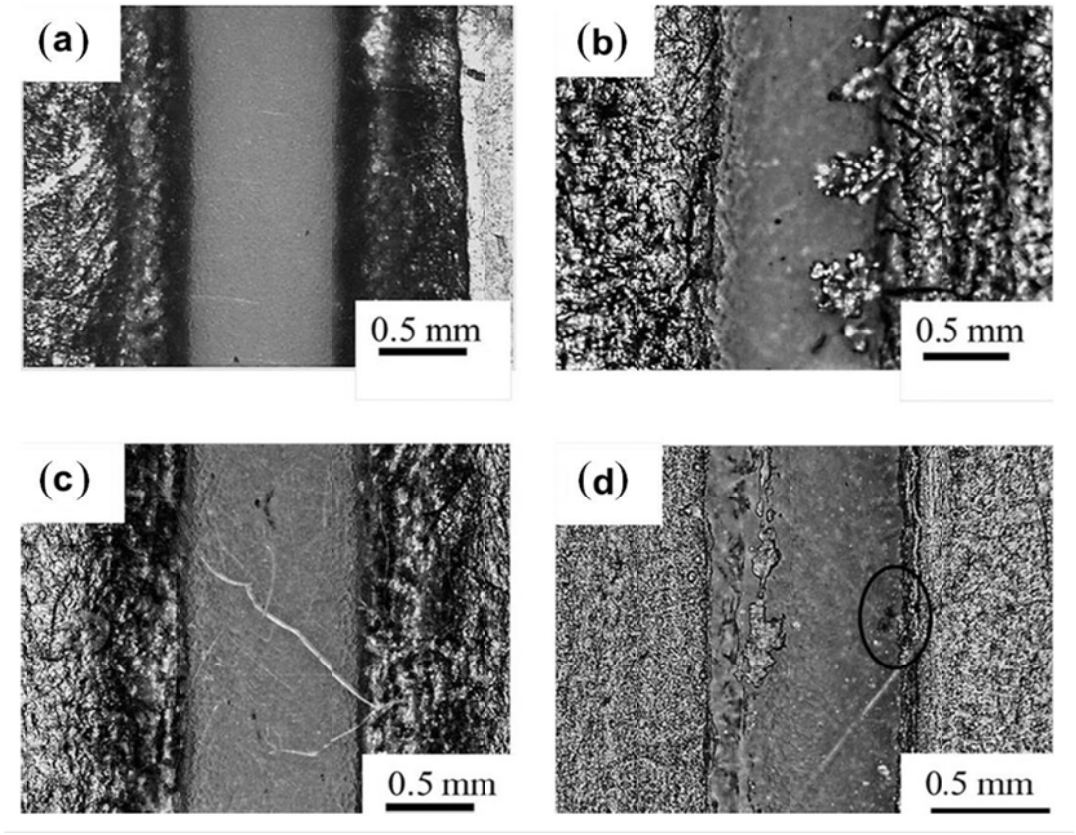

Figure 1.3. Dendrite growth in Li/PEO_{18}LiTFSI/Li and Li/PEO_{18}LiTFSI-1.44PP13FSI/Li cells at 0.1 mA cm^{-2} and at 60 ºC: (a) Li/PEO_{18}LiTFSI/Li for t = 0 h, (b) Li/PEO_{18}LiTFSI/Li for t = 210 h, (c) Li/PEO_{18}LiTFSI-1.44PP13FSI/Li for t = 0 h, and (d) Li/PEO_{18}LiTFSI-1.44PP13FSI/Li for t = 256 h. Reprinted from ref. 8.

In hybrid Li-air batteries, dendrite formation occurs in liquid carbonate electrolyte (*e.g.* 1 M $LiPF_6$ in ethylene carbonate (EC) / diethylcarbonate (DEC) (1:1 v/v)).[16, 17] Although layers of separator can be placed between the lithium-metal anode and the solid electrolyte to block the dendrites, after continuous cycling, dendrites will finally penetrate the separator and touch the solid electrolyte. Dendrite formation can be greatly suppressed by choosing appropriate solvents, supporting salts, and electrolyte additives. Liquid carbonate electrolytes have been successfully utilized in commercial Li-ion

batteries due to their good compatibility with Li-intercalation oxide cathodes and graphitic carbon anode. However, they are not helpful in suppressing dendritic Li growth on the lithium-metal anode.[18] Ether solvents, such as tetrahydrofuran (THF), 2-methyltertrahydrofuran (2-Me-THF), and diethyl ether (DEE) were reported to have fewer dendrite formation problems.[19] However, in these cases, prolonged cycling still led to dendritic Li deposition.[20, 21] Other possible solvents include a series of fluorinated esters, boric acid esters of glycol (BEG), and tetramethylene sulfone, all of which were reported to improve the performance of Li metal anodes.[22-24] Li salts are not as diverse as the solvents. Among the major salts used for lithium batteries, $LiClO_4$, $LiOSO_2CF_3$, and LiTFSI do not suppress the formation of Li dendrites.[18, 25] $LiPF_6$ has been shown to promote the interfacial stability of Li-metal anode possibly through HF, which is produced by the chemical reaction between PF_6^- and trace amounts of water in the electrolyte.[26, 27] Other possible candidates are lithium bis(perfluoroethylsulfonylimide) ($LiN(C_2F_5SO_2)_2$, LiBETI) and ionic liquids.[25, 28]

Adding a small amount of additives into the electrolyte is another effective way to control the Li-metal surface through the following four mechanisms: (1) reaction with the Li surface to produce stable SEI layers, (2) controlling the current distribution or reducing Li reactivity with the electrolyte, (3) forming Li alloys which affect the electrodeposited Li morphology, and (4) an electrostatic shielding mechanism by introducing Cs^+ or Rb^+ cations.[10] Kanamura *et al.*[27] added a small amount of HF to various nonaqueous electrolytes. Lithium dendrites formed in all of the electrolytes without HF additive. On the other hand, the electrodeposited lithium in all electrolytes containing HF was dendrite-free. The authors concluded that HF will react with the native Li surface layers, producing a very thin film of a LiF-Li_2O bilayer, which promotes smooth lithium deposition. Naoi *et al.*[29] tried to stabilize the lithium surface films by adding two kinds of nonionic polyether-type surfactants: polyethyleneglycol dimethyl ether and a copolymer of dimethylsilicone and propylene oxide. They found that the lithium surface films were very stable and the localized deposition was

suppressed in the presence of these surfactants. Other similar surfactants are compounds of decalin and benzene compounds.[30, 31]

A different approach is to introduce a small amount of metal ions, (*e.g.* Na, Mg, Al, and Sn) into the lithium electrolyte.[32-34] This results in a co-deposition of the addictive ions and lithium ions that suppresses the dendrite growth. It was suggested that the Li surface becomes more regular as a result of a thin layer of a Li-alloy.

An electrostatic shielding mechanism was proposed by Zhang *et al.*[35] A small amount of Cs^+ or Rb^+ cations was added into the electrolyte. During lithium electrodeposition, these cations form a positively charged electrostatic shield around any growth tip of the protuberances, forcing further depostition of lithium ions to nearby regions and thus eliminating dendrites formation.

1.4.2 Interface between the lithium metal and buffer layer

In hybrid Li-air batteries with the lithium-metal anode separated from the solid electrolyte by another Li^+-ion conducting solid (*e.g.* polymer, ceramic, *etc.*), which acts as a buffer layer, and the interface between the lithium metal and the buffer layer may be degraded upon repeated cycling. Philipe *et al.*[4] utilized lithium phosphorous nitride (LiPON) with a thickness of 0.5 – 2 μm as the buffer layer, which was deposited by radio frequency cathodic pulversation. Up to 40 cycles were obtained with cells cycled at a current density of 2 mAh cm^{-2}. The main reason for the degradation of cell performance was identified as the loss of contact between lithium metal and the LiPON buffer layer. Although a dense layer of lithium was formed during the initial charge, the dense layer becomes more porous or columnar upon Li dissolution and deposition. This volume change produces mechanical constraints on the lithium layer and leads to loss of contact between lithium and the ceramic. In addition, the possibility of solid-electrolyte degradation via lithium crossing through the thin layer of LiPON remained if the surface of the solid electrolyte was not sufficiently clean or dust-free.

Imanishi *et al.*[36] applied PEO_{18}LiTFSI -1.44PP13TFSI as the buffer layer in hybrid Li-air batteries. Although the interfacial resistance was greatly reduced by doping of the ionic liquid in the polymer electrolyte, the cell performance was significantly affected by SEI formation, leading to increased electrode resistance within the initial 25 cycles. A similar anode configuration was also applied in a hybrid electrochemical capacitor developed by the same group.[37] 27 % of the capacity was lost after 2000 cycles due to the degradation of the multi-layered Li negative electrode.

1.5 SOLID ELECTROLYTE

The solid electrolyte is the key component that enables the concept of hybrid Li-air batteries. The foremost requirement for the solid electrolyte is a thin and mechanically robust membrane with a high Li^+-ion conductivity at the operating temperature. Furthermore, they should be chemically stable in contact with aqueous electrolytes of various pH values, organic electrolytes, and lithium metal. Finally, as in all industrial developments, solid-state Li^+-ion conductors must be environmentally benign, non-toxic, and low-cost materials and easy to prepare.[38] We mainly discuss five types of solid Li-ion conductors here due to their possible stability in water: perovskite-type, NASICON-type, LiSICON-type, and garnet-type Li^+-ion conducting oxides, and single-crystal silicon wafers.

1.5.1 Fast Li^+-ion conduction

Currently the most successful solid electrolyte in hybrid Li-air batteries is the NASICON-type glass-ceramics ($Li_{1+x+y}Al_xTi_{2-x}Si_yP_{3-y}O_{12}$ or LTAP) produced by Ohara Inc., Japan. The specialty of this solid electrolyte lies in the high Li^+-ion conductivity, good mechanical strength, and very good chemical and thermal stabilities, as shown in Figure 1.4.[39] Two kinds of solid electrolytes are commercially available: Li_2O-Al_2O_3-SiO_2-P_2O_5-TiO_2-GeO_2 with a conductivity of 1 x 10^{-4} S cm^{-1} and Li_2O-Al_2O_3-SiO_2-P_2O_5-TiO_2 with a higher conductivity of 2.5 to 4 x 10^{-4} S cm^{-1} at 25 °C. The former has better mechanical strength than the later. The crystal structure of NASICON $A_xB_2(PO_4)_3$ is a

framework built of corner-shared PO_4 tetrahedra and BO_6 octahedra, providing a relatively open, three-dimensional network of sites and conduction pathways for various A cations. The Li^+-ion conductivity could be greatly enhanced by doping trivalent cations (Al, Cr, Ga, Fe, Sc, In, Lu, Y, or La) in the octahedral sites. For example, Aono *et al.*[40] reported that the conductivity in $Li_{1+x}M_xTi_{2-x}(PO_4)_3$ (M = Al, Sc, Y, and La) increased with increasing content of the M^{3+} dopant, and the maximum conductivity was obtained with $x = 0.3$ for all the systems. Some of the main reasons for the improvements were thought to be the increase in the concentration of Li^+ and the density of the pellet. The highest conductivity was obtained with the nominal composition $Li_{1.3}Al_{0.3}Ti_{1.7}(PO_4)_3$ (bulk conductivity = 3×10^{-3} S cm^{-1} at 298 K). Compared with sintered materials, glass-ceramics are advantageous due to the ease of manufacturing and dense microstructure.[41] Heat-treatment of glasses with the formula Li_2O-M_2O_3-TiO_2-P_2O_5 (M = Al and Ga) results in fast Li^+-ion conduction in the glass-ceramics. The glass-ceramics contain a main crystalline phase of $LiTi_2(PO_4)_3$ with Ti^{4+} partially replaced by Al^{3+} or Ga^{3+}. The maximum conductivity obtained was 1.3×10^{-3} S cm^{-1} and 9×10^{-4} S cm^{-1}, respectively, for Al^{3+} or Ga^{3+} doping at room temperature. Another system of the NASICON family is $LiZr_2(PO_4)_3$, which should be electrochemically stable in contact with lithium metal. The NASICON $LiZr_2(PO_4)_3$ compound prepared at 1473 K exhibits a first order transition from the triclinic $C\bar{1}$ form to the rhombohedral $R\bar{3}c$ form at about 310 K, and the rhombohedral phase $R\bar{3}c$ with high Li^+-ion conductivity can be stable only above 50 ºC.[42] The substitution of Ca^{2+} or Y^{3+} for Zr^{4+} in $LiZr_2(PO_4)_3$ can transform the structure to rhombohedral NASICON at room temperature and increase the bulk Li^+-ion conductivity above 1×10^{-4} s cm^{-1}.[43, 44]

Other promising Li^+-ion solid electrolytes with high Li^+-ion conductivity are the Li-rich garnet-type metal oxides. Weppener's group[45] reported facile Li^+-ion conduction in $Li_5La_3M_2O_{12}$ (M = Nb, Ta), which led to world-wide interest in garnet-type Li^+-ion conductors. $Li_7La_3Zr_2O_{12}$ was reported to exhibit a high Li^+-ion conductivity of $> 10^{-4}$ S

cm^{-1} at 25 ºC and stability in contact with lithium metal.[46] The bulk and grain boundary resistances are on the same order of magnitude, which is beneficial for ceramic solid electrolytes with a polycrystalline structure.[47] Adding Al_2O_3 has been found to help with the sintering of $Li_7La_3Zr_2O_{12}$ without blockage of the Li^+-ion framework.[48] A high Li^+-ion conductivity of 8×10^{-4} S cm^{-1} was obtained by Shingo Ohta *et al.*[49] with the formula of $Li_{6.75}La_3Zr_{1.75}Nb_{0.25}O_{12}$. Recently, an even higher Li^+-ion conductivity of $\sim 1 \times 10^{-3}$ S cm^{-1} has been obtained with $Li_{7-x}La_3Zr_{2-x}Ta_xO_{12}$ ($x = 0.6$, activation energy $E_a = 0.35$ eV) by Goodenough's group.[50]

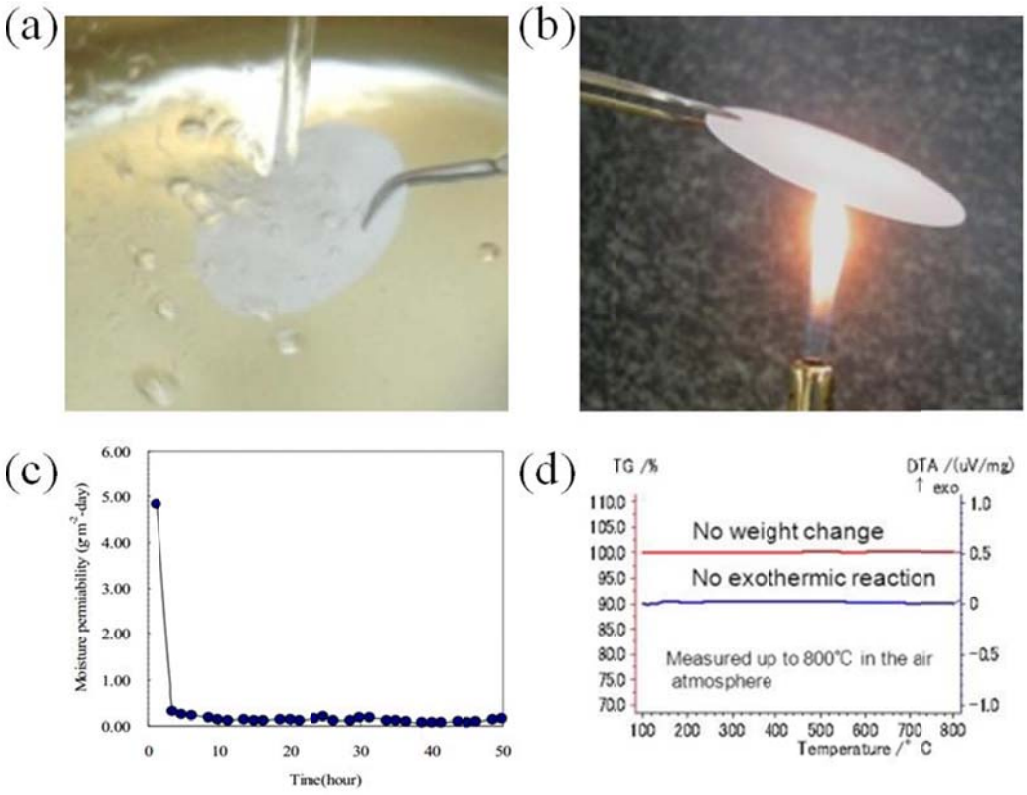

Figure 1.4. The LTAP membrane is stable in (a) water and (b) against flame. (c) Moisture permeability measurement confirmed that the LTAP can block moisture penetration. (d) Thermogravimetric analysis (TGA) demonstrates that the thermal stability is up to 600 ºC. Reprinted from ref. 39.

The perovskite-type (ABO_3) lithium lanthanum titanate (LLTO) is also an excellent Li^+-ion conductor, with the formula of $Li_{3x}La_{(2/3)-x}\square_{(1/3)-2x}TiO_3$ ($0<x<0.16$). A high bulk conductivity of 1×10^{-3} S cm^{-1} (E_a = 0.4 eV) at 27 ºC, which was comparable to that of a polymer or liquid electrolyte, was obtained when $x \approx 0.1$.[51] The high Li^+-ion conductivity of LLTO is related to the large concentration of *A* site vacancies, which allow for the movement of Li^+ ions between the *A* sites. By substituting La with 5 mol% Sr, a slightly higher bulk conductivity of 1.5×10^{-3} S cm^{-1} was achieved. Despite the high bulk ionic conductivity, the problem of the LLTO solid electrolyte lies in its high grain-boundary resistance, which hinders its application as a polycrystalline solid-electrolyte membrane.[52]

LISICON stands for Lithium Super Ionic Conductor, a name that was first given to $Li_{14}ZnGe_4O_{16}$. $Li_{14}ZnGe_4O_{16}$ belongs to the solid solution $Li_{2+2x}Zn_{1-x}GeO_4$, which contains interstitial Li^+ ions with the range of $-0.36 \leq x \leq +0.87$. Although $Li_{14}ZnGe_4O_{16}$ has a very high Li^+-ion conductivity of 0.125 S cm^{-1} at 300 ºC, the conductivity at room temperature is fairly low (1×10^{-6} S cm^{-1}).[53]

The single-crystal Si wafer solid electrolyte was first utilized in an aprotic Li-air battery to prevent O_2 from diffusing into the lithium anode.[54] The Li^+-ion conductivity of Si wafers with different thicknesses was tested in a specially designed set-up. It was found that the wafers possess a maximum Li^+-ion conductivity of 6×10^{-7} S cm^{-1} when the thickness is approximately 5 μm. The diffusion coefficient of O_2 in silicon is 34 orders of magnitude smaller than that of lithium. In this way, the lithium-metal anode was protected from the gradual corrosion by O_2, improving the cycle life in the long term.

1.5.2 Chemical stability

The stability of the solid electrolyte has a profound influence on the overall cell performance. Most studies on solid electrolytes focus on the high Li^+-ion conductivity, but chemical stability in the battery environment is of equal importance to ensure a long lifetime of the battery. The hybrid Li-air batteries possess stricter requirements on the

solid electrolyte than other types of lithium batteries. Ideally, the solid electrolyte should be stable in aqueous solutions of various pH values. This is difficult because most oxides tend to dissolve in strongly acidic or alkaline solutions.

NASICON-type LTAP materials are unstable with Li metal due to the facile reduction of Ti^{4+}. In one particular case, the reaction between lithium metal and LTAP was observed, which led to the development of cracks in the solid electrolyte.[4] Crack formation on the solid electrolyte was enhanced when pressure was applied on the cell to keep a tight contact between the cell components. Dendrites are formed in both organic liquid electrolyte and polymer electrolyte.[8, 55] In our experiments, we observed a change in the color of the LTAP when lithium dendrites touched the solid electrolyte after long-term cycling, similar to the reduction of Ti^{4+} observed in $Li_{0.33}La_{0.57}TiO_3$.[56] The LTAP is not stable in strong acids or bases,[57] necessitating the use of a catholyte with a mild pH value as discussed in the catholyte section later.

The perovskite (ABO_3)-type lithium lanthanum titanate (LLTO) is unstable with Li metal due to the facile reduction of Ti^{4+}. Wolfenstine *et al.*[58] studied the stability of LTAP and LLTO in aqueous solutions and found that both electrolytes were relatively stable in a water environment (pH ~ 7) and not stable at low and high pH values. The LISICON-type $Li_{14}ZnGe_4O_{16}$ is highly reactive with lithium metal.[38] In addition, it is not stable with atmospheric CO_2 and its conductivity decreases with time. Gopalakrishnan *et al.*[59] studied the Li^+/H^+ exchange in LISICON-type Li_2ZnGeO_4 and $Li_{2+2x}Zn_{1-x}GeO_4$ (x = 0.50 and x = 0.75). They found that the parent material Li_2ZnGeO_4 does not exhibit a ready Li^+/H^+ exchange because all of the Li ions form part of the tetrahedral framework structure. However, when the Li^+ ions are in both the framework (tetrahedral) and nonframework sites, LISICONs undergo a facile Li^+/H^+ exchange in a weak acetic acid solution. This facile exchange behavior indicates that this kind of solid electrolyte is not suitable for hybrid Li-air batteries due to the replacement of Li^+ ions in the solid electrolyte by H^+ from the aqueous electrolyte. Regardless of the pH value, protons are always present in aqueous solutions.

Garnet-type Li^+-ion conductors are stable in contact with lithium metal, eliminating the need for a buffer layer between lithium metal and solid electrolyte which is beneficial for reducing the overall internal resistance of Li-air batteries.[45] But Li-rich garnet oxides are unstable in water and Li^+-ions in garnet are exchanged by protons from water quickly. The extent of Li^+/H^+ exchange depends on the population of Li in octahedral interstitial sites of the garnet framework $B_3C_2O_{12}$. A $Li_xB_3C_2O_{12}$ garnet with $x \leqslant 3$ contains Li only in the tetrahedral sites 24*d* and is stable in water.[60] Takeda *et al.*[61] studied the stability of garnet-type $Li_6La_3Zr_2O_{11.5}$ in deionized water and a series of aqueous solutions: saturated LiCl, deionized water, 0.1 M HCl, and1 M LiOH. They concluded that $Li_6La_3Zr_2O_{11.5}$ was stable in saturated LiCl with respect to the structure and electrical conductivity, but unstable in water and acidic and alkaline solutions.

The single-crystal silicon wafer was reported to be stable in many electrolytes, including neutral and acidic aqueous electrolytes.[62] However, the wafer is not stable in contact with lithium metal due to severe electrochemical reactions. In addition, the silicon lattice will expand and induce a possible failure of the crystalline structure when too much lithium is accumulated in the lattice.[54] Finally, a highly resistive SEI layer was found on the side of the silicon wafer facing the air electrode due to the decomposition of the aprotic electrolyte. Much work is still needed to improve the Li^+-ion conductivity and electrochemical stability of the Si wafer in order for it to be competitive with the LTAP membrane, although the current cost of the Si wafer is ten times lower than that of LTAP.

1.6 ACIDIC CATHOLYTE

Acidic catholytes provide higher voltages than alkaline catholytes. Moreover, there is no need to worry about the CO_2 ingression associated with alkaline catholytes. However, there are several challenges associated with acidic catholytes. First, non-noble-metal catalysts suffer from instability and low activity in an acidic environment so it is hard to avoid the use of noble-metal catalysts. Second, the concentration of the acid needs to be increased to increase the overall energy density of the catholyte; otherwise, water

will decrease the overall energy density. Third, cell components (*e.g.,* solid electrolyte and current collector) need to be stable in the acidic environment, which is a challenge for many oxides and metals.

1.6.1 Catholyte selection

Acidic catholytes are composed of three parts: water, acid, and supporting salts. Currently, strong acids are not good options for hybrid Li-air batteries because the most widely used solid electrolyte, LTAP, corrodes easily in strong acids. For example, Imanishi *et al.*[63] immersed LTAP in 0.1 M HCl for 3 weeks. Although no apparent impurity peaks could be found by XRD, the resistance of LTAP increased significantly after immersion. The SEM images further indicated the presence of LTAP surface corrosion.

Weaker acids, *e.g.,* acetic acid (CH_3COOH or HOAc) or phosphoric acid (H_3PO_4), have been used in hybrid Li-air batteries.[64-66] The acetic acid possesses a theoretical capacity of 447 mAh g^{-1} and a dissociation constant (pKa) of 4.7. The dissociation constant is an important index for indicating the suitability of the acid for application in hybrid Li-air batteries. The higher the dissociation constant, the higher the pH value of the catholyte for a certain concentration. However, the pH value of HOAc is still too low for the solid electrolyte. Thus, a conjugate base, lithium acetate (LiOAc), was added to suppress the dissociation of HOAc and increase the pH value of the overall solution. The sandwiched structure of the hybrid Li-air battery with HOAc-H_2O-LiOAc catholyte is shown in Figure 1.5a. The total internal resistance of the cell was 5,446 Ω cm^2 at room temperature, which was mostly due to the interfacial resistance between the lithium-metal anode and the polymer buffer layer. However, the total internal resistance can be greatly decreased to 185 Ω cm^2 by operating the cell at 60 ºC.

The problem with acetic acid is its severe volatility, requiring storage in a closed environment. Even in a pressurized environment, the utilization rate was low.[67] As can be seen from the cycling performance of the battery in Figure 1.5b, the cell achieved a

practical capacity of 250 mAh g^{-1} for 15 cycles, which was much lower than the theoretical capacity of 447 mAh g^{-1}. The limited practical capacity was due to the low utilization rate of acetic acid.[68]

Phosphoric acid possesses a theoretical capacity of 273 mA h g^{-1} (considering only one proton) and a dissociation constant of 2.16, which is much higher than that of strong acids such as HCl (-9.3) and H_2SO_4 (-6.6). However, when used alone, phosphoric acid will corrode the solid electrolyte and we observed an increase in the bulk and grain boundary resistance of the LTAP.[69] The addition of a conjugate base, LiH_2PO_4, to the catholyte led to the formation of a phosphate buffer, which showed good compatibility with hybrid Li-air batteries without any observable increase in the bulk or grain boundary resistance of LTAP.[65] This could be attributed to the suppression of the dissociation of H_3PO_4 by LiH_2PO_4, increasing the pH value of the catholyte. The theoretical capacity of phosphoric acid can be tripled (819 mA h g^{-1}) if all three protons are utilized. This value is even higher than that for HCl (734 mA h g^{-1}). The problem with utilizing all three protons of phosphoric acid is that Li_2HPO_4 and Li_3PO_4 have very low solubility in water. Thus, they will deposit and clog the air electrode upon discharge. As a result, the polarization of the air electrode will increase, leading to a gradual loss of the battery efficiency.

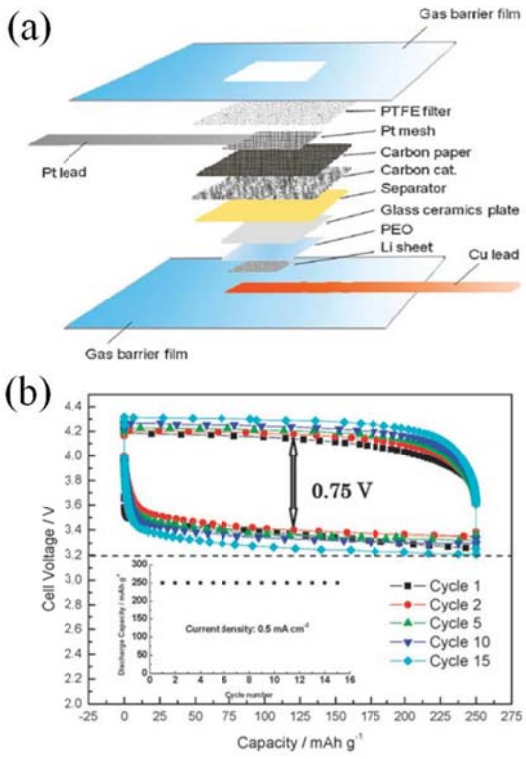

Figure 1.5. (a) Schematic diagram of the hybrid Li-air battery with HOAc-H_2O-LiOAc catholyte. (b) Cycling performance of the battery at 0.5 mA cm^{-2} and 60 ºC. Reprinted from ref. 67.

Another promising strategy for utilizing strong acids in hybrid Li-air batteries is to add imidazole to the catholyte.[70] Imidazole has a fairly high dissociation constant of 7.0,[71] enabling the use of many strong acids as catholytes. As can be seen in Figure 1.6a, imidazole is a small molecule with a strong ability to absorb the protons in water: it acts as a proton reservoir. In the initial state of the battery, most protons in the catholyte are trapped in the imidazole-proton composite, keeping the pH value close to neutral. Upon discharge, as protons are consumed, the imidazole-acid composite will gradually release protons. The pH values of imidazole buffered HCl solutions were calculated and are presented in Figure 1.6b. In order to obtain a pH value of 5, the concentration of

imidazole should be slightly higher than that of the acid (0.01 %). The discharge performance in Figure 1.6c shows that the discharge voltage will be higher with a higher concentration of acid and imidazole. Despite these advantages, the problem with the imidazole buffered catholyte is that the imidazole is not stable at high voltages, which means that imidazole will be oxidized during the charge process instead of water. A mechanically rechargeable catholyte may be possible by condensing the catholyte to extract the discharge product LiCl and add HCl after discharging the battery. However, in order to make the cell electrochemically rechargeable, a more stable base molecule with a stability window beyond that of water is needed.

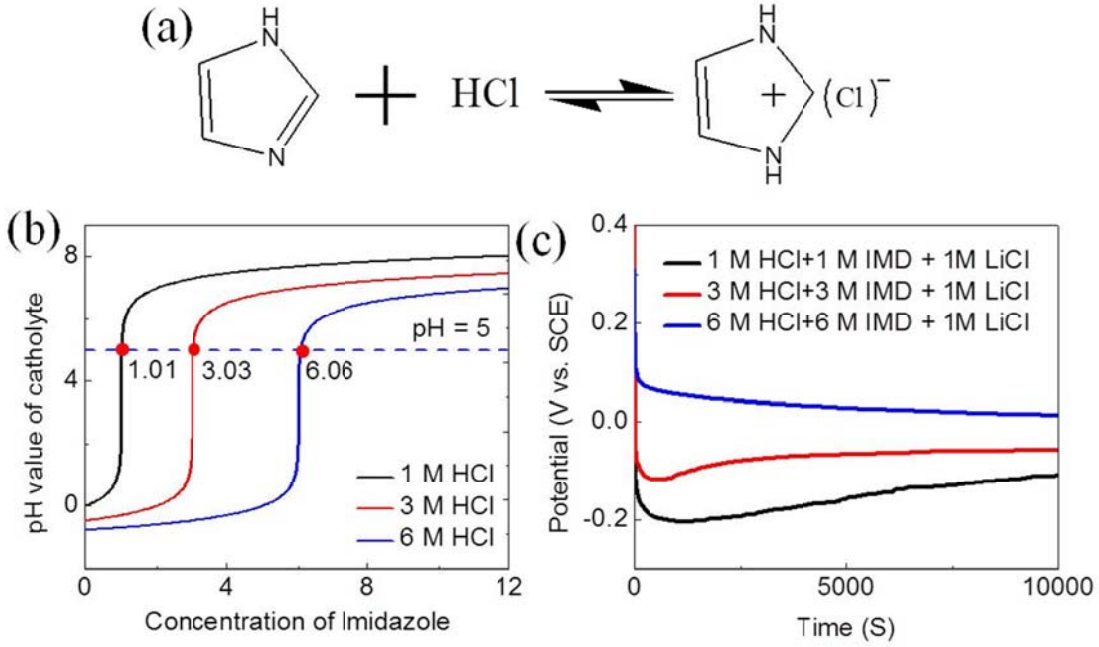

Figure 1.6. (a) Illustration of the composite formed between imidazole and hydrochloric acid. (b) Calculation of the pH value of hydrochloric acid solutions with various amounts of imidazole additive. (c) The half-cell discharge voltage profiles of different imidazole-hydrochloric acid catholytes.

1.6.2 Catalyst selection

The catalysts for the acid catholyte should fulfill two requirements. The first is that they should be stable in the acidic environment. The second is that they should show adequate catalytic activity for ORR/OER in the acidic environment. Due to the instability issue of non-noble-metal catalysts in acidic electrolytes, the most widely used catalyst in hybrid Li-air batteries with acidic catholyte is Pt/C, not only as the ORR catalyst but also as the OER catalyst. We utilized a commercial Pt/C catalyst in hybrid Li-air batteries with a phosphate buffer catholyte.[65] Although Pt/C is very active as an ORR catalyst in acidic electrolytes, it suffers from several problems (*e.g.*, corrosion of the carbon support, dissolution and migration of Pt, and agglomeration of nanoparticles), which are even worse at high charging voltages.[72-78]

Xing *et al.*[79] demonstrated a carbon nanotube buckypaper deposited with Pt nanoparticles as the catalysts in hybrid Li-air batteries. The Pt/CNT buckypaper was synthesized by a simple filtration method together with commercial carbon nanofibers. The schematic diagram of the cell structure is shown in Figure 1.7a. The layered structure includes an air cathode in the sulfuric acid catholyte and a Li foil in an aprotic anode electrolyte. Figure 1.7b demonstrates the cross section of the Pt/CNT buckypaper. The CNTs are intertwined, forming lots of pores for air and electrolyte diffusion. The cycling performance with 1 M H_2SO_4 is shown in Figure 1.7c. The initial round-trip overpotential was 1.25 V, which increased to 1.59 V after cycling. This fast degradation was mainly due to the degradation of the Pt/C catalysts at high voltage. Although Pt/C is a good catalyst for ORR, the high-voltage, oxidizing OER process brings a lot of damage to Pt nanoparticles as well as the carbon support. In addition, the solid electrolyte also underwent corrosion in such an acidic solution. The cell performance with 0.01 M H_2SO_4 is shown in Figure 1.7d. The cell achieved a discharge capacity of 306 mAh g^{-1} for 10 cycles.

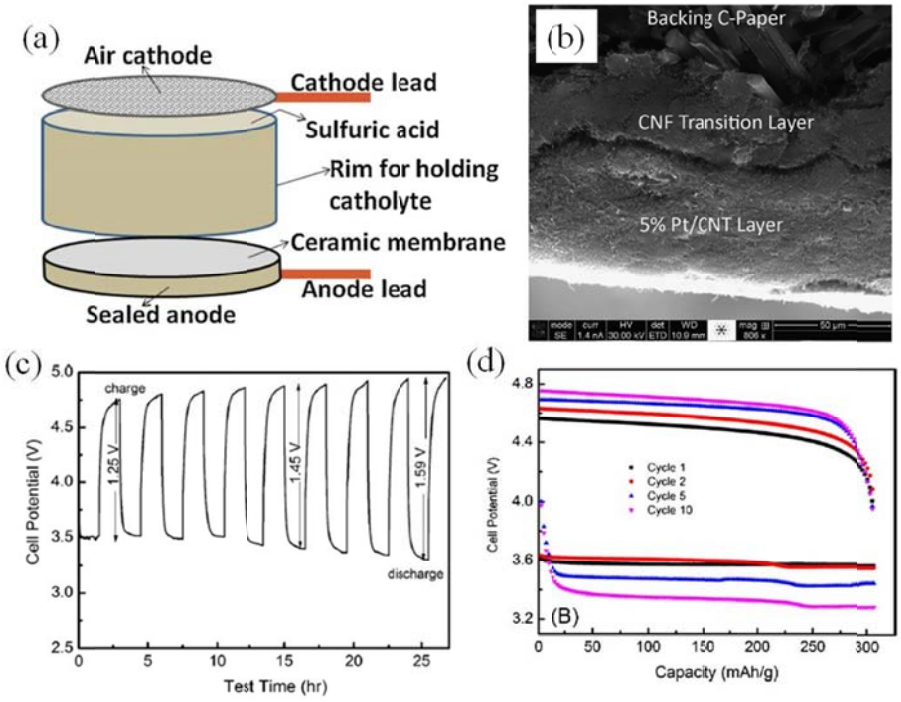

Figure 1.7. (a) Schematic diagram of hybrid Li-air battery with Pt/CNT catalyst. (b) A cross-section of 5 wt.% Pt/CNT buckypaper layer on a CNF transition layer. Charge-discharge performance of the 10 cm^2 Li-air cell with (c) 1.0 M H_2SO_4 and (d) 0.01 M H_2SO_4. Reprinted from ref. 79.

In a different approach, IrO_2 and Pt were both deposited on carbon nanotubes (CNT) to form a bifunctional catalyst, which improved the cell performance by achieving a capacity of 300 mAh g^{-1} for 20 cycles.[80] The round-trip overpotential increased from 72 to 81 % at the 10^{th} cycle. TEM images of the synthesized IrO_2/CNT and Pt/IrO_2/ CNT are shown in Figure 1.8a and b. The cycling performance of cells with Pt/CNT and Pt/IrO_2/CNT is shown in Figure 1.8c and d, respectively. The Pt/IrO_2/ CNT cells possessed higher round trip efficiency and better cycling stability than that with Pt/CNT.

A TiN catalyst, which has been widely utilized as the conductive support for Pt in polymer electrolyte fuel cells, was utilized as the ORR catalyst in hybrid Li-air batteries

with an acetic acid catholyte.[66] The synthesis of TiN has already been commercialized and could significantly reduce the cost of Li–air fuel cells. It was suggested that TiN has considerable catalytic activity for ORR in weak acidic solutions, which is just slightly inferior to the noble metal Pt.

Nitrogen-doped graphene nanosheets (N-GNSs) show a high electrocatalytic activity for the air electrode of Li–air fuel cells based on hybrid electrolytes.[81] N-GNSs exhibited a high discharge voltage, which was near that of commercial 20 wt. % Pt/carbon black. It was suggested that the presence of pyridine-type N along with a large proportion of edge sites in the N-doped GNSs may play a positive role in the catalysis of the ORR under acidic conditions.

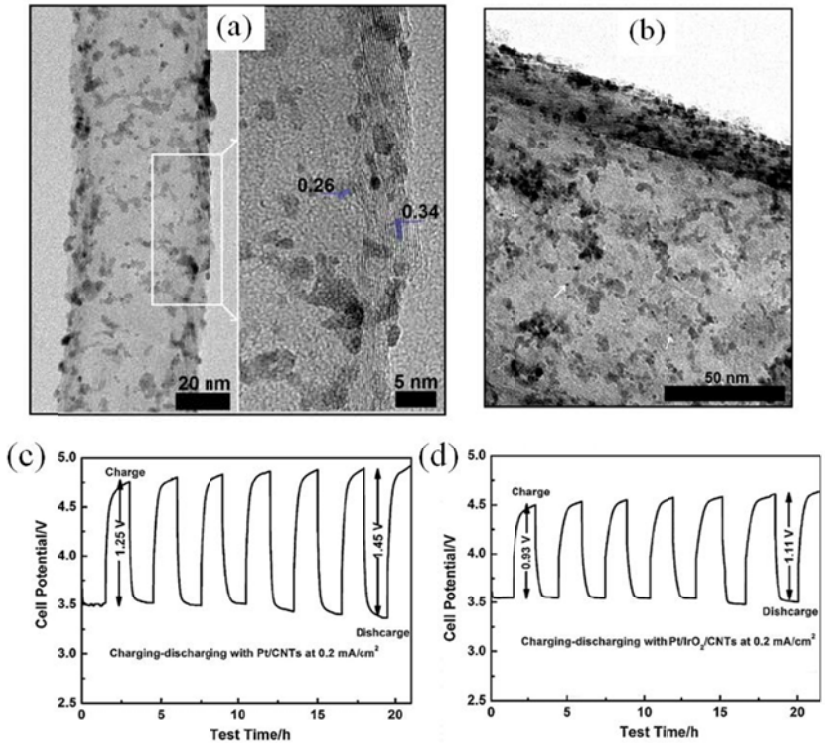

Figure 1.8. TEM images of (a) IrO_2/CNT and (b) Pt/IrO_2/CNT. Charge-discharge performance of the hybrid Li-air cells at 0.2 mA cm^{-2} in 1.0 M H_2SO_4 with (c) Pt/CNTs and (d) Pt/ IrO_2/CNTs. Reprinted from ref. 80.

1.6.3 Cell set-up

For hybrid Li-air batteries with an acidic electrolyte, there is no CO_2 ingression problem and so there is no need to utilize any accessories to filter out CO_2 gas. However, since the solid electrolyte may be susceptible to strong acids, a Li^+-ion conducting polymer may be deposited on the solid electrolyte to avoid direct contact of the solid electrolyte with the acidic catholyte. Since the discharge products may deposit on the air electrode and block the incoming air, a proton-conducting polymer can be coated onto the air electrode to let the discharge products deposit in the catholyte chamber.[4] A flow-through mode of the catholyte is possible with the acidic catholyte. The pressure in the catholyte chamber needs to be carefully controlled to prevent electrolyte from breaking the solid electrolyte or flooding the air electrode, which possess relatively weak mechanical strength.

1.7 ALKALINE CATHOLYTE

For the alkaline catholyte, there will be more options for low-cost non-noble-metal catalysts, *i.e.*, carbon materials, transition-metal oxides, perovskites, *etc*.

1.7.1 Catholyte selection

For the alkaline catholyte, the most utilized supporting salt is LiOH, which not only provides an alkaline environment to boost the ORR reaction on non-noble-metal catalysts, but also provides Li^+ ions to improve the conductivity of the catholyte.[82] However, LiOH by itself is not a good choice as the supporting salt for hybrid Li-air batteries because a high concentration of Li^+ ions is needed to increase the conductivity of the catholyte, but high concentrations of LiOH will introduce high alkalinity to the catholyte. In addition, since LiOH will be consumed during long-term charging of hybrid Li-air batteries, there will be a sharp increase in the internal resistance and a rise in charging voltage upon overcharging.[82] Therefore, additional supporting salt is needed to provide both high ionic conductivity and low pH at the initial state of the battery.

Kim *et al.*[82] studied the effect of the LiOH concentration on the discharge voltage of hybrid Li-air batteries. They concluded that the discharge voltage increased with lower concentrations of LiOH in the aqueous electrolyte due to the higher solubility of oxygen in lower alkaline concentrations, as shown in Figure 1.9a. Hence, by using weak (≤ 0.05 M LiOH) instead of strong alkaline solutions, the Li-air battery displayed discharge and charge voltages of 3.53 V and 4.19 V, respectively, at 0.05 mA cm^{-2}, resulting in an 84 % voltage efficiency. They also studied the effect of additional supporting salt in the catholyte. It was found that the addition of $LiClO_4$ to the aqueous solution further improved the voltage efficiency to 85 % (3.32 V at the discharge and 3.90 V at the charge) by reducing the internal resistance of the cell (Figure 1.9b). The use of $LiClO_4$ also alleviated the pH increase caused by fast or long-term discharge of the cell.

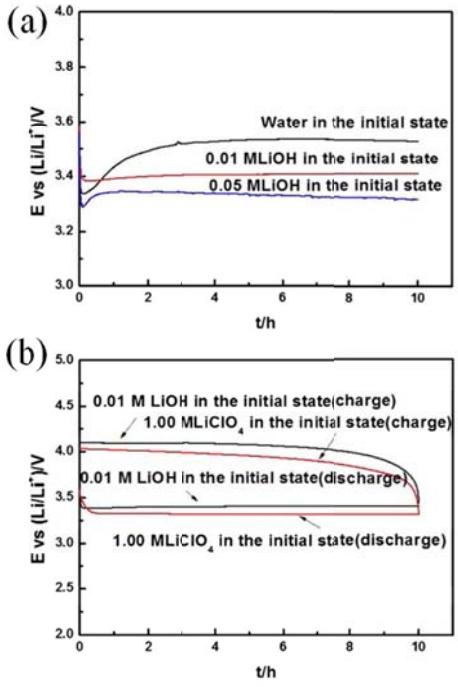

Figure 1.9. (a) Discharge performance of hybrid Li-air cells with various concentrations of LiOH as the catholyte. (b) Effect of $LiClO_4$ addition on the discharge-charge performance of hybrid Li-air cells. Reprinted from ref. 82.

Hybrid Li-air cells with varying amounts of LiOH in the catholyte have also been studied by Zhou *et al.*[83] They found that the cell voltage and the internal resistance decrease with an increasing concentration of LiOH. The cell voltage is related to the ratio of OH^-/O_2, obeying the Nernst equation. The effect on internal resistance is due to the low ionic conductivity of the electrolyte.

Other than $LiClO_4$, salts like $LiNO_3$ and LiCl are also widely used in hybrid Li-air batteries with an alkaline catholyte. The lithium-supporting salt will also suppress the dissolution of LiOH, helping to decrease the pH value of the catholyte upon discharge and keep the solid electrolyte stable. For example, Imanishi *et al.*[84] studied the LiCl-LiOH-H_2O catholyte with saturated LiCl in hybrid Li-air batteries. The pH value of the catholyte was within a range of 7-9 due to the high concentration of Li^+ in the solution suppressing the dissolution of LiOH, which is quite favorable for the LTAP membrane. However, the drawback of a high concentration of LiCl in the catholyte is that it will decrease the solubility of LiOH, leading to more serious clogging of the air electrode by the discharge product LiOH.

1.7.2 Catalyst selection

A variety of non-noble-metal catalysts can be used in hybrid Li-air batteries with an alkaline catholyte, including carbon materials, transition-metal oxides, *etc*. An oxygen-rich carbon material composed of graphene oxide and carbon nanotubes was utilized as the catalyst for hybrid Li-air batteries.[85] Short-term discharge and charge of the battery was realized. Based on density functional theory (DFT) computational studies, the authors proposed that oxygen functional groups promote the absorption of O_2 on the graphene oxide (GO) sheets and that in such a case, the four-electron pathway becomes favorable. However, oxygen functional groups promote the decomposition of carbon materials at high voltage during the charging process. Zhou *et al.*[86] utilized metal-free graphene nanosheets (GNSs) as the bifunctional catalyst inside hybrid Li-air batteries.

The cell structure and the catalytic mechanism are shown in Figure 1.10a. The GNSs possess both high electrical conductivity and large surface area. The catalytically active sites were believed to be the edge and defect sites on the carbon surface. Oxygen and electrolyte could access those catalytically active sites from both sides of the GNSs. The cycling performance of GNSs is shown in Figure 1.10b. While the discharge voltage decreased slightly by 0.2 V after 50 cycles, the charge voltage increased by 0.4 V. This degradation was due to the oxidation of the GNSs in the high-voltage, oxidizing charge process. After heat-treatment, the GNSs showed quite stable discharge and charge performance as shown in Figure 1.10c. The charge voltage only increased by 0.16 V after cycling. The high-temperature treated graphene had better stability upon cycling. With many oxygen-containing functional groups on the GNSs, carbon can oxidize easily. After a high-temperature treatment, most oxygen functional groups are removed, which makes graphene more stable at high voltages.

Xing *et al.*[87] developed a nitrogen-doped carbon nanotube array (N-CNTAs) on carbon fiber paper as a metal-free catalyst in hybrid Li-air batteries. The SEM image of the N-CNTAs is shown in Figure 1.11a. The N-CNTAs were grown by a plasma enhanced chemical vapor deposition (PECVD) method on a Toray carbon paper with Ni catalyst. The nitrogen-doped carbon nanotube arrays demonstrated considerable catalytic activity toward ORR, which is due to the nitrogen functional groups on the carbon nanotubes. The N-CNTAs were like bamboo shoots on the top layer of carbon fibers. The inner carbon fibers were free of the N-CNTAs due to the low concentration of gases, which could not access inner carbon fibers during the PECVD process. The electrochemical performance of N-CNTAs was evaluated in a hybrid Li-air battery as shown in Figure 1.11b. The initial round-trip overpotential was 1.35 V. After 20 cyles, this value increased to 1.58 V. This comparison shows the N-CNTAs have good cycling stability with high cell efficiency comparable to that that of Pt catalyst.[79]

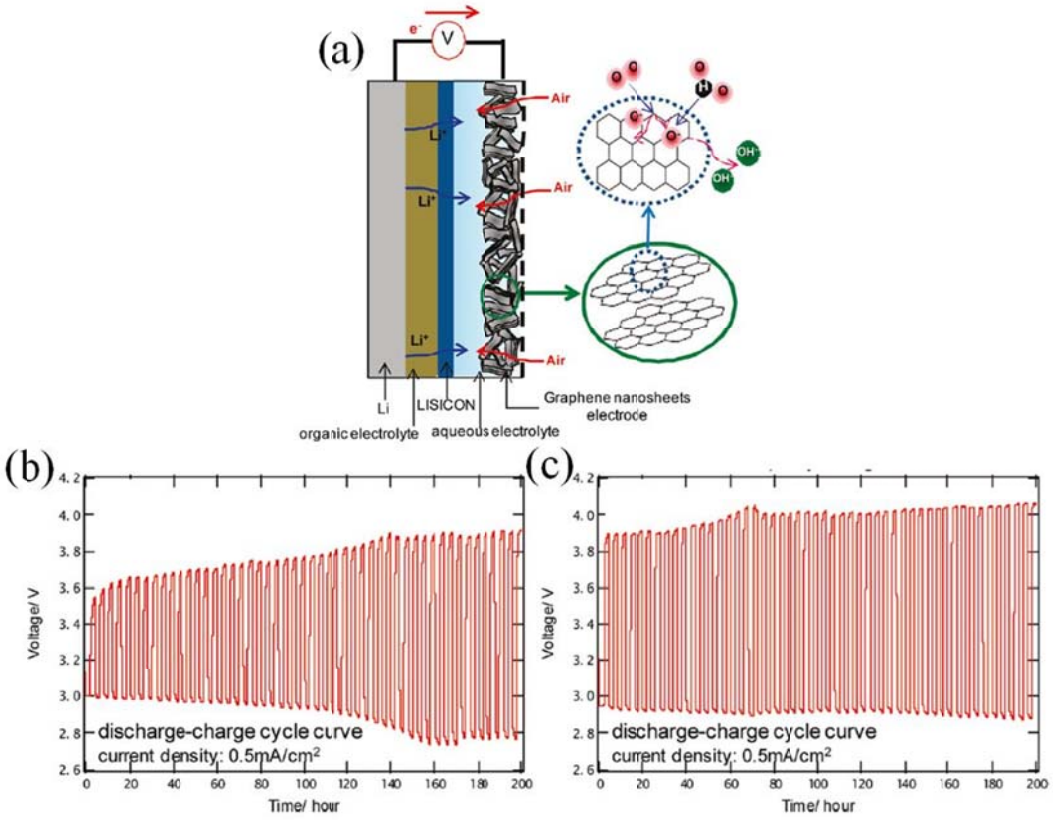

Figure 1.10. (a) Structure of the rechargeable the hybrid Li-air battery with GNSs catalyst. Charge-discharge voltage profiles of (b) GNSs and (c) heat-treated GNSs. Reprinted from ref. 86.

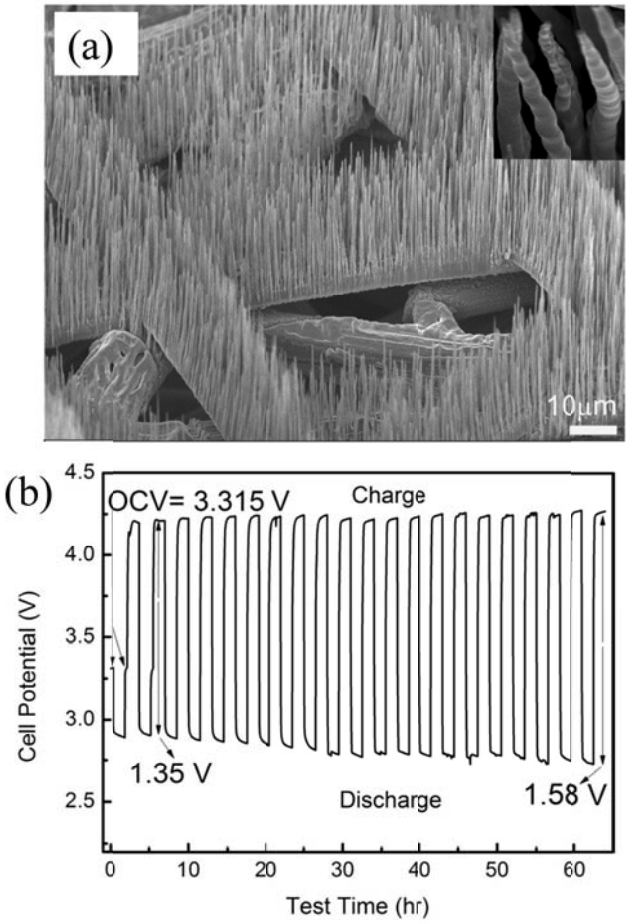

Figure 1.11. (a) SEM image of N-CNTAs grown on carbon fiber paper. (b) Battery cycling performance with N-CNTAs grown on carbon fiber paper as the catalyst. Reprinted from ref. 87.

Copper was first utilized in the lithium-air fuel cell by Zhou *et al.*[88] to catalyze the ORR by the copper-corrosion mechanism. The catalytic process begins with copper corrosion:

$$2\ Cu + ½\ O_2 = Cu_2O$$

Afterwards, Cu_2O is reduced by obtaining electrons from the external circuit:

$$Cu_2O + H_2O + 2e^- = 2\ Cu + 2\ OH^-$$

The overall reaction is a typical O_2 electrochemical reduction on copper：

$$½\ O_2 + H_2O + 2e^- = 2\ OH^-$$

However, copper does not have any OER activity. Only a so called “lithium-air fuel cell” was demonstrated.

To make a bifunctional catalyst, a composite catalyst containing perovskite $Sr_{0.95}Ce_{0.05}CoO_{3-\delta}$ loaded with copper nanoparticles (SCCO-Cu) was developed by Kim *et al.*[89] A surface Co^{4+}/Co^{3+} couple is known to be a good OER catalyst. The ORR performance of the SCCO-based catalyst is better than that of the carbon black Vulcan XC-72 at high current densities (> 0.1 mA cm^{-2}) and even close to that of the 50% Pt/carbon-black catalyst. The improved performance of the SCCO-Cu was due to the synergetic effect of SCCO and copper.

TiN was also utilized in a hybrid Li-air battery with an alkaline electrolyte, and the influence of TiN particle size was studied.[90] The SEM images of micro- and nano-sized TiN particles are shown in Figure 1.12a and b. The BET surface area of the micro and nano-sized particles was measured to be 12 and 291 $m^{-2}\ g^{-1}$, respectively. Nanosize TiN was reported to have a higher discharge voltage and better stability than micron-size TiN, as shown in Figure 1.12c. The difference in catalytic activity was caused by the different ORR pathways on the surface of the two catalysts. The ORR catalyzed by micron-sized TiN proceeds via the 2-electron pathway in a consecutive manner, with the reduction of HO_2^- starting at a higher electrode potential. On the other hand, the ORR catalyzed by nano-sized TiN proceeds via a dual-path, where the two serial ‘‘$2e^-$’’ steps proceed with smaller intervals and manifest in an overall mixed appearance by the coexistence of the parallel and serial ‘‘$2e^-$’’ steps. In other words, the reduction of HO_2^- starts more immediately after the reduction of O_2 to HO_2^- for the nano-sized TiN without showing the overall distinguishable steps.

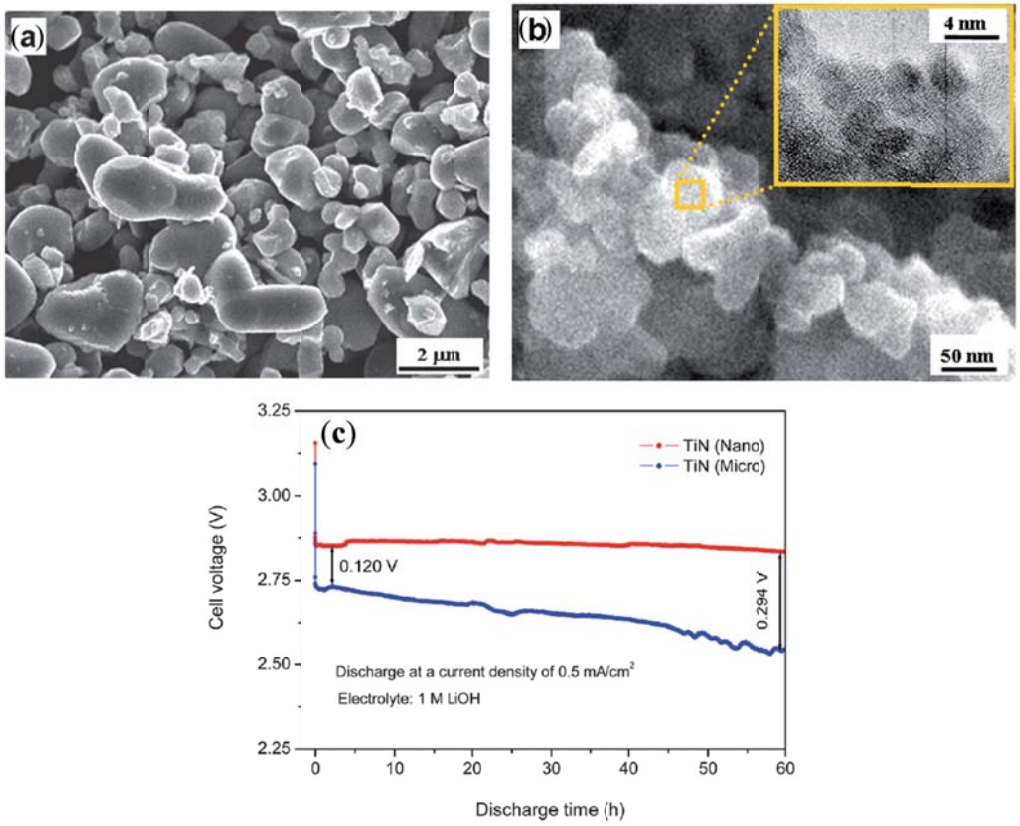

Figure 1.12. SEM images of (a) micro- and (b) nano-size TiN particles. (c) Discharge curves of hybrid Li-air fuel cells using these TiN particles as cathode catalysts. Reprinted from ref. 90.

1.7.3 Cell set-up

In hybrid Li-air batteries with alkaline catholyte, the discharge product LiOH has a very low solubility in water, which means that inactive and insulating LiOH could deposit on the air electrode. One way to solve this problem is to develop a flow-through operating mode as in a fuel cell, in which the generated LiOH is separated from the system during the discharge process.[16] In fact, this operating mode is similar to one of the possible modes for a H_2–O_2 fuel cell, where generated H_2O during the discharge process is used to prepare H_2.[16]

There is another degradation mechanism related with the alkaline catholyte. CO_2 from air tends to react with the alkaline catholyte touching the catalyst layer, producing insoluble Li_2CO_3 on the catalyst layer in the process. Since common catalysts have relatively low surface areas (typically < 100 m^2 g^{-1}), the active surface area can be easily blocked by deposited Li_2CO_3. One way to solve this problems is to install a device to filter the air to eliminate CO_2. Another way to solve this problem is to have a layer of an anion conducting polymer on the air-electrode surface.[4] This polymer layer helps not only to block CO_2 in the air from coming into the catholyte, but also to conduct OH^- ions formed during the ORR process. The anion-conducting polymer also helps to eliminate the deposited LiOH on the air-electrode surface. LiOH will be stored in the catholyte compartment instead of on the surface of the catalyst layer. Much longer discharge performance was achieved by utilizing this method with an air electrode in an alkaline electrolyte.[4] The use of high surface area N-doped mesoporous carbon can also allieviate the Li_2CO_3 deposition to some extent.

For the solid electrolyte, the discharge process accompanies the accumulation of LiOH in the catholyte, which will eventually deposit on the solid electrolyte and block Li^+-ion transport. One way to solve this problem is to deposit a layer of Li^+-ion conducting polymer on the solid electrolyte to conduct Li^+ ions as well as to eliminate the deposition of LiOH on the surface of the solid electrolyte.[4]

1.8 OBJECTIVES FOR THIS DISSERTATION

The primary objective of this dissertation is to solve two persistent issues with hybrid Li-air batteries: development of (i) catholytes that can avoid corrosion of the solid electrolyte and (ii) efficient, inexpensive electroctalysts for the oxygen reduction reaction (ORR) and oxygen evolution reaction (OER). Accordingly, the general experimental methods are described in chapter 2. In chapter 3, a phosphate buffer catholyte consisting of phosphoric acid and lithium dihydrogen phosphate is demonstrated as a promising catholyte for hybrid Li-air batteries. Phosphoric acid provides high capacity in hybrid Li-

air batteries, but it will corrode the solid electrolyte easily if used alone. Thus, lithium dihydrogen phosphate is added into phosphoric acid to keep a moderate pH and increase the ionic conductivity of the catholyte. The resulting phosphate buffer catholyte helps to keep the solid electrolyte stable in hybrid Li-air batteries. Later, we found the capacity of phosphoric acid can be increased by utilizing up to three protons in the phosphoric acid, which is presented in chapter 4. An *in situ* pH measurement method is developed to prove that the battery chemistry is the consumption of the three protons in phosphoric acid one by one.

Two major issues limiting the conversion efficiency and power density of hybrid Li-air batteries are identified to be lack of efficient OER catalysts and high internal resistance associated with the solid electrolyte. In this context, a nanocrystalline IrO_2 is employed as the OER catalysts to lower the charge voltage by 0.11 V at a current density of 2 mA cm^{-2}. In addition, the large internal resistance has been substantially reduced by increasing the operating temperature to 40 °C and employing a more conductive solid electrolyte. These achievements are described in chapter 5.

In chapters 6 and 7, a novel, decoupled ORR and OER air electrode design is shown to improve the catalytic activity and stability of both electrodes in hybrid Li-air batteries. Mesoporous $NiCo_2O_4$ nanoflakes are directly grown onto a nickel foam (NCONF@Ni) to serve as the decoupled OER electrode. The direct "grow on" strategy eliminates the involvement of vulnerable carbon or binder in the highly oxidizing charging process to ensure the durability. For the decoupled ORR electrode, a nitrogen-doped mesoporous carbon (NMC) with extremely high surface area (1520 m^2 g^{-1}) and optimized nitrogen doping content (3.9 wt. %) is loaded onto a hydrophobic carbon fiber paper to serve as the ORR catalyst. The high surface area of the N-doped mesoporous carbon provides a large number of catalytically active sites and fast electrolyte/oxygen diffusion, lowering the reaction overpotential. The nitrogen functional groups are highly active and durable as each of them is anchored onto the carbon surface. The large internal mesoporous volume of the NMC particles helps it survive from Li_2CO_3 deposition

resulting from CO_2 ingression. Although the outside surface of NMC particles may be covered by inactive and insulting Li_2CO_3, the large internal surface area can still facilitate the ORR. In addition, compared to many so-called "metal-free" catalysts, which actually may contain small amounts of metals from the synthesis process, the NMC used here is totally free of metals through the whole synthesis process and truly cost-effective for practical applications. The highly mesoporous NMC exhibits activity similar to but stability much better than that of the noble-metal Pt/C catalyst. With this decoupled configuration, a variety of other non-noble or metal-free catalysts could play the role of ORR without worrying about their stability in the high-voltage charge process. For example, we have also developed a 3-D O- and N- doped carbon nanoweb as a highly active metal-free catalyst for ORR in hybrid Li-air cells. Finally, all these challenges and approaches are summarized in chapter 8.

Chapter 2: General experimental procedures

2.1 MATERIALS SYNTHESIS

The synthesis procedures for the catalysts used in the hybrid Li-air batteries are reported in each individual chapter.

2.2 MATERIALS CHARACTERIZATION TECHNIQUES

The general characterization techniques are presented in the following sections. Other specific characterization techniques can be found in specific chapters.

2.2.1 X-ray diffraction (XRD)

XRD data were collected with a Philips X-ray diffractometer (PW 1830 + APD 3520) equipped with Cu Kα radiation. The crystalline phases were determined by comparing the XRD patterns with JCPDS cards.

2.2.2 Surface area and pore size measurements

N_2 physisorption was performed on a volumetric sorption analyzer (NOVA 2000, Quantachrome) at 77 K. Prior to measurement, the sample was purged with flowing N_2 at 423 K for 2 h. The specific surface area was calculated using the Brunauer–Emmett–Teller (BET) method from the nitrogen adsorption data in the relative pressure range (P/P0) of 0.06–0.20. The total pore volume was determined from the amount of N_2 uptake at a relative pressure of P/P0 = 0.95. The pore size distribution plot was derived from the adsorption branch of the isotherm based on the Barrett–Joyner–Halenda (BJH) model.

2.2.3 Thermogravimetric analysis (TGA)

The thermal stabilities of the materials synthesized were studied by TGA with a Perkin-Elmer TGA 7 Thermogravimetric Analyzer at a fixed heating rate in flowing air.

2.2.4 Scanning electron microscopy (SEM) and Energy dispersive X-ray spectroscopy (EDS)

Particle size and morphology observations were conducted with a FEI Quanta 650 SEM or a Hitachi S-5500 SEM. EDS spectra or mappings were obtained by utilizing the energy dispersive spectrometer attached to the SEM.

2.2.5 Transmission electron microscopy (TEM)

The TEM characterizations were carried out with a JEOL 2010F transmission electron microscope, which enables a resolution of 0.19 nm at an accelerating voltage 200 kV.

2.2.6 X-ray photoelectron spectroscopy (XPS)

XPS is a surface analysis technique which measures the elemental composition at the top ~ 10 nm of the sample. The sample surface is irradiated with a beam of X-rays and the kinetic energy and number of escaping electrons from the sample surface are measured. The XPS data were conducted with a Kratos Analytical spectrometer. The deconvolution of the XPS spectrum was performed with CasaXPS solftware with Gaussian-Lorentzian functions and a Shirley background.

2.3 ELECTROCHEMICAL CHARACTERIZATION

2.3.1 Rotating disk electrode (RDE)

The intrinsic catalytic activities of the catalysts synthesized were compared by linear sweep voltammetry (LSV) and cyclic voltammetry (CV) in a standard rotating disk electrode (RDE) setup with an Autolab PGSTAT302N potentiostat (Eco Chemie B.V.). A glassy carbon electrode with a diameter of 5 mm was polished to a mirror-like finish before serving as the working electrode. The counter electrode was a Pt mesh. A saturated calomel electrode (SCE) worked as the reference electrode. The catalyst ink was made by sonicating the catalyst powder in ethanol. The catalyst ink was then loaded

onto the glassy carbon electrode followed by drying in air. 5 μL of Nafion solution (0.5 wt. %) was then dropped onto the top of the catalyst layer to form a protective layer.

2.3.2 Half-cell test

The half-cell tests were conducted in a home-made three-electrode half-cell in which 0.5 M LiOH + 1 M $LiNO_3$, a Hg/HgO electrode, and a platinum flag were used, respectively, as the electrolyte, reference electrode, and counter electrode.

2.3.3 Full-cell test

A home-made PTFE layered battery mould was used to carry out the full cell test. For heating purpose, the anode and cathode plates can be replaced by stainless steel. The anode side was assembled in an argon filled glove box and then combined with the cathode side in air. The anode side consisted of a nickel foam current collector, a lithium metal foil, and the organic carbonate electrolyte (1 M $LiPF_6$ in ethylene carbonate (EC) / diethylcarbonate (DEC) (1:1 v/v)). The cathode side consisted of catholyte, an air electrode (0.76 × 0.76 cm) containing various catalysts, and a platinum mesh current collector. A LTAP membrane (0.15 mm thick, $\sigma = 1\times10^{-4}$ S cm^{-1} or 2.5×10^{-4} S cm^{-1}, 0.76 cm × 0.76 cm, OHARA Inc., Japan) was used as the separator. The cathode side of the hybrid cell was purged with water-saturated air during operation to suppress the evaporation of water from the catholyte.

2.3.4 Discharge and charge tests

The discharge and charge tests were conducted with an Arbin BT 2000 battery cycler. The discharge and charge times were determined by the electrolyte and catalysts used. A current density of 0.5 mA cm^{-2} is mostly used. Different charge or discharge current densities may apply to test the rate capability of catalysts.

2.3.5 Polarization curves

Polarization curves were obtained by sweeping the potential of the cell from the open-circuit voltage (OCV) to a certain value with a VoltaLab PGZ 402 potentiostat. It is a quick method to show the catalytic activity of different catalysts.

2.3.6 Electrochemical impedance spectroscopy (EIS)

The internal resistance was measured at open-circuit voltage (OCV) by a Solartron 1260A impedance analyzer from 2 MHz to 0.1 or 0.01 Hz with an ac voltage amplitude of 10 mV.

Chapter 3: A rechargeable hybrid Li-air battery with phosphate buffer catholyte*

3.1 INTRODUCTION

Current lithium-ion batteries with insertion-compound electrodes fall short of the high power and energy densities demanded by multifunctional portable electronic devices, electric vehicles, and grid storage.[91] Metal-air batteries, with the highest energy density of all known batteries, have the potential to provide solutions for these applications. Among the metal-air batteries, Li-air batteries offer the highest theoretical energy density (11,680 Wh/kg, excluding oxygen), rivaling that of gasoline (13,000 Wh/kg), due to the high capacity of both the electrodes and the high operating voltage of the Li-O_2 couple.[92]

Abraham and Jiang[93] reported the first rechargeable lithium-oxygen cell based on an aprotic electrolyte, which was then further developed by others.[94-97] However, most aprotic lithium-oxygen cells are operated in pure oxygen or a mixture of dry oxygen and nitrogen since the moisture in ambient environment can degrade the non-aqueous electrolyte and the lithium metal anode, resulting in poor cycle life. The lithium-air cells based on aprotic electrolytes also suffer from clogging of the porous air cathodes by insoluble products like Li_2O_2 and Li_2O. To overcome this problem, Visco *et al.*[6] proposed the use of water-stable NASICON-type solid electrolytes ($Li_{1+x+y}Al_xTi_{2-x}Si_yP_{3-y}O_{12}$ or LTAP) to protect the lithium metal anode. This idea has been applied to many hybrid lithium cells, including hybrid Li-air cells.[17, 98, 99] For example, Zhang *et al.*[67] developed a Li | PEO_{18}LiTFSI | LTAP | HOAc (90 vol %)–H_2O–LiOAc (sat) (10 vol %) | Pt-black air battery, which delivered a discharge capacity of 250 mAh g^{-1} for 15 cycles. However, the

---

* L. Li, X. Zhao and A. Manthiram, "A hybrid rechargeable Li-air battery with phosphate buffer catholyte," *Electrochem. Commun.*, 2012, **14**, 78-81.
L. Li carried out the experimental work. X. Zhao provided assistance in experimental details. A. Manthiram supervised the project. All participated in the preparation of the manuscript.

cell had to be operated at 3 atm of air to improve the utilization of acetic acid and at 60 °C to maintain low interfacial impedance. Wang *et al.*[16] proposed a Li | organic electrolyte | LTAP | 10 ml 1M KOH | Mn_3O_4 cell, but they needed to divide the aqueous electrolyte into two compartments with a cation exchange membrane (CEM) to protect the LTAP membrane from corrosion by the discharge product, LiOH.[55] Unfortunately, CEM increases the complexity and cost of the whole system.

We report here a novel hybrid Li-air battery system, in which a phosphate buffer solution is used as the catholyte with the cell configuration of Li | 1 M $LiPF_6$ in EC/DEC | LTAP | 0.1M H_3PO_4+1 M LiH_2PO_4 | Pt air. Phosphoric acid is a moderately strong acid and could corrode the LTAP membrane, if used solely. However, a phosphate buffer solution consisting of a mixture of 0.1 M phosphoric acid and 1 M LiH_2PO_4 with a net pH value of 3.14 at room temperature can avoid the corrosion of the LTAP membrane, and the results are presented here.

3.2 EXPERIMENTAL

All experiments were conducted with a PTFE-plate constructed battery mold shown in Figure 3.1. This layered battery structure consists of a nickel foam current collector, lithium foil, aprotic electrolyte (1 M $LiPF_6$ in EC/DEC (1:1 v/v)), LTAP membrane (0.15mm thick, 0.76 × 0.76 cm, OHARA Inc., Japan), aqueous catholyte (0.1 M H_3PO_4 + 1 M LiH_2PO_4), an air electrode with carbon-supported platinum catalyst (0.76 × 0.76 cm), and a platinum mesh current collector. The air electrode was prepared by spraying the catalyst ink made with Pt/C (40 wt. %, Johnson Matthey) and Nafion (5 wt. %, EW1000, Dupont) onto a 10 BA gas diffusion layer (SGL). The Pt loading and Nafion content in the air electrode were, respectively, 1.2 mg cm^{-2} and 20 wt. %. In order to protect LTAP from being reduced by lithium metal, the lithium metal and LTAP were separated with two layers of Celgard® polypropylene impregnated with the aprotic electrolyte.[98] The anode side of this cell was assembled in an argon-filled glove box and

then combined with the cathode side in air followed by adding 0.4 mL of catholyte containing 0.1 M H_3PO_4 + 1 M LiH_2PO_4.

Discharge-charge tests were conducted with an Arbin BT 2000 battery test system. Electrochemical impedance spectra (EIS) were recorded at open circuit voltage (OCV) with an impedance analyzer (Solartron 1260 A) in the frequency range of 2 MHz to 1 Hz. The ac voltage amplitude was 10 mV. Polarization curves were recorded with a potentiostat (Solartron 1287) in the potential range of OCV to 0 V with a scan rate of 5 mV s^{-1}. All tests were conducted at room temperature.

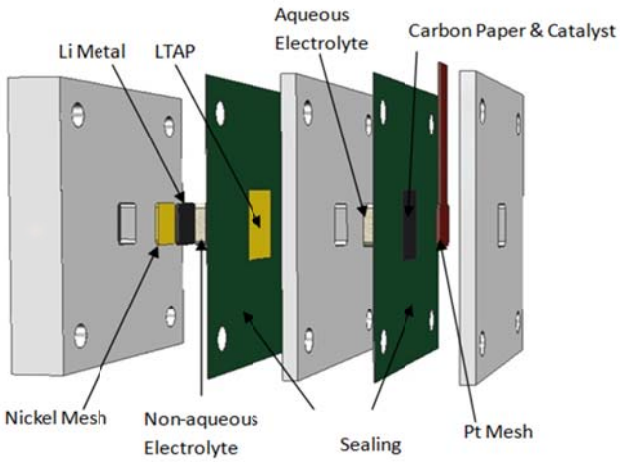

Figure 3.1. Hybrid Li-air cell consisting of a lithium metal anode, aprotic electrolyte, LTAP membrane, aqueous catholyte, and an air electrode.

3.3 RESULT AND DISCUSSION

During the discharge-charge process, the reversible electrode reactions and the overall cell reaction occur as shown below in reactions 1, 2, and 3, which are similar to those in the aqueous Li-air cell reported by Zhang *et al.*:[67]

Anode: $Li \leftrightarrow Li^+ + e^-$ (1)

Cathode: $H_3PO_4 + 1/4\ O_2 + e^- \leftrightarrow (H_2PO_4)^- + 1/2\ H_2O$ (2)

Overall : $Li + H_3PO_4 + 1/4\ O_2 \leftrightarrow LiH_2PO_4 + 1/2\ H_2O$ (3)

The forward reaction 2 refers to the oxygen reduction reaction (ORR) and the backward reaction 2 refers to the oxygen evolution reaction (OER). During discharge, O_2 diffuses to the catalyst active sites and combines with protons in the catholyte to form water. While in the aprotic electrolyte, the lithium metal anode is oxidized to Li^+ ions, which diffuse through the LTAP membrane into the catholyte to form LiH_2PO_4. During charge, water splits into oxygen and protons; while oxygen is removed as bubbles, the protons combine with $(H_2PO_4)^-$ to form phosphoric acid. Lithium ions in the catholyte diffuse back to the aprotic electrolyte and get reduced and plated onto the lithium metal anode.

Figure 3.2a shows a typical discharge-charge curve of the Li-air cell at ambient environment. The cell was discharged for three hours and then charged for three hours at 0.5 mA cm^{-2}. The observed capacity of 221 mAh g^{-1} based on H_3PO_4 (excluding the air electrode and oxygen) is 81 % of the theoretical capacity (273 mAh g^{-1}) of 3.92 mg H_3PO_4 within the catholyte. The energy density of H_3PO_4 based on the first discharge capacity and cell voltage is ~ 770 Wh kg^{-1}. The theoretical energy density of the cell based on the overall cell reaction 3 (involving Li metal and H_3PO_4, but excluding oxygen and air electrode) and a theoretical voltage of 4.27 V is 1,089 Wh kg^{-1}. Figure 3.2b shows the discharge voltage profiles of the cell at various current densities of 0.1 – 0.5 mA cm^{-2} for half an hour at each current density. The very flat discharge plateaus seen at different current densities demonstrate excellent rate capability and good electrocatalytic activity and kinetics at the air electrode. The discharge overpotential increases only slightly as the current density increases, revealing very low internal resistance and high catalytic activity of the hybrid Li-air cell presented here. Using acetic acid as the active material, Zhang *et al.*[67] achieved a discharge capacity of 250 mAh g^{-1} for 15 cycles with good rate capability up to 0.5 mA cm^{-2} at 60 °C. However, since acetic acid suffers from vaporization problems, its utilization rate is low (56 %) even under 3 atm of air.[67] In contrast, H_3PO_4 is stable and nonflammable and offers a high utilization rate of 81 % in ambient

environment. The utilization rate could increase close to 100 % with optimized cell design.

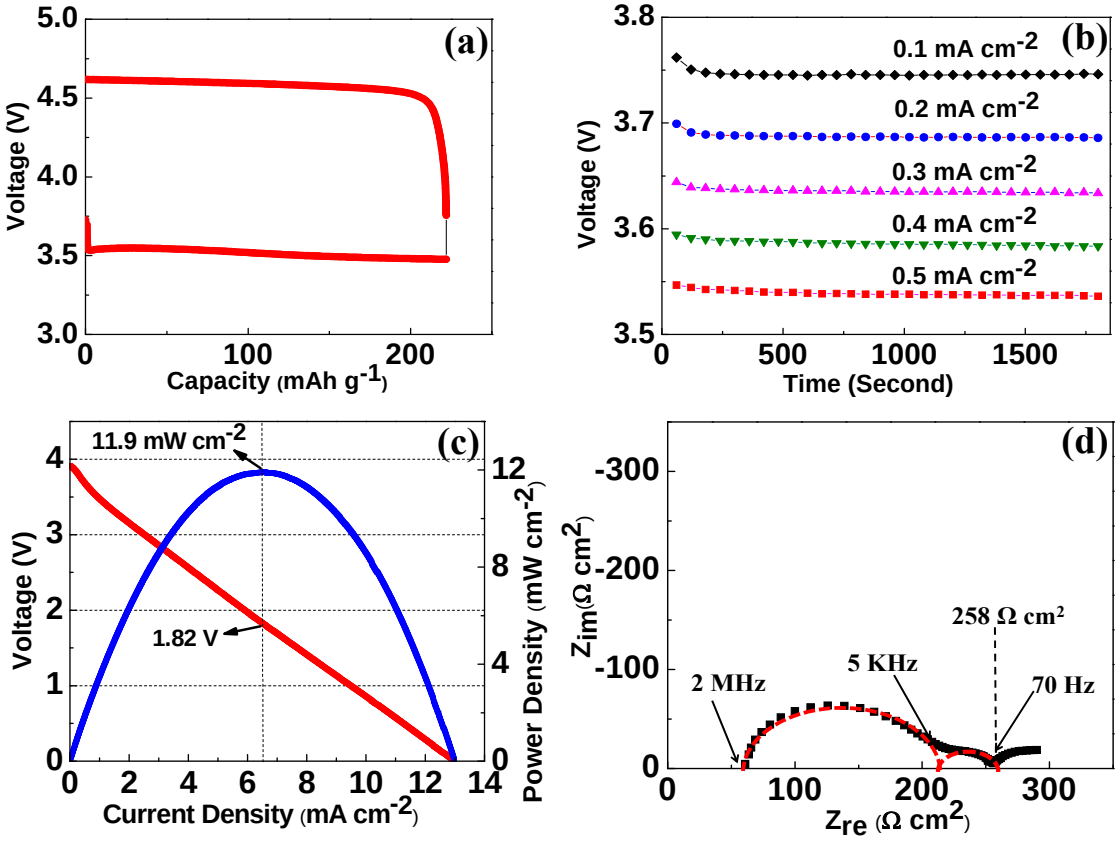

Figure 3.2. Electrochemical performance of the hybrid Li-air cell: (a) typical discharge-charge profiles at a current density of 0.5 mA cm^{-2}, (b) discharge profiles at current densities of 0.1, 0.2, 0.3, 0.4, and 0.5 mA cm^{-2}, (c) polarization curves of the hybrid Li-air cell at a scanning rate of 5 mV s^{-1}, and (d) EIS analysis of the hybrid Li-air cell. The red curve refers to the curve fitting.

Figure 3.2c shows the polarization curve of the Li-air cell obtained by a potential sweep method at a scan rate of 5 mV s^{-1} with a potentiostat. It displays a maximum power density of 11.9 mW cm^{-2} at 1.82 V, which is comparable to the lithium-air fuel cell

developed by He *et al.*[83] The peak power density could be increased by ten times if a capacitor electrode is incorporated into the cell.[100] The abrupt drop observed at the beginning of the polarization curve at low current densities is due to the activation polarization of the oxygen reduction catalyst. The rest of the polarization curve is almost linear, where the polarization is dominated by the resistance of the LTAP membrane. Compared to aprotic Li-air batteries, the hybrid Li-air battery offers much higher operating voltage and power density, which are even competitive with those of direct methanol fuel cells[101]. Figure 3.2d shows a typical impedance profile of the hybrid Li-air cell at OCV. From the intersection of the semi-circles with the real axis, we can obtain the resistances of the liquid electrolytes (R_E), the LTAP membrane (R_L), and charge transfer and interface (R_F+R_I).

Figure 3.3a shows the extended cycling performance of the Li-air cell at 0.5 mA cm^{-2} at ambient environment for 20 cycles. The charge and discharge overpotential increased from 1 to 1.3 V after 20 cycles. In order to understand the cell performance decay associated with the impedance change, the impedance profiles before and after cycling were measured, as shown by the Nyquist plots in Figure 3.3b. The total impedance increased from 258 $\Omega \cdot cm^2$ to 292 $\Omega \cdot cm^2$ after 20 cycles. The impedance profile shows a large semicircle in the high frequency range and a small semicircle in the low frequency range. Based on the impedance data, the resistances of the liquid electrolytes (R_E), LTAP membrane (R_L), and charge transfer and interface (R_F+R_I) were obtained, respectively, as 57, 155, and 46 $\Omega \cdot cm^2$ before cycling, which increased to 58, 157, and 77 $\Omega \cdot cm^2$ after 20 cycles. The first semicircle corresponds to the impedance of the LTAP plate, which is close to the theoretical resistance (150 $\Omega \cdot cm^2$) of the LTAP membrane with a thickness 0.015 cm and a conductivity of 1×10^{-4} S cm^{-1} at room temperature. Hasegawa *et al.*[63] pointed out that the LTAP plate will decompose and show high resistance in strong acidic or basic solutions. Wang *et al.*[55] also reported the instability of the LTAP plate in strong alkaline solutions and tried to stabilize the cell by dividing the aqueous electrolyte into two compartments with a cation exchange

membrane (CEM) to protect the LTAP membrane from corrosion. While in our cell, the R_E and R_L values remained almost constant after 20 cycles, indicating that the robustness of this hybrid Li-air system is mostly related to the stability of the LTAP membrane in the moderately acidic buffer electrolyte.[68] The R_F+R_I value increased by 31 Ω cm^2 after 20 cycles, which is due to the oxidation and degradation of the air electrode during the high-voltage charge process. This problem could be addressed by developing better bifunctional electrocatalysts to lower the charge potential.[102]

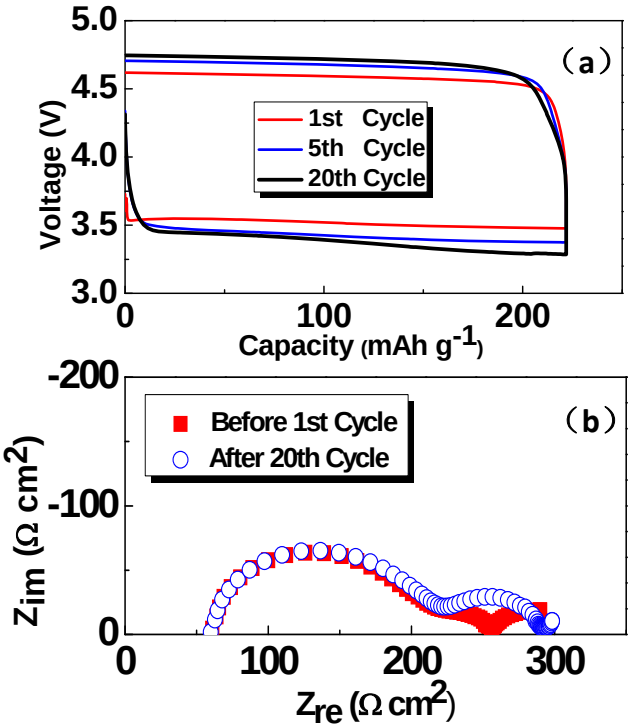

Figure 3.3. (a) Cycling performance of the hybrid Li-air cell at a current density of 0.5 mA cm^{-2} under ambient environment and (b) Nyquist plots at OCV before and after 20 cycles.

3.4 CONCLUSION

In summary, we have successfully developed a new type of hybrid Li-air battery

with high capacity and voltage, consisting of lithium metal in aprotic electrolyte as the anode, an air electrode in an acidic phosphate buffer solution as the cathode, and a solid Li^+-ion conducting oxide as the separator. The cell exhibits a high discharge capacity of 221 mAh g^{-1} and an energy density of ~770 Wh kg^{-1} for H_3PO_4 at a current density of 0.5 mA cm^{-2} for 20 cycles with mild degradation. The cell exhibits very good stability after extended cycles in air, overcoming the instability issues of conventional aprotic Li-air batteries in ambient environment. The phosphate buffer solution proves to be a promising catholyte for this type of novel hybrid Li-air batteries.

Chapter 4: Polyprotic acid catholyte for high capacity hybrid Li-air batteries*

4.1 INTRODUCTION

Lithium metal has been widely considered as the most promising anode for high energy density batteries because it is the lightest metal with the most negative reduction potential. The idea of incorporating air as the cathode and the lithium metal as the anode was first realized by Abraham *et al.* in 1996.[93] The energy density of Li-air batteries can be comparable to that of gasoline, which makes them a promising candidate to replace internal combustion engines in vehicles.[92] However, a number of challenges are associated with aprotic Li-air batteries based on organic electrolytes, such as low efficiency and poor rechargeability. Visco *et al.*[6] pursued hybrid lithium-air batteries by utilizing NASICON-type solid electrolytes ($Li_{1+x+y}Al_xTi_{2-x}Si_yP_{3-y}O_{12}$ or LTAP) to protect the lithium metal anode. Since the LTAP membrane is a single lithium-ion conductor and blocks the contaminants from air, the hybrid Li-air batteries have shown good rechargeablity and efficiency.[4, 103]

There are basically two kinds of catholytes classified by the battery chemistry for hybrid Li-air batteries: neutral or basic catholyte and acidic catholyte. In cells with neutral or basic catholytes, the cell reaction is $2Li+1/2O_2+H_2O \leftrightarrow 2LiOH$. As the discharge process progresses, the catholyte encounters a soaring alkalinity quickly by becoming saturated with LiOH, which is highly corrosive to the LTAP membrane. For instance, the deposited LiOH solid blocks the lithium-ion tunnels in the LTAP membrane and clogs the air inlet pores on the porous air cathode, while the CO_2 from air reacts with LiOH to form inactive Li_2CO_3.[8104] Accessorial components are needed to overcome these

---

* L. Li, X. Zhao, Y. Fu and A. Manthiram, "Polyprotic acid catholyte for high capacity hybrid Li-air batteries," *Phys. Chem. Chem. Phys.*, 2012, **14**, 12737-12740.
L. Li carried out the experimental work. X. Zhao and Y. Fu provided assistance in experimental details. A. Manthiram supervised the project. All participated in the preparation of the manuscript.

problems.[4, 55] In cells with acidic catholyte, the cell reaction is $2Li+1/2O_2+2HA\leftrightarrow 2LiA+H_2O$, where A is a weak acid anion like $(CH_3COO)^-$ or $(H_2PO_4)^-$.[65, 67] Although strong acids like HCl have high theoretical capacity, their strong acidity makes the LTAP membrane vulnerable.[63] The oxygen reduction reaction (ORR) in acidic solution is 0.8 V higher than that in basic solution. As the discharge process progresses, the catholyte becomes less acidic, which is less corrosive to the LTAP membrane. We have reported the use of a phosphate buffer solution containing 0.1M H_3PO_4 + 1M LiH_2PO_4 with a moderate pH for hybrid Li-air batteries with high capacity and stability.[65] However, only one proton of the phosphoric acid was utilized in the buffer solution during the discharge process. With an aim to increase the energy density of the hybrid Li-air batteries further, we present here the successful utilization of multiple protons per molecule of H_3PO_4.

In this work, three protons of phosphoric acid are effectively utilized to achieve a high capacity with the hybrid Li-air batteries. We use here 0.1 M H_3PO_4 + 1 M Li_2SO_4 as the catholyte to eliminate the influence of protons from LiH_2PO_4. The air cathode consists of 1.2 mg cm^{-2} of IrO_2 as an oxygen evolution reaction catalyst and 1.2 mg cm^{-2} of Pt as an oxygen reduction reaction catalyst. The discharge voltage profile is interestingly in synchronism with the pH change of the catholyte, confirming that the discharge battery chemistry involves the consumption of phosphoric acid. The operating voltage of hybrid Li-air batteries with acidic catholyte is about 1 V on average higher than that of aprotic Li-air batteries. The rechargeability and stability are also better because the lithium metal anode and aprotic electrolyte are protected from water by the LTAP membrane.[99]

4.2 EXPERIMENTAL

All experiments were conducted with a layered battery structure described in chapter 3 (Figure 3.1). 1 M $LiPF_6$ in EC/DEC (1:1 v/v) was used as the electrolyte with the Li anode and 0.1 M H_3PO_4+1M Li_2SO_4 was used as the catholyte. A LTAP

membrane (0.15 mm thick, 0.76 × 0.76 cm, OHARA Inc., Japan) was used as the separator between the two electrolytes. The air electrode was prepared by spraying the catalyst ink made with Pt/C (40 wt. %, Johnson Matthey), IrO_2, and Nafion (5 wt. %, EW1000, Dupont) onto a 10 BA gas diffusion layer (SGL). The Pt loading, IrO_2 loading, and Nafion content in the air electrode were, respectively, 1.2 mg cm^{-2}, 1.2 mg cm^{-2}, and 20 wt. %. IrO_2 powder was prepared by the modified Adams fusion method.[105] Two layers of Celgard® polypropylene separator were placed between lithium metal anode and the LTAP membrane. The anode side was assembled in an argon-filled glove box, and then combined with the cathode side outside the glove box by adding 0.2 mL catholyte containing 0.1 M H_3PO_4 + 1 M Li_2SO_4 (the pH measurement of the catholyte during the discharge process was conducted in a cell containing 1 mL catholyte). The cathode side of the cell was purged with water-saturated air during cycling test to suppress the evaporation of water from the catholyte.

An Arbin BT 2000 battery test system was used to conduct discharge-charge tests. Electrochemical impedance spectra (EIS) were recorded at open circuit voltage (OCV) with an impedance analyzer (Solartron 1260 A) in the frequency range of 2 MHz to 1 Hz. The ac voltage amplitude was 10 mV. All pH measurements were conducted with a HI 2223 pH benchtop meter controlled by HANNA HI92000 Windows® compatible software and a PerpHecT® ROSS® combination micro pH electrode. Before each test, the pH electrode was calibrated with three pH buffers: 1.68, 4.01, and 7.01. All tests were conducted at room temperature.

4.3 RESULT AND DISCUSSION

The battery chemistry is illustrated in Figure 4.1, which can be described as follows:

$$3Li+H_3PO_4 + 3/4\ O_2 \leftrightarrow Li_3PO_4 + 3/2\ H_2O$$

During the discharge process, lithium metal at the anode is oxidized into Li^+ ions, which are released into the aprotic electrolyte and diffuse through the LTAP membrane

into the catholyte. While at the air cathode, O_2 is reduced and combines with the protons to form water. Li^+ ions play the role of balancing the negatively charged phosphate ions produced by the consumption of protons in the catholyte. During the charge process, water splits into oxygen and protons; the Li^+ ions in the catholyte diffuse back into the aprotic electrolyte and are reduced and plated onto the lithium metal anode. The charge balance in the catholyte is maintained by the protons produced.

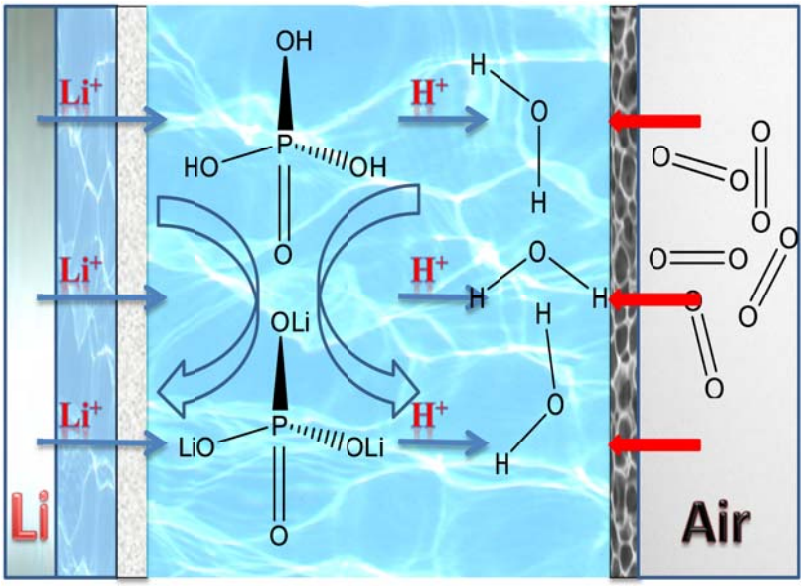

Figure 4.1. Schematic diagram of the structure and operatng principle of the hybrid Li-air battery based on phosphoric acid catholyte.

The black curve in Figure 4.2 shows the typical three-stage discharge curve of a high-capacity hybrid Li-air cell, corresponding to the following three-step reactions:

$$Li + H_3PO_4 + 1/4\ O_2 = LiH_2PO_4 + 1/2\ H_2O \quad (1)$$

$$Li + LiH_2PO_4 + 1/4\ O_2 = Li_2HPO_4 + 1/2\ H_2O \quad (2)$$

$$Li + Li_2HPO_4 + 1/4\ O_2 = Li_3PO_4 + 1/2\ H_2O \quad (3)$$

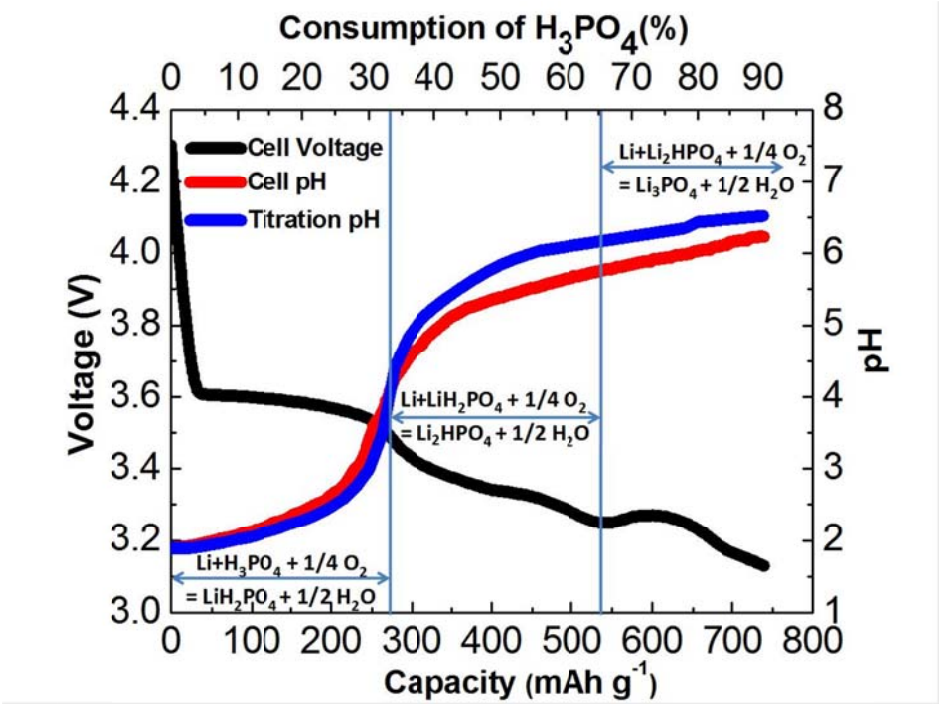

Figure 4.2. Black curve: a typical discharge voltage curve showing the three-stage oxygen reduction reactions; red curve: pH change of the catholyte associated with the three-stage discharge process; blue: titration curve of 0.1 M H_3PO_4 in 1 M Li_2SO_4 against LiOH.

There was in total number of 1.96 mg H_3PO_4 in the catholyte. With the discharge-charge cycling, the cell was discharged for five hours and then charged for five hours at a constant current of 0.5 mA cm^{-2}. Hybrid Li-air batteries do not experience an abrupt voltage drop or increase at the end of discharge or charge. Thus, we do not control the discharge and charge times via voltage cutoff. Instead, we control the discharge and charge times themselves which can be easily converted to capacity. Similar methods and plots have been presented in the literatues.[4, 67, 86] During discharge, the first stage between 0 and 273.5 mAh g^{-1} on the discharge curve represents reaction (1), the second stage between 273.5 mAh $g^{-1}$and 547 mAh g^{-1} corresponds to reaction (2), and the third stage

between 547 mAh g^{-1} and 740 mAh g^{-1} refers to reaction (3). There are two equivalent points at 273.5 mAh/g and 547 mAh g^{-1}, which signal the transitions from reaction (1) to reaction (2) and then from reaction (2) to reaction (3), respectively. The obtained 740 mAh g^{-1} capacity is 90.2% of the theoretical capacity of H_3PO_4 (820 mAh g^{-1}), considering all three protons in H_3PO_4 are active for the oxygen reduction reaction. The theoretical capacity of H_3PO_4 is even higher than HCl (735.2 mAh/g). The achieved energy density of H_3PO_4 based on the discharge capacity (740 mAh g^{-1}) and cell voltage (3.3 V on average) is 2442 Wh kg^{-1}. The ultra-high energy density and the possibility to build aqueous cathodes into a flow-through mode endow the hybrid Li-air batteries with great potential for large-scale stationary electrical energy storage.[106, 107]

The discharge battery chemistry was assumed to be a consumption process of the three protons of H_3PO_4 by reactions (1), (2) and (3). In order to validate this mechanism, the pH change of the catholyte during the discharge process was recorded (red curve in Figure 4.2) and was compared with the titration profile of 0.1M H_3PO_4 in 1M Li_2SO_4 against LiOH (blue curve in Figure 4.2). These two methods basically indicate the same pH values at different consumption points of H_3PO_4. An apparent deviation in pH starts at the first equivalent point, which is because of the mass transport effect. While the solution was well stirred during the titration process, the catholyte in the cell was static. The oxygen reduction reaction at the interface of the air electrode and the catholyte consuming the protons caused the pH value at the interface higher than that at the center of the catholyte, where the micro pH electrode stayed. The deviation starts from the first equivalent point because the produced Li_2HPO_4 has low solubility with a low mobility of protons compared to that with H_3PO_4 and LiH_2PO_4, where the mass transport effect dominates. The increasing pH and their synchronism with the discharge curve clearly show that the dominating battery reaction during the discharge process is the consumption of the three protons of H_3PO_4. In comparison to the unclear battery chemistry and detrimental side reactions in aprotic Li-air batteries,[108, 109] the staged pH change in the hybrid Li-air batteries employing phosphoric acid catholyte reveals clearly

the battery reaction process, thereby enabling easy operation and monitoring of the cells, which is critical for large-scale battery systems.

The acid dissociation constants of the three protons in phosphoric acid are quite different from each other, which results in the increasing pH curves in Figure 4.2. The acid dissociation constants of phosphoric acid are: pK_{a1}=2.16, pK_{a2}=7.21,and pK_{a3}=12.32 at 25 °C.[110] The first point (pH=1.9) on the red curve corresponds to the initial 0.1M H_3PO_4 in 1M Li_2SO_4. As soon as the discharge process begins, $(H_2PO_4)^-$ is produced. The solution becomes a buffer containing H_3PO_4 and its conjugate base $(H_2PO_4)^-$. The buffer is resistant to changes in pH, thus we see a relatively flat pH curve before the first equivalent point. The flat pH curve also leads to a flat discharge profile before the first equivalent point in accordance with the Nernst equation $E=E^o$-0.059 pH, where the pressure of oxygen is taken to be unity and the polarization losses are assumed to be constant.[111] At the first equivalent point (pH=4.1), all of the H_3PO_4 has been converted to $(H_2PO_4)^-$, which is accompanied by a sharp rise in pH because of the large difference between pK_{a1} and pK_{a2}. As the discharge process continues beyond the first equivalent point, $(H_2PO_4)^-$ is consumed and $(HPO_4)^{2-}$ is produced. It is called the second buffer zone because the catholyte contains $(H_2PO_4)^-$ and its conjugate base $(HPO_4)^{2-}$. The vanishing of the sharp rise in pH after the second equivalent point is due to the suppression of the dissociation and hydrolysis of Li_3PO_4 by the high concentration of Li_2SO_4. It is the hydrolysis of Li_3PO_4 that contributes to the alkalinity of Li_3PO_4 in water.[112] In the third buffer zone starting at the second equivalent point (pH=5.8), $(HPO_4)^{2-}$ and its conjugate base $(PO_4)^{3-}$ remain in the catholyte. The discharge ends with 90.2 % of the total protons in H_3PO_4 consumed. The ending pH (=6.3), which is nearly neutral and far below the pH value (>12) of a Li_3PO_4 single salt solution, avoids the corrosion of LTAP membrane, ensuring long-term stability of the cell. The pH value of the catholyte decreases to the initial value on charging, accompanied by a reversible pH change within the catholyte.

In most of the literature, the obtained discharge curves of hybrid and aqueous Li-air cells are flat because buffers were used as the catholyte. For example, Zhang *et al.*[68]

used lithium acetate (LiAc) saturated acetic acid (HAc) as the catholyte for aqueous Li-air batteries. The catholyte is a buffer containing HAc and its conjugate base LiAc. It is resistant to the change in pH during cycling, which leads to flat discharge and charge voltage profiles. In our previous work, the phosphate buffer containing H_3PO_4 and its conjugate base LiH_2PO_4 also showed flat discharge and charge voltages.[65] In this work, the discharge process results in a large pH value change of the catholyte from about 2 to nearly 6.3. The low initial pH of the catholyte could raise the question of potential corrosion of the LTAP membrane, resulting in cell failure. However, galvanostatic cycling and impedance analysis demonstrate good electrochemical stability for the system.

Figure 4.3a shows the cycling performance of the hybrid Li-air cell at a current density of 0.5 mA cm^{-2}. As can be seen, the charge profiles show voltage plateaus that correspond well with the discharge profiles. There are only two clear stages on the charge curve because water electrolysis happens on the IrO_2 catalyst surface and is not affected by the deposited Li_3PO_4 on Pt surface, which make the discharge voltage of the third stage deviate from the second stage. The cell performance reveals only very mild degradation and potential shifts after 20 cycles, indicating the robustness of this Li-air system. In order to show the stability of this cell, the impedance of the cell was measured before and after cycling, which is shown in Figure 4.3b. According to the intersections of the impedance profiles with the real axis, the resistance of the cell is divided into: resistance of the two liquid electrolytes, bulk resistances of the LTAP membrane and the air electrode (R_E), grain boundary resistance of the LTAP membrane and air electrode (R_L), and charge transfer and interfacial resistance (R_F+R_I).[83] As can be seen, R_E increases from 46 to 66 Ω cm^2 after 20 cycles. At the same time, R_L increases slightly from 134 to 138 Ω cm^2. The increase in R_E and R_L does not result in a drastic degradation of the cell performance, indicating the feasibility of using phosphoric acid as a catholyte for high-capacity hybrid Li-air batteries. The charge transfer and interfacial impedance R_F+R_I increases from 80 to 91 Ω cm^2. This increase is not significant because IrO_2 was

added as the oxygen evolution catalyst to suppress carbon support corrosion, thus decreasing degradation in the catalytic performance of the air cathode.[113]

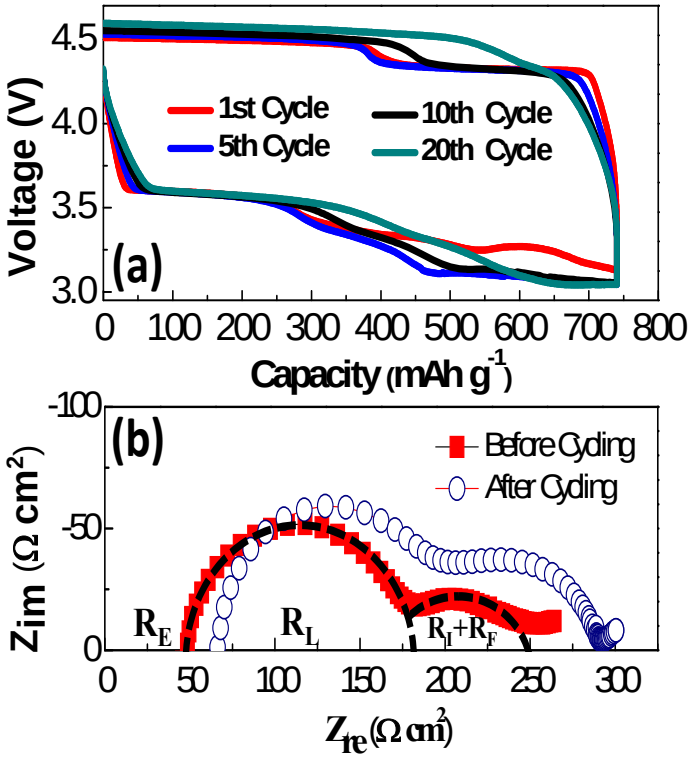

Figure 4.3. (a) Cycling performance of the hybrid Li-air cell at a current density of 0.5 mA cm^{-2} and (b) cell impedance profiles before and after the cycling test.

4.4 CONCLUSION

In conclusion, this study demonstrates the utilization of the three protons of phosphoric acid with an ultra-high capacity in hybrid Li-air batteries. Polyprotic acids like H_3PO_4 have higher theoretical capacities than light-weight strong acids like HCl, and are more compatible with the LTAP membrane since the higher dissociation constants help raise the pH value at the beginning of discharge and the suppression of the hydrolysis of Li_3PO_4 by the Li_2SO_4 supporting salt brings down the pH value towards the end of discharge. The high capacity along with the high cell voltage enables the stack

energy densities of the hybrid Li-air batteries comparable with those of redox flow batteries. The good rechargeability and electrochemical stability demonstrate the feasibility of this dual electrolyte technology; it can enable a flow-through mode system for large-scale grid-energy storage.

Chapter 5: Hybrid Li-air batteries: influence of catalyst, temperature, and solid-electrolyte conductivity on the efficiency and power density*

5.1 INTRODUCTION

Unlike the traditional metal-air batteries such as zinc-air batteries, the Li-air batteries cannot be operated with aqueous electrolytes without the protection of the lithium metal due to the vigorous reaction between lithium metal and water. To solve this problem, a water-stable Li-ion solid electrolyte was used to separate the lithium anode from the aqueous cathode.[6] There should also be a separator soaked with the organic electrolyte between the lithium metal and the solid electrolyte membrane, resulting in a hybrid Li-air cell, since the most commonly used lithium titanium aluminum phosphate (LTAP) electrolyte membrane is not stable on contact with lithium metal.[57]

The overall internal resistance of hybrid Li-air batteries (several hundred Ω cm^2) is high compared to that of fuel cells like direct methanol fuel cells (DMFC) and solid oxide fuel cells (SOFC) under the operating conditions due to the limited ionic conductivity of the Li-ion solid electrolyte and the unique cell structure. The high internal resistance results in limited operating current density ($\leq$ 0.5 mA cm^{-2}) and power performance of hybrid Li-air batteries. [86, 89, 114]

For hybrid Li-air batteries with acidic catholyte, platinum on carbon support is usually used as the catalyst in the air electrodes.[65, 79] Although platinum is considered as the best catalyst for the oxygen reduction reaction (ORR) in acidic solutions, the catalytic activity of platinum for the oxygen evolution reaction (OER) is quite limited.[115] This leads to a high charge voltage, which is aggravated by the high internal resistance. Both the platinum and carbon support undergo serious degradation during the high-voltage

---

* L. Li and A. Manthiram, "Hybrid lithium-air batteries: influence of catalyst, temperature, and solid-electrolyte conductivity on the efficiency and power density," *J. Mater. Chem. A*, 2013, **1**, 5121-5127.
L. Li carried out the experimental work. A. Manthiram supervised the project. Both participated in the preparation of the manuscript.

OER process, which shortens the cycle life of the air electrode.[116]

IrO_2 has been widely used in water electrolysis or photochemical water splitting due to its high catalytic activity and excellent stability.[117, 118] It has been shown not only to promote oxygen evolution but also to suppress the electrochemical carbon corrosion.[119] We showed recently that the use of IrO_2 as an OER catalyst improves the cycling performance of hybrid Li-air batteries.[69] A more detailed investigation here first of the effect of adding IrO_2 to the catalyst layer on the OER performance of hybrid Li-air batteries revealed that although adding IrO_2 to the catalyst layer lowers the charge potential and suppresses carbon support corrosion, it does not change the internal resistance, which still limits the cell performance. In order to lower the internal resistance, we explore here the effect of increasing the operating temperature of the hybrid batteries and the lithium-ion conductivity of the LTAP membrane. Both of these modifications are found to increase significantly the conversion efficiency and power density, illustrating a viable approach toward practical hybrid cells.

5.2 EXPERIMENTAL

5.2.1 Synthesis of IrO_2

IrO_2 was synthesized by a modified Adams method.[105] In a typical reaction, 142 mg of H_2IrCl_6 and 5 g of finely ground $NaNO_3$ were dissolved and well mixed in 10 mL of deionized water. The mixture was then stirred on a hot plate at 70 ºC. After the water was completely evaporated, the mixture was placed in a quartz crucible and heated to 500 ºC in air for 30 min. After cooling down, the mixture was washed with a large quantity of deionized water, centrifuged, and dried at 50 ºC to obtain IrO_2.

5.2.2 Characterization

The sample was characterized by X-ray diffraction (XRD) with a Philips X-ray diffractometer equipped with CuKα radiation from 10 to 80 º at a scan rate of 0.02 º s^{-1}. Particle size and morpholoy characterizations were carried out with a Hitachi S-5500

SEM and JEOL 2010F transmission electron microscpoe (TEM) at 200 keV. The (Brunauer-Emmett-Teller) BET surface area was measured by N_2 absorption method (NOVA 2000, Quantanchrome).

5.2.3 Three-electrode cell test

The intrinsic catalytic activity of Pt/C and IrO_2 for OER was compared with a three-electrode cell. In a typical test, a standard three-electrode cell with a electrochemical workstation (CH Instruments, Inc.) was used. A glassy carbon electrode with a diameter of 3 mm was polished to a mirror-like finish before serving as the working electrode. The counter electrode was a Pt wire. A Hg/Hg_2SO_4 electrode worked as the reference electrode and the potentials reported here are with reference to reversible hydrogen electrode (RHE). The catalyst ink (2 mg mL^{-1}) was made by sonicating 4 mg of IrO_2 powder or commercial 40 wt. % Pt on a carbon support (Johnson Matthey) in a mixture of deionized water and ethanol (2 mL, 1:1 v/v). 12 μL of the catalyst ink was then loaded onto the glassy carbon electrode followed by drying in air. 5 μL of Nafion solution (5 wt. %) was then dropped onto the top of the catalyst layer to form a protective layer.[20] The electrolyte (0.5 M H_2SO_4) was bubbled with high purity nitrogen gas for 30 min before each test. The linear sweep voltammograms (LSVs) were recorded in the range of 1.2 to 1.6 V vs. RHE at a scan rate of 5 mV s^{-1}. Similarily, LSVs for ORR of Pt was measured on a rotating disk electrode (5 mm diameter, 1600 rpm) in the range of 1.05 to 0.15 V vs. RHE at a scan rate of 5 mV s^{-1}.[120] Temperature was controled by a circulating waterbath (Fisher Scientific).

5.2.4 Half cell test

The cycling performance of the air electrodes was tested in a home-made three-electrode half-cell in which 0.5 M H_2SO_4, a Hg/Hg_2SO_4 electrode, and a platinum flag were used, respectively, as the electrolyte, reference electrode, and counter electrode. The method to prepare the air electrode has been reported elsewhere.[65] The potentials are also referred to RHE.

5.2.5 Full cell test

A home-made PTFE layered battery mould was used to carry out the full cell test.[65] For heating purposes, the anode and cathode plates were made of stainless steel. The anode side was assembled in an argon-filled glove box and then combined with the cathode side in air. The anode side consisted of a nickel foam current collector, a lithium-metal foil, and the organic carbonate electrolyte (1 M $LiPF_6$ in ethylene carbonate (EC) / diethylcarbonate (DEC) (1:1 v/v)). The cathode side consisted of 1 mL of 0.1 M H_3PO_4 + 1 M LiH_2PO_4 buffer solution as the catholyte, an air electrode (0.76 × 0.76 cm) containing 1.2 mg cm^{-2} Pt plus various mass loading of IrO_2 as the catalyst, and a platinum mesh current collector. A LTAP membrane (0.15 mm thick, $\sigma = 1\times10^{-4}$ S cm^{-1} or 2.5×10^{-4} S cm^{-1}, 0.76 × 0.76 cm, OHARA Inc., Japan) was used as the separator. The cathode side of the hybrid cell was purged with water-saturated air during operation to suppress the evaporation of water from the catholyte.[69]

The internal resistance was measured at open circuit voltage (OCV) by a Solartron 1260A impedance analyzer from 2 MHz to 0.01 Hz with an ac voltage amplitude of 10 mV. Discharge-charge experiments were conducted on an Arbin BT 2000 battery cycler. Polarization curves were recorded on a VoltaLab PGZ 402 potentiostat by sweeping the potential from OCV to 1 V vs. Li^+/Li.

5.3 RESULT AND DISCUSSION

5.3.1 Effect of IrO_2

The indexed XRD pattern shown in Figure 5.1a confirms the formation of pure rutile-type IrO_2. The broad peaks indicate a small particle size and low crystallization, which is beneficial for good electrocatalytic activity.[121] The BET surface area was measured to be 130.73 m^2/g. Figure 5.1b shows the SEM image of the synthesized IrO_2 in which it is difficult to determine the particle size due to agglomeration of the nanosize particles. However, from the low and high magnification TEM images in Figure 5.1c and d, nancrystalline IrO_2 with an average particle size of several nanometers can be clearly

observed.

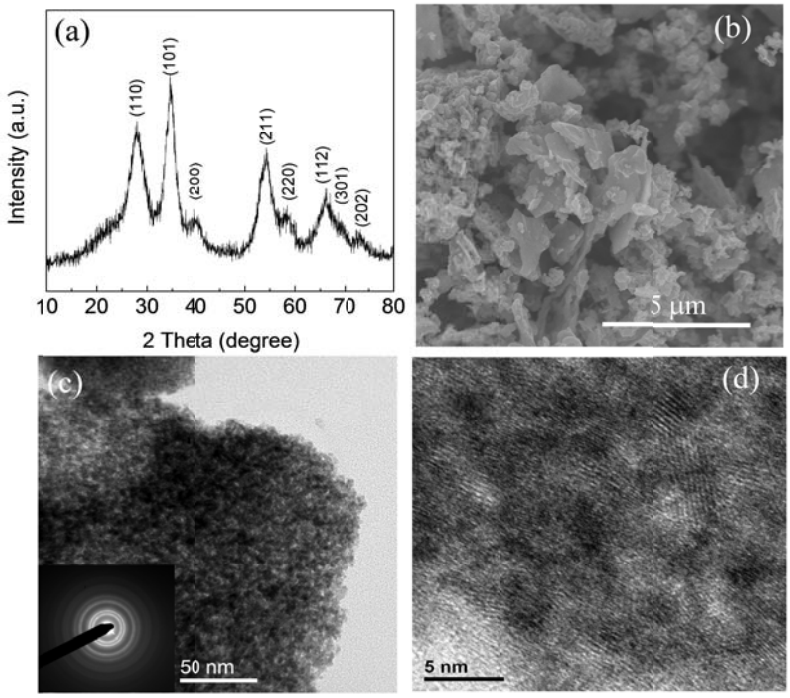

Figure 5.1. (a) XRD pattern, (b) SEM image, (c) Low magnification and (d) High-magnification TEM images of the synthesized IrO_2.

The intrinsic catalytic activity of the synthesized IrO_2 towards OER was first evaluated by linear sweep voltammograms (LSVs) on a glassy carbon electrode. For a comparison, the LSVs of Pt/C were also evaluated as shown in Figure 5.2a. The calculated standard electrode potential for OER in 0.5 M H_2SO_4 is 1.23 V vs. RHE at 25 °C. The clear onset potential around 1.5 V vs. RHE and the rapid increasing current density at higher voltage indicate the much better catalytic activity of IrO_2 over Pt/C for the OER. To evaluate the effect of IrO_2 on the performance of air electrodes, the air electrodes containing 1.2 mg/cm^2 Pt/C or 1.2 mg/cm^2 Pt/C + 1.2 mg/cm^2 IrO_2 catalyst were prepared and tested in half-cells. Figure 5.2b shows the first ten cycles of the two air electrodes at a current density of 1 mA/cm^2. The charging potential of the Pt/C air

electrode is almost 0.1 V higher than that of the Pt/C + IrO_2 air electrode and it keeps increasing slowly, while the charging potential of Pt/C + IrO_2 air electrode stays steady throughout the ten cycles. The discharge potential of Pt/C + IrO_2 air electrode is initially lower than that of the Pt/C air electrode, which can be attributed to the lower conductivity of IrO_2, thicker catalyst layer, and higher Nafion loading. But the discharge voltage of the Pt/C + IrO_2 air electrode becomes comparable to or higher than that of the Pt/C air electrode after five cycles, showing that IrO_2 improves the long-term cycling performance of the air electrodes. Figure 5.2c shows the polarization curves toward OER of the Pt/C + IrO_2 air electrodes with different IrO_2 mass loading in the catalyst layer in Li-air cells. The curvature of the OER polarization curve becomes smaller as we increase the catalyst loading from 0 to 0.8 mg/cm^2. If the IrO_2 loading is 1.2 mg/cm^2 or more, the OER polarization curve becomes a straight line, revealing that the support-carbon corrosion has been so greatly suppressed that it does not influence the shape of the polarization curves. The linear curve could be fitted with the formula,

$$U=E-I\times R \quad (1)$$

where E is the electromotive force, I is the current (negative here because of a charging current), and R is the overall internal resistance. In contrast, the polarization curve of the IrO_2-poor (< 1.2 mg/cm^2) air electrodes is bent at higher current densities above 4.6 V vs. Li^+/Li (*i.e.*, 1.6 V vs. NHE). This abnormal increase in current could be explained by the apparent corrosion on the carbon support above 1.6 V vs. NHE, which has been proved by CO_2 mass spectra.[119] Figure 5.2d shows the charge voltage profiles of the Li-air cells with and without the IrO_2 catalyst at different current densities from 0.5 to 2.0 mA cm^{-2}. The reversible electrode reactions and the overall cell reaction have been reported elsewhere.[65] The calculated OCV for the total reaction is about 4.08 V at 25 °C, taking the oxygen partial pressure to be 0.2 atm. The charge voltage of the Pt/C +IrO_2 air electrode is lower than that of the Pt/C air electrode at each current density, illustrating lower overpotential, which can improve the battery efficiency. The charge voltage at 2 mA cm^{-2} is decreased by 0.11 V with the addition of IrO_2 to the air electrode. In the case

of regenerative fuel cells, a large decrease of about 300 mV in the terminal voltage has been reported with the addition of a small amount of IrO_2 to the air electrode during water electrolysis.[121] Oxygen evolution reaction could predominantly take place on the IrO_2 surface due to its higher catalytic acitivity, and the produced oxygen gas eliminates water on the carbon surface to suppress carbon support corrosion,[113] which can improve the service life of the air electrodes as well as the performance of the cell.

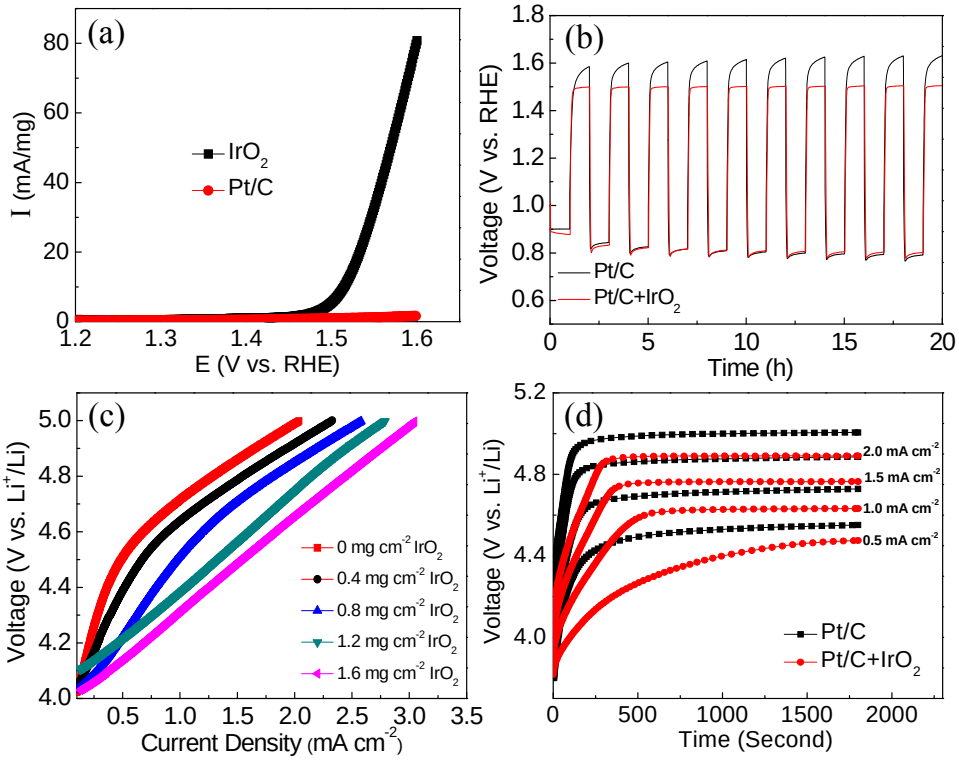

Figure 5.2. (a) Linear sweep voltammograms of Pt/C and IrO_2, (b) cycling performance of 1.2 mg/cm^2 Pt/C or 1.2 mg/cm^2 Pt/C +1.2 mg/cm^2 IrO_2 air electrodes at 1 mA/cm^2 in half cell, (c) polarizations curves of Pt/C + IrO_2 air electrodes with different IrO_2 mass loading in Li-air cells, and (d) charge voltage profiles of Pt/C and Pt/C + IrO_2 air electrodes in Li-air cells.

5.3.2 Effect of temperature

Increasing the temperature has been found to reduce the overall internal resistance of hybrid Li-air fuel cells with an alkaline catholyte.[83] However, the effect of temperature on the charging process of hybrid Li-air cells has not been reported yet. Here, we show how the high operating temperature affects the internal resistance and charge/discharge behavior of the hybrid Li-air cells. As shown in Figure 5.3a, when the operating temperature is increased from 20 to 40 ºC, the overall internal resistance is reduced by nearly 50 %. The impedance data are fitted with the Zview software with the equivalent circuit shown in the figure.[83] The largest reduction, as seen in Figure 5.3a, lies in the two semicircles, which are believed to be the grain boundary resistance and interfacial plus charge transfer resistance. The ionic conductivity in the liquid and solid electrolyte is enhanced at elevated temperatures. The charge transfer resistance also decreases as the temperature increases because of the higher catalytic activity of the catalyst at higher temperatures.[83] Figure 5.3b shows the polarization curves toward ORR of the Li-air cell at different temperatures. These curves were obtained by using a potential sweep method at a scan rate of 10 mV s^{-1}. The polarization is mainly governed by the internal resistance and catalytic activity towards ORR, which is quite similar to that in fuel cells.[122] As the temperature increases, the slope of the curves in high current density decreases because of the decreasing internal resistance, and a large slope in the region of low current density (< 4 mA cm^{-2}) shortens due to the improved catalytic activity. The maximum power density increases nearly three-fold from ~ 12 mW cm^{-2} to ~ 30 mW cm^{-2} when the operating temperature is increased from 20 to 40 ºC. It has been suggested to put an additional capacitor electrode facing the lithium-metal anode in organic electrolytes to improve the power performance by almost ten times.[100] Here, we show a facile way to improve the performance of hybrid lithium-air cells by increasing the operating temperature.

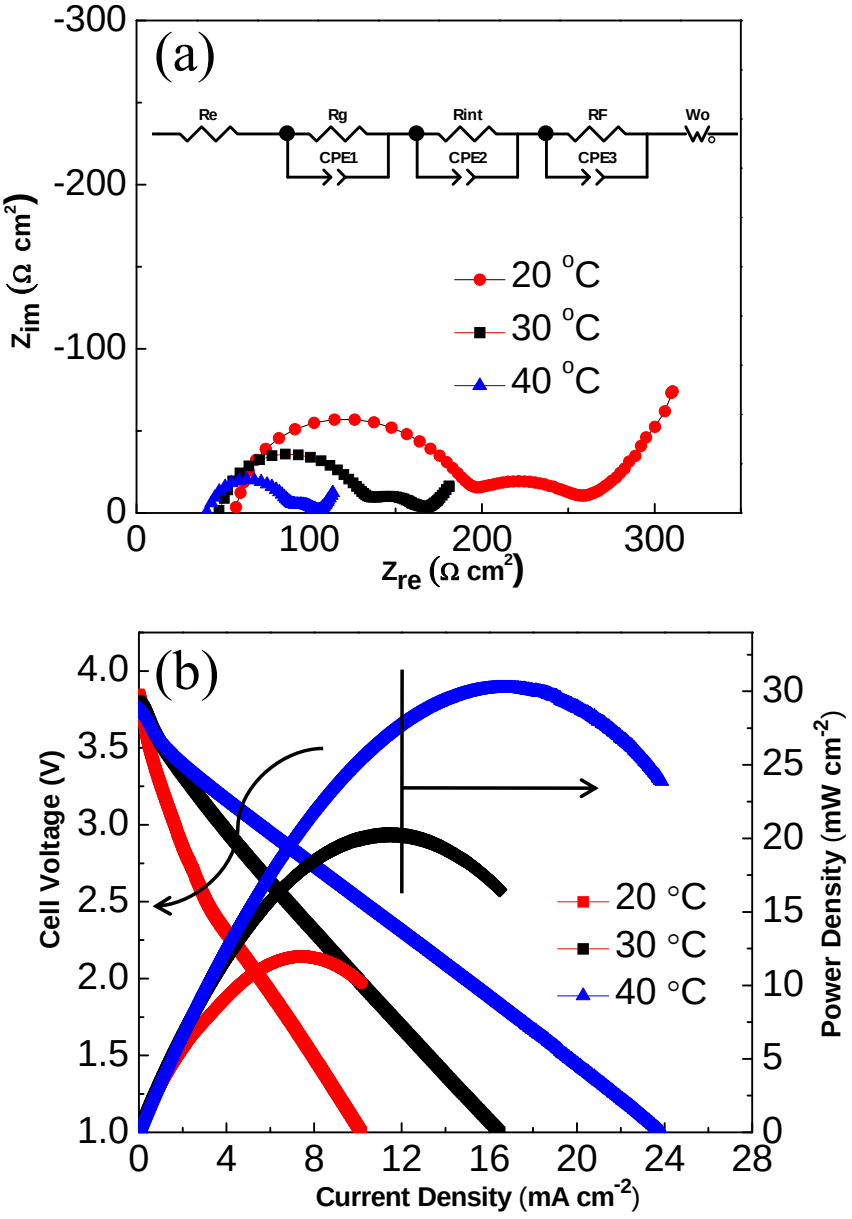

Figure 5.3. Effect of temperature on the (a) overall internal resistance and (b) power performance of Li-air cells.

In order to illustrate how temperature affects the intrinsic catalytical activity of the catalyst without influence from the internal resistance, LSVs of Pt/C towared the ORR and IrO_2 toward the OER were recorded at 20 and 40 °C. Based on the LSVs for the ORR of Pt/C in Figure 5.4a, the diffusion-limited current densities are slightly higher at 40 °C. Based on the calculations reported elsewhere, the diffusion limited current densities of Pt should remain nearly constant from 20 to 60 °C, with a local maximum at 55 °C.[123] Above 60 °C, the diffusion-limited current density is predicted to decrease due to the increase in the vapor pressure of water. In our experiements, the cell is just heated up to 40 °C, which slightly improves the ORR activity of Pt in the catalyst layer. For the OER of IrO_2 in Figure 5.4b, the onset potential is lower and the current densities are apparently higher at 40 °C, indicating the much improved OER performance of IrO_2 at elevated temperatures.

To examine further the effect of temperature on the discharge and charge overpotentials of the Li-air cell, the discharge and charge voltage profiles at different current densities at 20 and 40 ºC are presented in Figure 5.5. The catalyst used was 1.2 mg cm^{-2} Pt + 1.2 mg cm^{-2} IrO_2. At both temperatures, the charge potentials increase and the discharge potentials decrease with increasing current densities, resulting in desending conversion efficiency. However, the overpotentials at 20 ºC increase much faster than those at 40 ºC due to the high overall internal resistance at 20 ºC (almost twice as big as that at 40 ºC). The battery conversion efficiency at the current density of 2.0 mA cm^{-2} based on the terminal voltage increases from ~ 61 % at 20 ºC to ~ 74 % at 40 ºC.

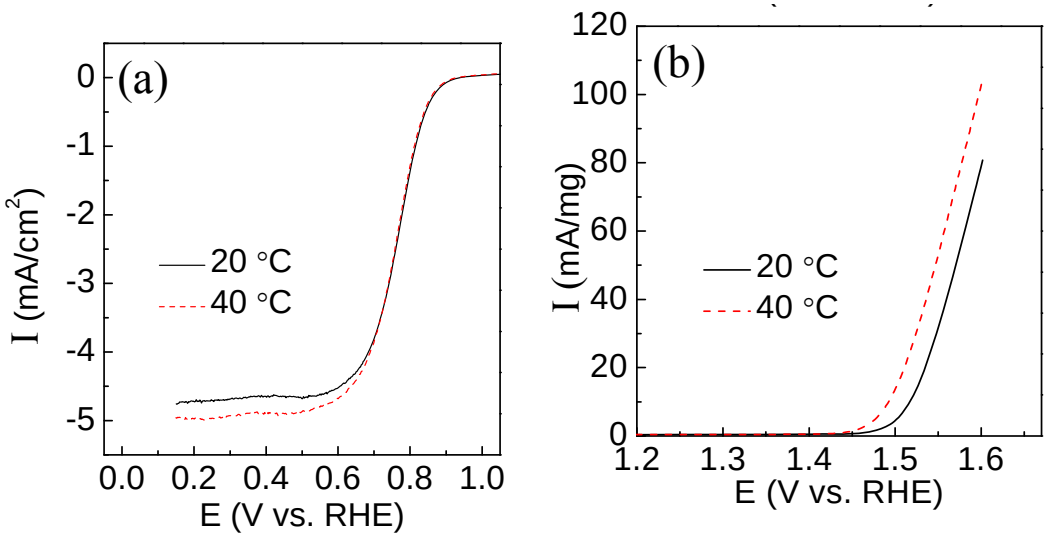

Figure 5.4. LSVs for (a) ORR of Pt/C (1600 rpm) in oxygen saturated and (b) OER of IrO_2 in nitrogen saturated 0.5 M H_2SO_4 solution at 20 and 40 °C.

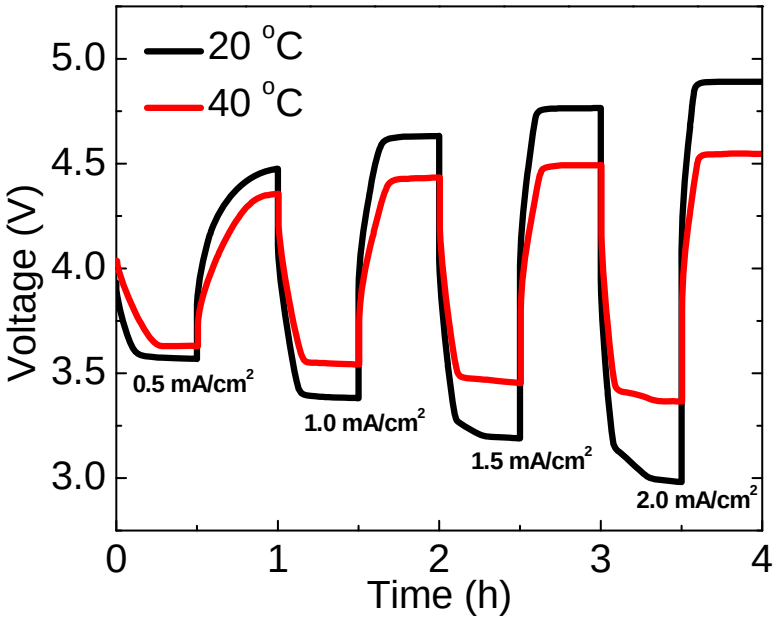

Figure 5.5. Effect of temperature on the discharge and charge voltage profiles of Li-air cells at different current densities.

5.3.3 Effect of solid-electrolyte conductivity

In our Li-air cells, we use a NASICON-type Li^+-ion solid electrolyte ($Li_{1+x+y}Al_xTi_{2-x}Si_yP_{3-y}O_{12}$ or LTAP, OHARA Inc., Japan), which has a high plate ionic conductivity of ~ 1×10^{-4} S cm^{-1} at room temperature. Since the solid electrolyte takes up a large portion of the overall internal resistance of the hybrid Li-air cell, we would naturally expect a significant reduction of the overall internal resistance by using a LTAP with a higher ionic conductivity. In the literature, LTAP membranes with different ionic conductivities are used by different groups. However, the dependence of the cell performance on the LTAP membranes with various ionic conductivities has not been studied yet.

Herein, we report the cell performance with two types of LTAP membranes, which have same thickness (150 μm) but different ionic conductivities (1×10^{-4} S cm^{-1} vs. 2.5×10^{-4} S cm^{-1} at room temperature). The overall resistance of the solid electrolyte is given as

$$R = L/\sigma\times A \qquad (2)$$

where R is the total resistance of the LTAP membrane, L is the thickness, σ is the ionic conductivity, and A is the area. The total resistance of the LTAP membrane with the conductivity of 1×10^{-4} S cm^{-1} at room temperature in the cell is calculated to be 150 Ω cm^2. After increasing the ionic conductivity from 1×10^{-4} S cm^{-1} to 2.5×10^{-4} S cm^{-1}, the total internal resistance associated with the solid electrolyte at room temperature is calculated to be 90 Ω cm^2. As can be seen in Figure 5.6a, a considerable reduction in internal resistance compared to that we obtained in Figure 5.4a at the same temperatures is achieved. The total internal resistance also decreases with increasing temperature, consistent with what we observed in the previous section. The overall internal resistance decreases to less than 100 Ω cm^2 with the LTAP membrane having an ionic conductivity of 2.5×10^{-4} S cm^{-1} at the elevated operating temperatures.

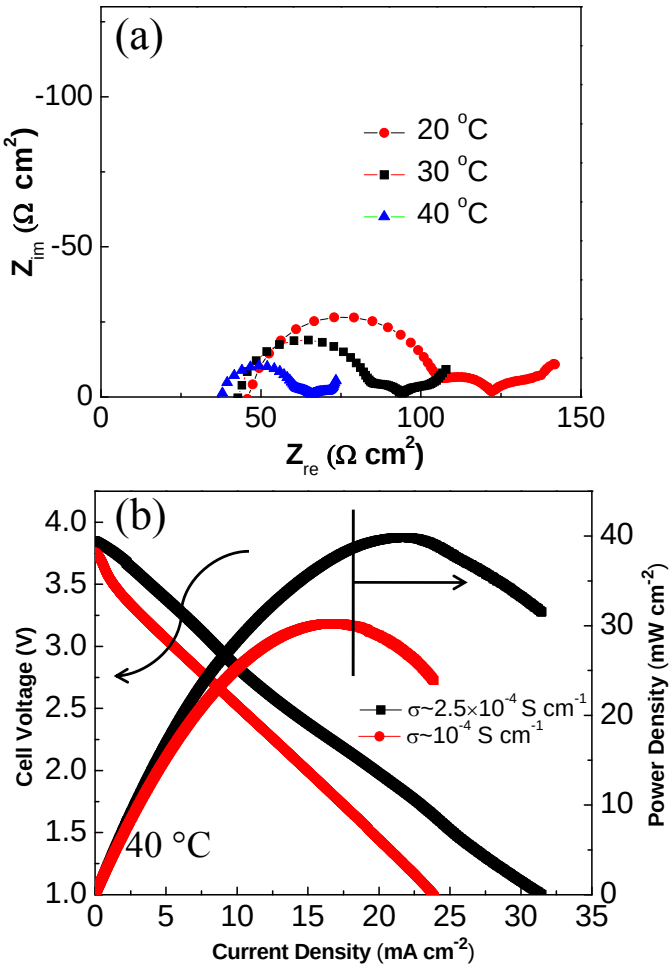

Figure 5.6. (a) Effect of temperature on the internal resistance of Li-air cells with a better LTAP ($\sigma \sim 2.5\times10^{-4}$ S cm^{-1}) and (b) the effect of ionic conductivity of LTAP on the power performance of Li-air cells.

The polarization curves of the cells with different LTAP membranes are plotted in the voltage range of OCV to 1.0 V vs. Li^+/Li at 40 ºC in Figure 5.6b. Both curves are almost linear under the control of internal resistance. As the ionic conductivity increases, the slope decreases. The maximum power density increases from ~ 30 mW cm^{-2} to ~40 mW cm^{-2} by increasing the ionic conductivity of the LTAP membrane. Discharge-charge

voltage profiles of the cells with the two LTAP membranes at 40 ºC are shown in Figure 5.7. The efficiency at 2 mA cm^{-2} is improved from 74 % to 80 % after increasing the ionic conductivity of the LTAP membrane. To the best of our knowledge, a discharge voltage plateau above 3.5 V and a charge voltage plateau below 4.5 V at 2 mA cm^{-2} are among the best reported performance for hybrid Li-air batteries.

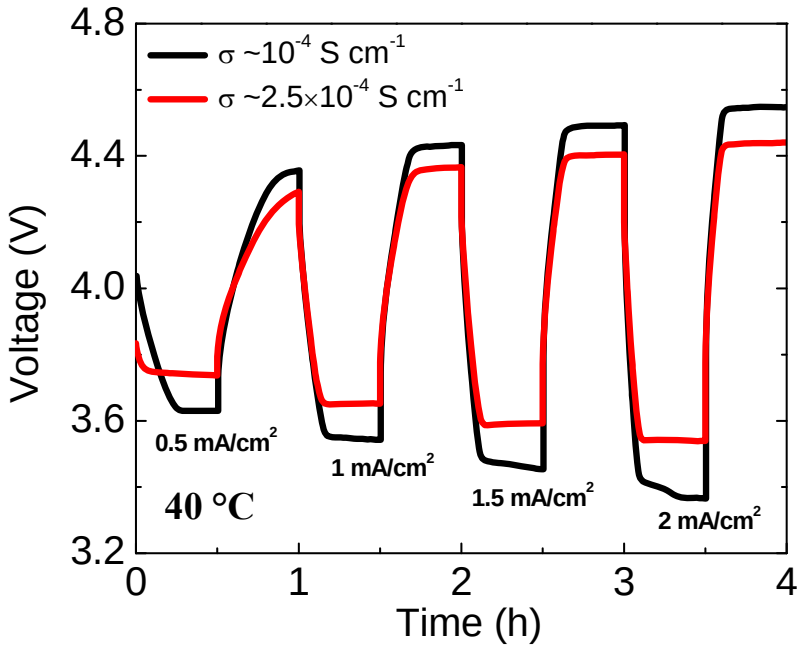

Figure 5.7. Effect of temperature on the discharge and charge voltage profiles of Li-air cells at different current densities.

Further improvements on the cell performance call for a solid electrolyte that is stable on contact with lithium, eliminating the use of organic solvent, and has a high ionic conductivity (> 1×10^{-3} S cm^{-1}). Weppner *et al.*[46] have reported a stable lithium garnet on contact with lithium metal and a room-temperature ionic conductivity > 10^{-4} S cm^{-1}, which is very attractive as a potential solid electrolyte for hybrid Li-air batteries. Recently, an optimum ionic conductivity of ~ 1×10^{-3} S cm^{-1} of lithium garnet $Li_{7-x}La_3Zr_{2-x}Ta_xO_{12}$ ($0 \leq x \leq 0.6$) has been achieved by Goodenough's group.[50] Although some

problems still exist with these solid electrolytes, these promising results suggest that there is still much room to improve the performance of hybrid Li-air batteries.

5.4 CONCLUSION

Lack of efficient oxygen evolution catalysts and large internal resistance have been identified as two major problems facing hybrid Li-air batteries. We have shown that the use of IrO_2 as the oxygen evolution catalyst in hybrid Li-air batteries lowers the charge potential, leading to increased battery conversion efficiency. Also, the carbon support corrosion has been suppressed, improving the durability of the air electrode. The large internal resistance has been decreased by elevating the operating temperature or increasing the ionic conductivity of the LTAP membrane. With these optimizations, the maximum power density reaches 40 mW cm^{-2} and the battery conversion efficiency at 2 mA cm^{-2} reaches 80 % at 40 ºC. Overall, this study points out ways to improve the performance of hybrid Li-air batteries toward potential applications such as large-scale grid energy storage.

Chapter 6: O- and N-doped carbon nanoweb as metal-free catalysts for hybrid Li-air batteries*

6.1 INTRODUCTION

The oxygen reduction reaction (ORR) at the cathode of hybrid Li-air batteries is sluggish, which usually requires noble-metal catalysts like Pt or its alloys to retain a high discharge voltage.[67, 69, 80] The high cost and scarcity of Pt will impede the wide application of hybrid Li-air batteries.[37, 124] The practical catalysts for hybrid Li-air batteries should ideally be based on environmentally abundant elements that could facilitate high catalytic activity.

N-doped carbon materials have been proposed as an effective ORR catalyst. The diversity in carbon structure and morphology enables the possibility to optimize oxygen/electrolyte diffusion and electron transport. In addition, considerable improvement in ORR activity has been shown with carbon materials by nitrogen doping. For example, nitrogen doping has been reported to enhance greatly the ORR activity of carbon nanotubes (CNT) and graphene.[125, 126] Nitrogen-doped carbon nanotube cups have been found to exhibit catalytic activity similar to Pt-CNTs.[127] The ORR activity of nitrogen-doped carbon nanofibers was much higher than that of undoped carbon nanofibers, possibly due to faster hydrogen peroxide decomposition by nitrogen doping.[128] Nitrogen-doped carbon nanosheets with size-defined mesopores showed pronounced electrocatalytic activity and long-term stability toward ORR under acidic conditions.[129] A special kind of CNTs with strongly attached graphene wings that were doped with nitrogen showed high activity for catalyzing ORR in an alkaline electrolyte.[130] Other special nitrogen-doped carbons investigated include fullerenes, quantum dots, nanoribbons, nanocapsules, *etc*.[131-134] But most studied carbon materials

---

* L. Li and A. Manthiram, "O- and N-doped carbon nanoweb as metal-free catalysts for hybrid Li-air batteries," *Adv. Energy Mater.*, DOI: 10.1002/aenm.201301795 (2014).
L. Li carried out the experimental work. A. Manthiram supervised the project. Both participated in the preparation of the manuscript.

are 1-D or 2-D materials with limited oxygen and electrolyte diffusion properties, like carbon nanotubes, carbon nanofibers, and graphene. Although some 3-D structures, like aligned N-doped carbon nanotube arrays and 3-D graphene-based hybrid materials, can be achieved by carefully tuning the synthesis process, these processes are inevitably complex and could impede the large scale production of these materials.[135-137]

We present here a facile synthesis of a novel 3-D O- and N-doped carbon nanoweb (ON-CNW) as a potential metal-free catalyst for ORR in hybrid Li-air cells. The 3-D nanoweb structure provides an ideal backbone support for catalytically active sites due to the fast electron and mass transport properties compared with the 1-D or 2-D structure. In addition, the synergistic effect between the O and N groups creates highly active pyridone groups all over the nanoweb surface, which significantly improves the catalytic activity toward ORR. With a hybrid Li-air cell, the ON-CNW is shown to exhibit superior cell performance close to that of commercial Pt/C catalyst.

6.2 EXPERIMENTAL

6.2.1 Chemicals and materials

Cetrimonium bromide ($C_{19}H_{42}BrN$, 99+ %, Acros Organics), hydrochloric acid (HCl, 37 %, Fisher Scientific), ammonium peroxydifulfate ($(NH_4)_2S_2O_8$, 99.5 %, Fisher Scientific), pyrrole (C_4H_5N, 99 %, Acros Organics), potassium hydroxide (KOH, 85.3 %, Fisher Scientific), lithium hydroxide monohydrate ($LiOH{\cdot}H_2O$, Fisher Scientific), and lithium nitrate ($LiNO_3$, 99 %, Acros Organics), were purchased and used as received.

6.2.2 Synthesis

The polypyrrole (PPy) nanoweb was synthesized by an oxidative template assembly method.[138, 139] In a typical synthesis, cetrimonium bromide (CTAB, 0.6 mmol) was dissolved in 1 M HCl (60 mL) under ice bath. Meanwhile, ammonium peroxydifulfate (18 mmol) was dissolved in de-ionized water (10 mL) and added into the above solution. The solution was stirred for 0.5 h before pyrrole (200 μL) was added. The

reaction was kept under ice bath for 4 h with continuous stirring. Then the black precipitate was suction filtered, washed with 1 M HCl (300 mL) and de-ionized water (2 L), and oven dried at 50 °C overnight. The PPy nanosphere was synthesized by the same process without adding the CTAB surfactant. N-CNW and N-CNS were obtained by annealing the PPy nanoweb or nanosphere precursors in a N_2 atmosphere at 900 °C for 3 h with a heating and cooling rate of 2 °C min^{-1}. ON-CNW was obtained by activating N-CNW with KOH powder in a mass ratio of 1 : 2 in a N_2 atmosphere at 600 °C for 0.5 h, followed by washing and drying.

6.2.3 Characterization

Morphology characterizations were carried out with a Hitachi S-5500 SEM and JEOL 2010F transmission electron microscpoe (TEM) at 200 keV. The Brunauer–Emmett–Teller (BET) surface areas were measured by the N_2 absorption method (NOVA 2000, Quantanchrome). X-ray diffraction (XRD) data were collected with a Philips X-ray diffractometer equipped with CuKα radiation from 10 to 90 º at a scan rate of 0.02º s^{-1}. X-ray photoelectron spectroscopy (XPS) data were collected with a Kratos Analytical spectrometer.

6.2.4 Electrohemical characterization

The intrinsic catalytic activities of N-CNS, N-CNW, and ON-CNW were compared by linear sweep voltammetry (LSV) and cyclic voltammetry (CV) in a standard rotating disk electrode (RDE) setup with an Autolab PGSTAT302N potentiostat (Eco Chemie B.V.). The catalyst ink (5 mg mL^{-1}) was made by sonicating N-CNS, N-CNW, or ON-CNW powder (10 mg) in ethanol (2 mL). The catalyst ink (5 μL) was then loaded onto the glassy carbon electrode (5 mm diameter) followed by drying in air. 5 μL of Nafion solution (0.5 wt. %) was then dropped onto the top of the catalyst layer to form a protective layer. CVs and LSVs were obtained by sweeping the potential between -1.0 to 0.0 V (vs. SCE) at a scan rate of 10 and 30 mV s^{-1}, repectively. The half-cell test was

conducted in a three-electrode half-cell with 0.5 M LiOH + 1 M $LiNO_3$ as the electrolyte.[140] Polarization curves were recorded on a VoltaLab PGZ 402 potentiostat by sweeping the potential at a scan rate of 10 mV s^{-1}. Chronopotentiometry (i~t) data were collected on an Arbin BT 2000 battery cycler. The polarization curves and chronopotentiometry (i~t) data were manually corrected for iR loss. The air electrodes were prepared by spraying the catalyst ink made with the N-CNS, N-CNW, or ON-CNW catalyst and LITHion binder (Ion Power, USA) onto a 10 BA gas diffusion layer (GDL). The catalyst loading and binder content in the air electrodes were 1 mg cm^{-2} and 20 wt. %. A PTFE layered battery mold was used to carry out the full cell test with 0.5 M LiOH + 1 M $LiNO_3$ (2 mL) as the catholyte.[65] The anode and cathode were separated by a $Li_{1+x+y}Ti_{2-x}Al_xP_{3-y}Si_yO_{12}$ (0.15 mm thick, $\sigma = 1 \times 10^{-4}$ S cm^{-1}, 0.76 × 0.76 cm, OHARA Inc., Japan) solid Li-ion conducting electrolyte. Discharge-charge experiments were conducted on an Arbin BT 2000 battery cycler. The obtained specific capacity was calculated based on the total mass of catalyst in the ORR and OER electrodes (1 mg cm^{-2} + 1 mg cm^{-2}).

6.3 RESULT AND DISCUSSION

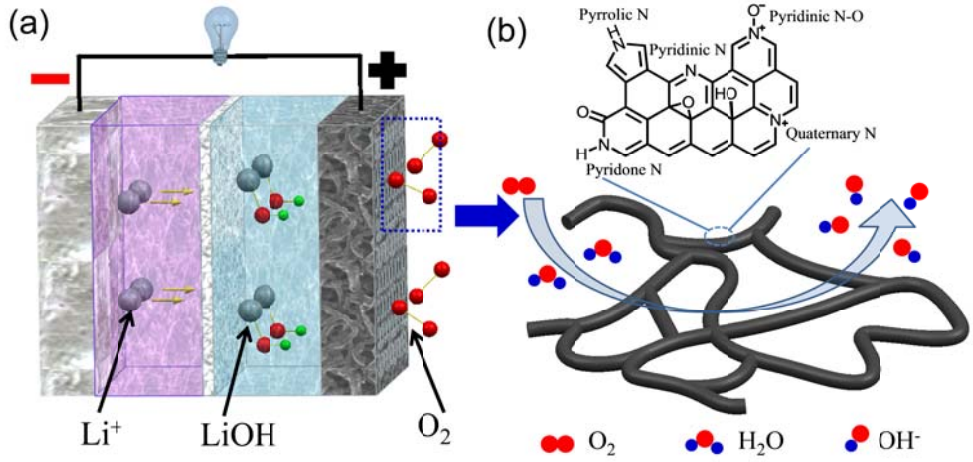

Figure 6.1. (a) Schematic illustration of the hybrid Li-air battery with metal-free ON-CNW as the ORR catalyst and (b) ORR on the surface of ON-CNW.

Figure 6.1(a) shows the discharge mechanism of a hybrid Li-air cell based on an alkaline catholyte and ON-CNW catalyst. Upon discharge, oxygen from air is absorbed and reduced on the catholyte / ON-CNW / Air three-phase interface, which then combines with the water in the catholyte and the Li^+ ions diffusing from the anode through the solid electrolyte into the catholyte to form the discharge product LiOH. The detailed ORR process on the ON-CNW surface is depicted in Figure 6.1b. Polypyrrole is made of five-membered pyrrole rings, which are mostly converted into six-membered rings during pyrolysis at high temperatures. The six-membered rings mainly consist of pyridinic and quartenary nitrogen functionalities, which are the most stable forms under the high-temperature pyrolysis condition.[141] These N groups have certain ORR catalytic activity. But recently, the pyridone groups have been identified as more active catalytic sites for ORR, which can be formed by grafting O groups near the N groups. KOH activation, which is a traditional method to increase the surface area of carbon, introduces a large amount of oxygen-containing functional groups (*e.g.*, carbonyl, epoxide, hydroxyl) on the web surface (Figure 6.1b). After the activation process, the synergistic effect between the O and N groups creates lots of pyridone groups in ON-CNW and greatly enhances its ORR catalytic activity.[142]

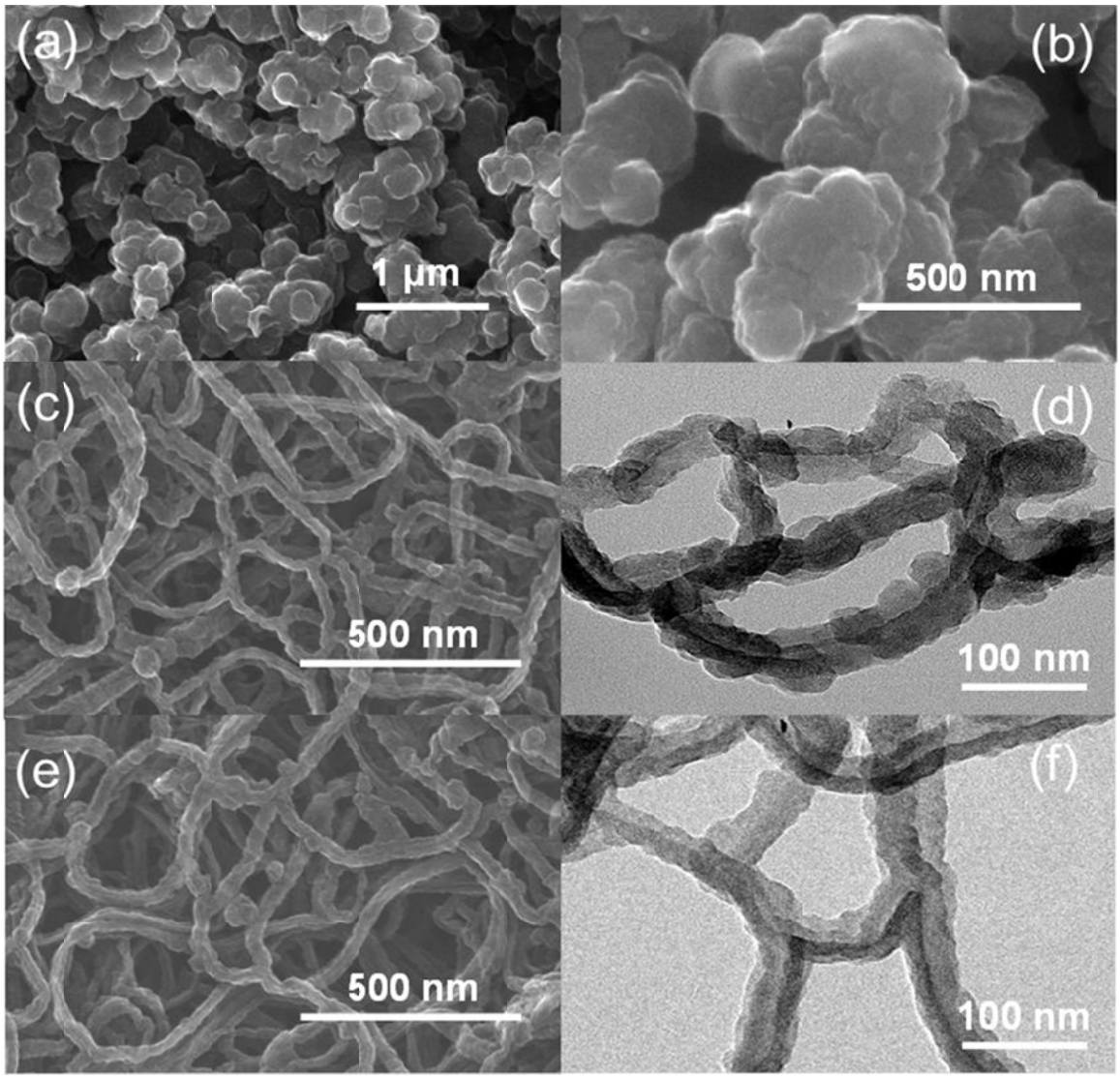

Figure 6.2. SEM and TEM images of (a, b) N-CNS, (c,d) N-CNW, and (e, f) ON-CNW.

Figure 6.2 compares the scanning electron microscopy (SEM) and transmission electron microscopy (TEM) images of the synthesized N-doped carbon nanospheres (N-CNS), N-doped carbon nanoweb (N-CNW), and ON-CNW. N-CNS and N-CNW were obtained by annealing their polypyrrole (PPy) precursors (Figure 6.3) in a N_2 atmosphere at 900 °C. ON-CNW was obtained by activating the N-CNW with KOH in an inert

atmosphere. KOH can consume, broaden, and even collapse the (002) planes of graphite during the activation process.[143] N-CNW can lose the web morphology if excess KOH is used. Accordingly, the maximum mass ratio of KOH to N-CNW was determined to be 2:1.

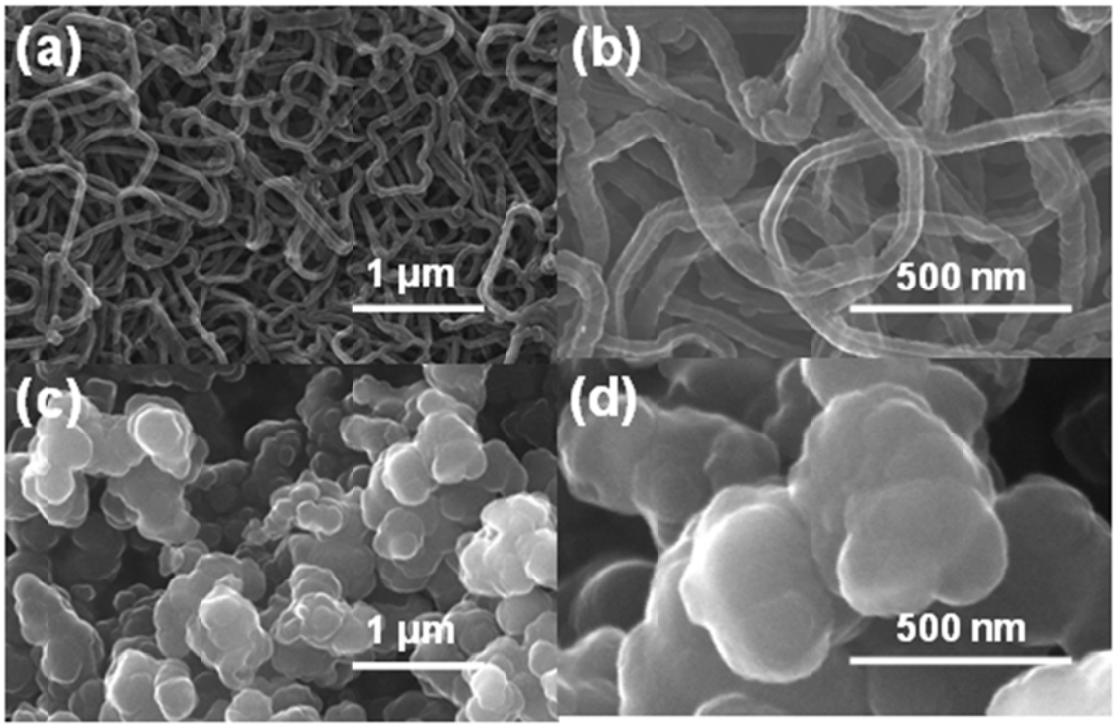

Figure 6.3. SEM images of the synthesized PPy nanoweb and nanosphere precursor.

The hetero-atom doping compositions were determined by XPS. Figure 6.4a and b show the N 1s and O 1s spectra of N-CNW, while Figure 6.4c and d show those of ON-CNW. The oxygen content in ON-CNW is increased nearly by five times after the KOH activation, as shown in Figure 6.4b and d and quantified in Table 6.1, indicating that a lot of O groups have been grafted onto the carbon surface. The deconvolution of the N 1s peak of N-CNW and ON-CNW (Figure 6.4a and c) shows, after the KOH activation, a significant increase in the content of N-5 nitrogen (pyridone/pyrrolic nitrogen) with a corresponding reduction in the content of N-6 nitrogen species (Table 6.2),[141] which is

inconsistent with the fact that N-6 nitrogen species are more stable than the N-5 pyrrolic nitrogen at high temperatures.

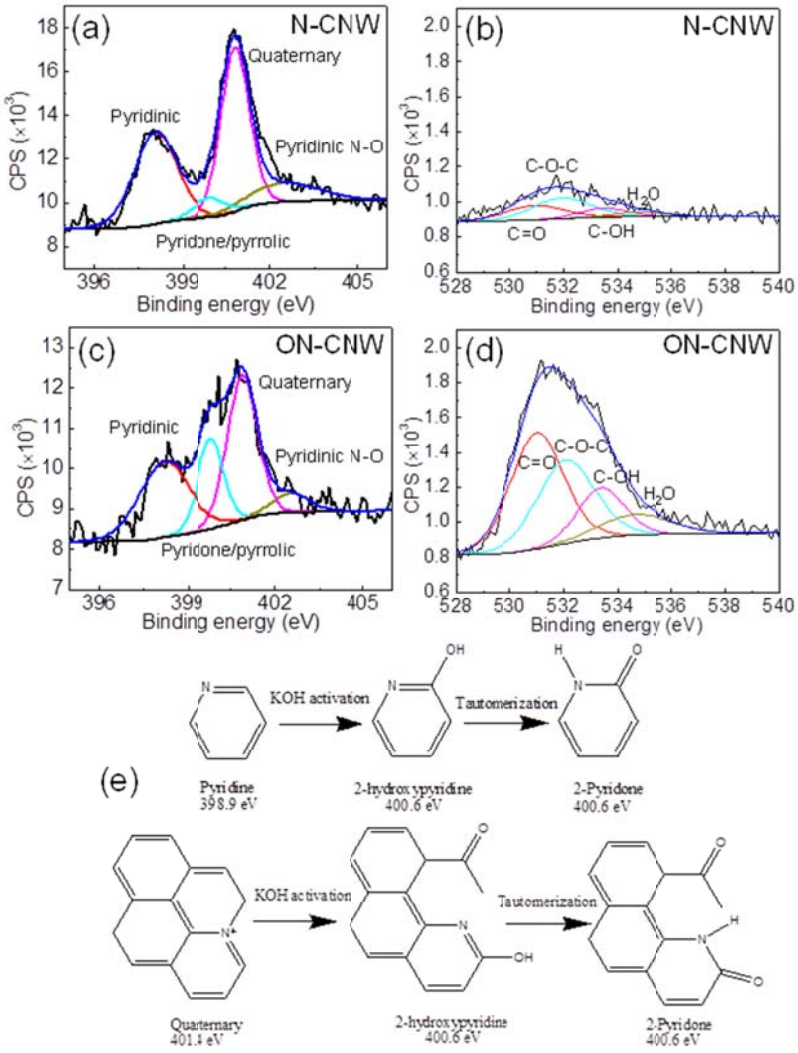

Figure 6.4. XPS analysis of the N 1s and O 1s peak of (a, b) N-CNW and (c, d) ON-CNW. (e) Transformation of N-6 (pyridine and quarternary nitrogen) into N-5 (2-pyridone) through KOH activation and tautomerization.

Sample	Wt. % C	Wt. % N	Wt. % O
N-CNS	88.96	6.71	4.33
N-CNW	89.23	8.70	2.07
ON-CNW	84.48	4.72	10.80

Table 6.1. Compositional analysis based on the peaks in the XPS spectra.

Sample	Pyridinic atom %	Pyridone/Pyrrolic atom %	Quarternary atom %	Pyridinic N-O atom %
N-CNS	28.72	9.62	44.5	17.16
N-CNW	36.3	7.05	45.11	11.54
ON-CNW	32.16	20.14	36.87	10.83

Table 6.2. N1s compositional analysis from XPS spectra.

It is believed that the increase in N-5 nitrogen comes from pyridone instead of pyrrole.[142] Pyridone can undergo tautomerization with hydroxypyridine; in other words, the pyridinic nitrogen can be grafted with a hydrogen from the nearby hydroxyl group (Figure 6.4e). The introduced hydroxyl groups come from KOH at 600 °C. Quaternary nitrogen can also undergo a similar transformation once a hydroxyl group is introduced onto the nearby carbon (Table 6.2, Figure 6.4e). Thus, the content of N-5 nitrogen (pyridone/pyrrolic) on ON-CNW sample is about three times that of N-CNW. Correspondingly, a significant increase in the carbonyl functional groups (from pyridone) in ON-CNW is expected, which is confirmed by the strong carbonyl O 1s peak in Figure 6.4d. The pyridone nitrogen is known to stabilize singlet dioxygen by forming a stable adduct (Figure 6.5).[141, 144] This helps weakening and breaking the bond in the oxygen molecule, which is a critical step for ORR. Thus, an improved ORR catalytic activity is expected for N-CNW after the KOH activation.

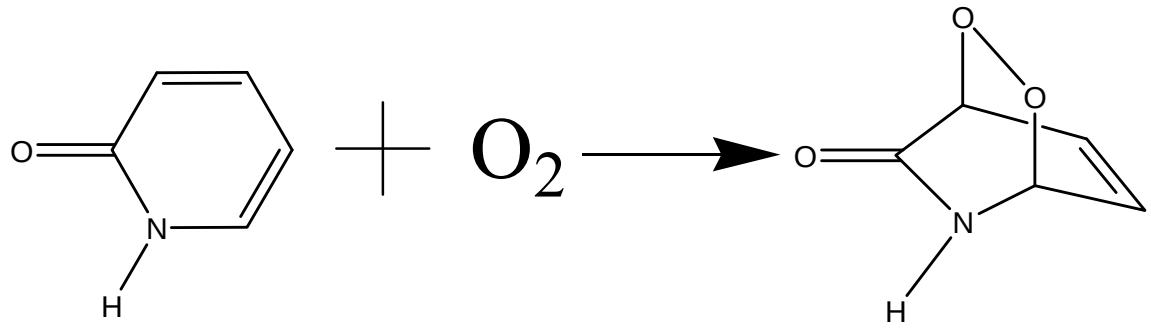

Figure 6.5. The combination of pyridone and singlet oxygen to form a stable adduct.

The three samples (N-CNS, N-CNW, and ON-CNW) were characterized by cyclic voltammetry (CV) in O_2 or N_2 saturated 0.1 M KOH shown in Figure 6.6a. These voltammograms possess a single ORR peak only in the O_2 saturated 0.1 M KOH. The ORR peak potential for N-CNS is -0.4 V (vs. SCE). But for the N-CNW, the peak potentials are positively shifted to -0.29 V (vs. SCE). This is attributed to the different morphology and structure of the two PPy derived carbon materials. The inter-particle resistance of the N-CNS powder material is large and mass transport is blocked by closely packed carbon spheres. In contrast, the N-CNW is made of 3-D interconnected N-doped carbon fibers, which have better electron transport pathways with efficient oxygen and electrolyte diffusion. The small difference in N-doping between N-CNS and N-CNW is neglected because the higher pyridone/pyrrolic content in N-CNS (9.62 %) than that in N-CNW (7.05 %) is compensated by the lower overall nitrogen content in N-CNS (6.71 %) than that in N-CNW (8.7 %). Furthermore, such small difference in nitrogen content and functionalities should not cause that large a difference in the ORR catalytic activity observed in the CV. After activating N-CNW with KOH, the onset and peak potentials are further shifted to higher potentials due to the transformation of N-6 (pyridinic and quaternary) nitrogen groups into highly active N-5 pyridone groups. Figure 6.6b shows the Koutecky-Levich plots based on rotating disk electrode (RDE) performance of the three carbon materials (Figure 6.7) at -1.0 V vs. SCE. The slopes of

the three carbon materials follow the trend of N-CNS > N-CNW > ON-CNW, with the calculated number of electrons transferred being 2.2, 3.3, and 3.7, respectively.

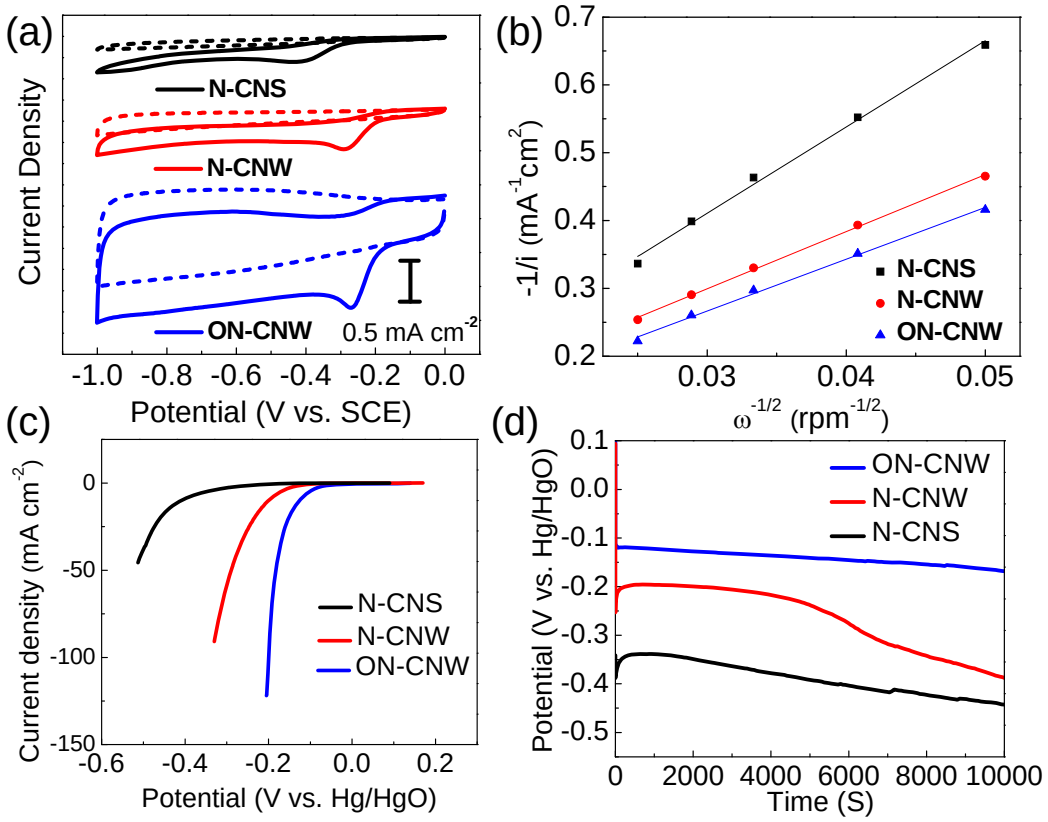

Figure 6.6. (a) Cyclic voltammetry curves, (b) Koutecky-Levich plots, (c) discharge polarization curves, and (d) chronopotentiometry (i~t) measurements of N-CNS, N-CNW, and ON-CNW.

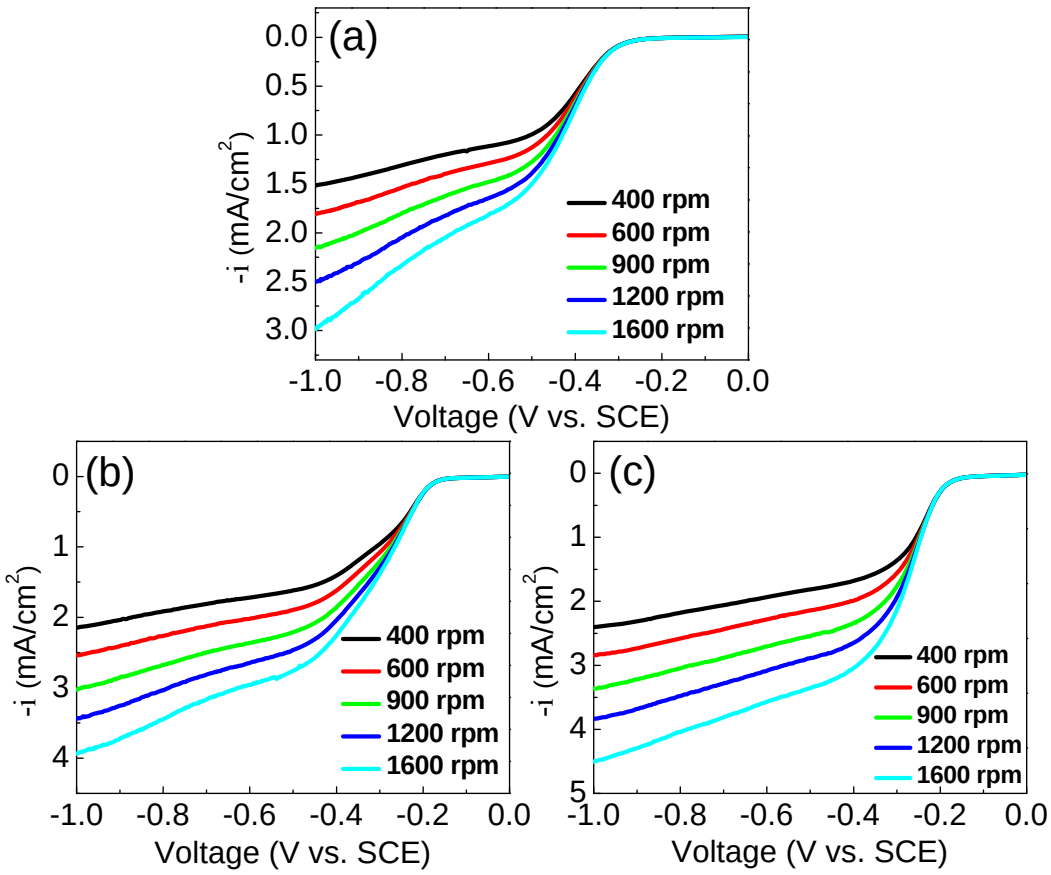

Figure 6.7. Linear sweep voltammetry curves of ORR at different rotation rates: (a) N-CNS, (b) N-CNW, and (c) ON-CNW.

The half-cell performance is shown in Figure 6.6c and d. As we can observe from the ORR polarization curves of three carbon materials in Figure 6.6c, N-CNS possesses the lowest ORR onset potential and the smallest current density. This is due to the lowest ORR catalytic activity of N-CNS. N-CNW has a much higher onset potential of around -0.15 V (vs. Hg/HgO). In addition, the current density of N-CNW at -0.3 V (vs. Hg/HgO) is 20 times larger than that of N-CNS. Among the three carbon materials, ON-CNW possesses the highest onset potential (-0.08 V vs. Hg/HgO). The current density of ON-CNW at -0.2 V (vs. Hg/HgO) is almost an order of magnitude higher than that of N-

CNW. The durability of the three carbon materials is compared in Figure 6.6d. The half cells were discharged at a current density of 10 mA cm^{-2} continuously. As we can see, ON-CNW possesses the highest discharge potential due to the best ORR catalytic activity. The stability of ON-CNW is also better than that of N-CNW because of the dominant four-electron pathway for ORR, resulting in water as the only product. But for N-CNW, significant degradation can be observed after 5000 s due to the accumulation of HO_2^- and other highly oxidative species, which are corrosive to the catalytically active sites.[145, 146]

The performances of the obtained N-CNW and ON-CNW were also evaluated in a hybrid Li-air cell. Since carbon materials are vulnerable during the OER process, an independent OER electrode was inserted into the catholyte to play the role of OER.[147] With this decoupled ORR and OER electrode design, the instability issue of the ORR catalysts during the high-voltage oxidizing charging process can be eliminated. With this approach, the well-developed ORR catalysts for fuel cells (*e.g.,* alkaline fuel cells) can also be utilized in hybrid Li-air batteries. The 3-D OER electrode consists of mesoporous $NiCo_2O_4$ nanoflakes directly grown onto a nickel foam. The obtained specific capacity was calculated based on the total mass of the catalyst in the ORR and OER electrodes (1 mg cm^{-2} + 1 mg cm^{-2}). Since the OER electrode is the same for all the cells, the difference in cell performance can only be attributed to the difference in the ORR catalyst. As we can see from Figure 6.8a, the discharge voltage plateau of ON-CNW is higher than that of N-CNW at each current density. At 0.5 mA cm^{-2}, the discharge plateau of ON-CNW is only 0.077 V lower than that of Pt/C. For N-CNW and acetylene black (AB), the differences compared with Pt/C is 0.141 V and 0.244 V, respectively. At 2.0 mA cm^{-2}, the difference in discharge voltage between ON-CNW and Pt/C is further narrowed to 0.048 V. But for N-CNW and AB, the differences compared with Pt/C are, respectively, 0.140 V and 0.267 V. The apparent decrease in the difference between ON-CNW and Pt/C when increasing the current density indicates the excellent catalytic activity of ON-CNW in fast electrochemical reactions. The cycling performance

of ON-CNW and N-CNW were compared in hybrid Li-air cells at a constant current density of 0.5 mA cm^{-2} in ambient environment. The first thirty cycles are shown in Figure 6.8b and c. While the round-trip overpotential increased from 1.00 to 1.43 V for N-CNW, the round-trip overpotential increased only slightly from 0.92 to 1.02 V for ON-CNW, revealing the high activity and stability of hybrid Li-air cells with the ON-CNW as an ORR catalyst.

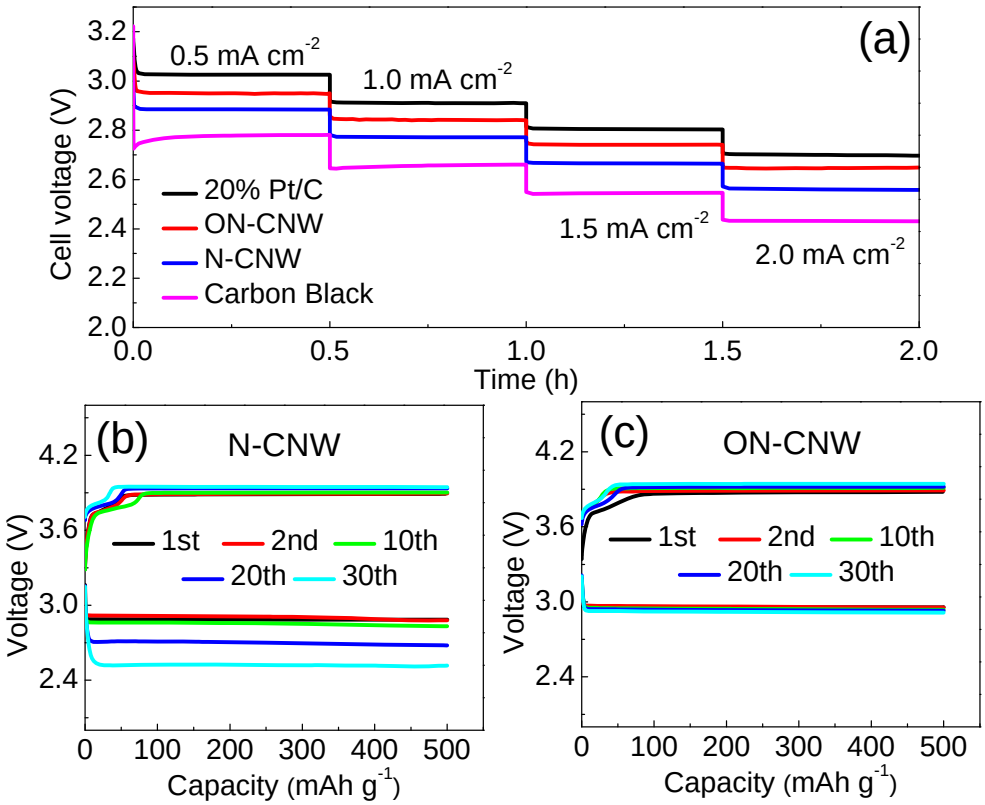

Figure 6.8. (a) Discharge voltage profiles of hybrid Li-air cells with Pt/C, N-CNW, ON-CNW, or carbon black as the ORR catalyst at different current densities, (b,c) cycling performance of hybrid Li-air cells with N-CNW or ON-CNW as the ORR catalyst and $NiCo_2O_4$ nanoflakes grown on a nickel foam as the decoupled OER electrode.

6.4 CONCLUSION

In summary, metal-free O- and N-doped carbon nanowebs have been developed as an efficient ORR catalyst for hybrid Li-air batteries. The 3-D web structure has better electron and mass transport properties, which render it a better backbone support for catalytically active sites. In addition, after carbonization and activation with KOH, the synergistic effect of O and N groups creates highly ORR active pyridone groups on the nanoweb surface. The obtained ON-CNW not only possesses high intrinsic ORR activity, but also facilitates the Li-air cell reaction with similar efficiency as that of commercial Pt/C catalyst. The novel 3-D nanoweb structure and the general methodology to integrate O and N groups to form highly active sites for ORR open up a new avenue to develop efficient and cost-effective catalysts for hybrid Li-air batteries.

Chapter 7: Advanced hybrid Li-air batteries with high-performance mesoporous nanocatalysts

7.1 INTRODUCTION

Following the first aprotic Li-air battery work in 1996, most of the efforts on Li-air batteries have been on the development of efficient catalysts to lower the high overpotentials associated with the formation ($\eta \sim 0.3$ V) and decomposition ($\eta > 1$V) of Li_2O_2 in aprotic electrolytes.[93, 148, 149] However, more detailed characterizations of the discharge and charge products recently reveal that the traditional materials used in battery research, such as organic carbonate electrolytes, carbon support, and even poly(vinylidene difluoride) binder, are not stable during the discharge and charge processes, which is believed to result from the formation of superoxide radical (*i.e.*, O_2^-).[108, 150-153] Hybrid Li-air batteries with a solid-electrolyte membrane, originally designed to protect the lithium metal anode from the contaminants in air, can avoid these detrimental side reactions in aprotic Li-air batteries.[6] But the reported cycle life of hybrid Li-air batteries is limited, making it hard to achieve the high theoretical energy density of the Li-O_2 couple.

One persistent problem limiting the cycle life of hybrid Li-air batteries is the low activity and limited durability of the bifunctional air electrodes. To overcome the carbon corrosion during the high-voltage charge process, the concept of decoupling the oxygen reduction reaction (ORR) and oxygen evolution reaction (OER) electrodes was first demonstrated with metal hydrid-air batteries in 1995 and applied recently to hybrid Li-air batteries.[4, 154, 155] A third electrode, made by metal mesh (including nickel, stainless steel, or titanium) played the role of OER, independent of the ORR electrode. However, significant degradation in cell performance could still be observed after an extended cycling test. For the OER electrode, the pure metal mesh suffers from high overpotential and low stability due to small surface area, low catalytic activity, and passivation at high potentials. For example, the typical specific surface area of a nickel mesh is less than 1

m^2 g^{-1}, offering limited catalytically active sites.[14] In addition, less conductive phases involving Ni^{4+} tend to form on the nickel surface at high potentials, degrading its OER performance.[156]

Although the decoupled design could avoid the ORR electrode during the high-voltage charge process, the ORR at the cathode is sluggish, which usually requires a noble metal catalyst like Pt or its alloys to retain a high discharge voltage. However, the high cost and scarcity of Pt will impede the wide application of hybrid Li-air batteries.[37, 124] To develop low-cost ORR catalysts with earth-abundant elements, carbon-based catalysts, such as graphene nanosheets, N-doped graphene, and carbon nanotubes have been pursued in hybrid Li-air batteries.[81, 86, 157] Another class of promising carbon materials is N-doped mesoporous carbon (NMC), which has not yet been explored in hybrid Li-air batteries. The advantage of NMC lies in the large mesoporous surface area, which provides large number of catalytically active sites and fast electrolyte/oxygen diffusion.

Here, we demonstrate an advanced hybrid Li-air cell with mesoporous nanocatalysts, which exhibits the best reported cycling performance so far (Table 7.1). The cell could be cycled for over 100 cycles (400 hours) in air with only 0.08 V increase in round-trip overpotential based on discharge and charge end voltages. Mesoporous $NiCo_2O_4$ nanoflakes were directly grown onto a nickel foam (NCONF@Ni) to serve as the OER electrode. With this approach, the catalytically active surface area is increased from less than 1 m^2 g^{-1} to more than 80 m^2 g^{-1}. Moreover, the spinel $NiCo_2O_4$ catalyst possesses much higher catalytic activity and stability than Ni metal at high potentials, leading to a fairly low OER overpotential that is comparable to that seen with the noble-metal IrO_2 catalyst. A nitrogen-doped mesoporous carbon (NMC) with extremely high surface area (1520 m^2 g^{-1}) and optimized nitrogen doping content (3.9 wt. %) was loaded onto a hydrophobic carbon fiber paper to act as the ORR electrode. The highly mesoporous NMC exhibits activity similar to but stability much better than that of the noble-metal Pt/C catalyst.

No.	Catalyst	Current density	Total cycling time (h)	Round-trip overpotential increased (V)	Ref.
1	$Sr_{0.95}Ce_{0.05}CoO_{3-\delta}$-Cu	0.2 mA cm^{-2}	37.5*	~0.26*	89
2	Pt	0.5 mA cm^{-2}	60*	~0.26*	67
3	N-doped carbon nanotubes grown onto carbon fiber paper	0.5 mA cm^{-2}	65	0.23	87
4	Heat-treated graphene nanosheets	0.5 mA cm^{-2}	200	~ 0.23*	86
5	Stainless steel + commercial ORR electrode (decoupled)	2 mAh cm^{-2}	<200 (Li-water)	~ 0.16*	4
6	Titanium + Mn_3O_4/C (decoupled)	0.5 mA cm^{-2}	80	~ 0.21*	155
7	NCONF@Ni + NMC (decoupled)	0.5 mA cm^{-2}	400	0.08	This work

Table 7.1. Summary of the cycling performances of prominent hybrid Li-air batteries developed world-wide.

7.2 EXPERIMENTAL

IrO_2 nanopowder was synthesized by a modified Adams method as detailed in our previous report.[140] $NiCo_2O_4$ nanoflakes grown onto nickel foam was obtained by a hydrothermal method followed by post-calcination in air.[158] The hydrothermal treatment was carried out once on each side to ensure the uniform distribution of catalyst on both sides. In one treatment, 0.5 mmol of $Ni(NO_3)_2$•$6H_20$, 1 mmol of $Co(NO_3)_2$•$6H_20$, and 3 mmol hexamethylene-tetramine were dissolved in a mixture of de-ionized water and

ethanol (30 mL, 2:1 v/v), resulting in a mole ratio of 1 : 2 : 6. The obtained solution was transferred into a Teflon-lined stainless-steel autoclave. A pre-cleaned nickel foam (2 cm × 4 cm) was immersed into the obtained solution with one side facing down. The autoclave was sealed and maintained at 90 °C for 10 h. After the solution was cooled down, the nickel foam was covered with a layer of greenish Ni-Co precursor preferably on the side facing down. The nickel foam was cleaned and subjected to the second hydrothermal treatment with the other side facing down. The nickel foam deposited with the Ni-Co precursor was finally annealed at 320 °C for 2 h in air. Greenish Ni-Co precursor precipitate in the solution was also collected, washed, and annealed with the same procedure to obtain $NiCo_2O_4$ nanoflakes powder. The nickel foam with 1 mg cm^{-2} of the $NiCo_2O_4$ nanoflakes was cut into small pieces with a dimension of 0.76 cm × 0.76 cm. To obtain 0.5 mg cm^{-2} or 2.8 mg cm^{-2} of the $NiCo_2O_4$ nanoflakes, the concentration of the solutions was adjusted while keeping the ratio of $Ni(NO_3)_2$•$6H_20$, $Co(NO_3)_2$•$6H_20$, and hexamethylene-tetramine constant.

The nitrogen-doped mesoporous carbon (NMC) was synthesized by a direct activation of amorphous mesoporous carbon (AMC, 1.5 g) under flowing ammonia (60 mL min^{-1}) at 1000 ^oC for 1 h with a heating rate of 50 ^oC min^{-1}.[159] The AMC was synthesized by carbonization of nanostructured polymeric composites, which were obtained by self-assembly of block copolymer (Pluronic F127) and phenolic resin (phloroglucinol−formaldehyde) under acidic conditions via a soft-template method.[160] In a typical synthesis, a 2 L flask was charged with 26.2 g of phloroglucinol, 52.4 g of F127, and 10.0 g of aqueous HCl (37 wt%) in 1300 mL of ethanol. The mixture was heated to reflux with stirring. To this solution, 26.0 g of aqueous formaldehyde solution (37 wt. %) was added. Precipitates appeared at about 4 min after the addition of formaldehyde, indicating the formation of F127−phenolic resin polymeric composites. The reaction mixture was stirred for 2 h and then filtered. The yellow polymer particles were washed with ethanol and dried in an oven at 100 ^oC for 3 h. Carbonization was

carried out under flowing nitrogen (100 mL min^{-1}) by heating the polymer particles to 900 ^{o}C with a heating rate of 2 ^{o}C min^{-1} and maintaining the final temperature for 2 h.

The morphology and microstructure of the prepared samples were examined with a FEI Quanta 650 scanning electron microscope (SEM) and JEOL 2010F transmission electron microscope (TEM) at 200 KeV. The elemental mapping results were examined with an energy dispersive spectrometer (EDS) attached to the FEI Quanta 650 SEM. X-ray photoelectron spectroscopy (XPS) analysis was conducted with a Kratos Analytical spectrometer. The deconvolution of the XPS spectrum was performed using CasaXPS software with Gaussian-Lorentzian functions and a Shirley background. N_2 physisorption was performed on a Micromeritics Tristar analyzer at 77 K. Prior to the measurement, the sample was purged with flowing N_2 at 423 K for 2 h. The specific surface area was calculated by the Brunauer–Emmett–Teller (BET) method from the nitrogen adsorption data in the relative pressure range (P/P0) of 0.06–0.20. The total pore volume was determined from the amount of N_2 uptake at a relative pressure of P/P0 = 0.95. The pore size distribution plot was derived from the adsorption branch of the isotherm based on the Barrett–Joyner–Halenda (BJH) model.

The linear sweep voltammetry (LSV) of NMC and Pt/C was tested in a standard rotating disk electrode (RDE) setup with an Autolab PGSTAT302N potentiostat (Eco Chemie B.V.). The catalyst ink (5 mg mL^{-1}) was made by sonicating the catalyst powder (10 mg) in ethanol (2 mL). The catalyst ink (3, 5, 7 μL) was then loaded onto the glassy carbon electrode (5 mm diameter) followed by drying in air. 5 μL of Nafion solution (0.5 wt. %) was then dropped onto the top of the catalyst layer to form a protective layer. LSVs were obtained by sweeping the potential from 0.0 to -1.0 V (vs. SCE) at 1600 rpm with a scan rate of 10 mV s^{-1} in O_2 saturated 0.1 M KOH solution. Chronopotentiometry curves were obtained at -0.28 V and 1000 rpm. The half-cell test was conducted in a three-electrode half-cell with 0.5 M LiOH + 1 M $LiNO_3$ as the electrolyte.[140] Polarization curves were recorded on a VoltaLab PGZ 402 potentiostat by sweeping the potential at a scan rate of 10 mV s^{-1}. Chronopotentiometry (i~t) data were collected on an Arbin BT

2000 battery cycler. The half-cell polarization curves and chronopotentiometry data were manually corrected for iR loss.

A PTFE layered battery mould was used to carry out the full cell test. The anode side was assembled in an argon-filled glove box and then combined with the cathode side in air. The anode side consisted of a nickel foam current collector, a lithium metal foil, and the organic carbonate electrolyte (1 M LiPF6 in ethylene carbonate (EC) / diethylcarbonate (DEC) (1:1 v/v)) absorbed by two layers of Celgard® polypropylene. The cathode side consisted of 2 mL of 0.5 M LiOH + 1 M $LiNO_3$ solution as the catholyte, an air electrode (0.76 cm × 0.76 cm), and a platinum mesh current collector. The method to prepare the air electrode has been reported elsewhere.[140] A LTAP ($Li_{1+x+y}Ti_{2-x}Al_xP_{3-y}Si_yO_{12}$) membrane (0.15 mm thick, = 1×10^{-4} S cm^{-1}, 0.76 cm × 0.76 cm, OHARA Inc., Japan) was used as the separator. In the conventional air electrode, the catalysts include Pt/C (20 wt. %, 1 mg cm^{-2}, Johnson Matthey) and IrO_2 nanopowder (1 mg cm^{-2}). In our cell with mesoporous nanocatalysts, an additional oxygen evolution electrode ($NiCo_2O_4$ nanoflakes on nickel foam, 1 mg cm^{-2}, 0.76 cm × 0.76 cm) was immersed into the catholyte between the solid electrolyte and ORR air electrode (nitrogen-doped mesoporous carbon, 1 mg cm^{-2}). A nickel wire was attached to the nickel foam to conduct current. The cathode side of the hybrid cell was purged with water-saturated air during operation to suppress the evaporation of water from the catholyte. The polarization curves were obtained by sweeping the potential at a scan rate of 10 mV s^{-1} with a VoltaLab PGZ 402 potentiostat. Discharge-charge experiments were conducted with an Arbin BT 2000 battery cycler with a 5-minute rest time between each discharge and charge period. For the cell with mesoporous nanocatalysts, two independent Arbin channels were used to collect the discharge and charge data alternatively with a 5-minute rest time between each discharge and charge period.

7.3 RESULT AND DISCUSSION

Figure 7.1 shows the cell configuration of the hybrid Li-air cell with the mesoporous nanocatalysts. The bifunctional air electrode consists of two independent electrodes, one optimized for ORR and the other optimized for OER. Upon discharge, oxygen from air is absorbed and reduced by the N-doped mesoporous carbon and combine with water in the catholyte and Li^+ ions coming from the anode through the solid electrolyte ($Li_{1+x+y}Ti_{2-x}Al_xP_{3-y}Si_yO_{12}$ (LTAP), Ohara Inc., Japan) to form LiOH as the discharge product. The N-doped mesoporous carbon was loaded onto a hydrophobic carbon fiber paper to maximize catholyte/NMC/air three-phase interface for ORR. The large mesoporous surface area along with N-doping provides a large amount of catalytically active sites and fast electrolyte/oxygen diffusion, which lowers the reaction overpotential.[161, 162] The nitrogen functional groups are highly active and durable as each of them is anchored onto the carbon surface. In addition, in comparison with many so-called "metal-free" catalysts, which actually may contain small amounts of metals from the synthesis process, this NMC is totally free of metal based on the synthesis process used and is truly cost-effective for practical applications.[163]

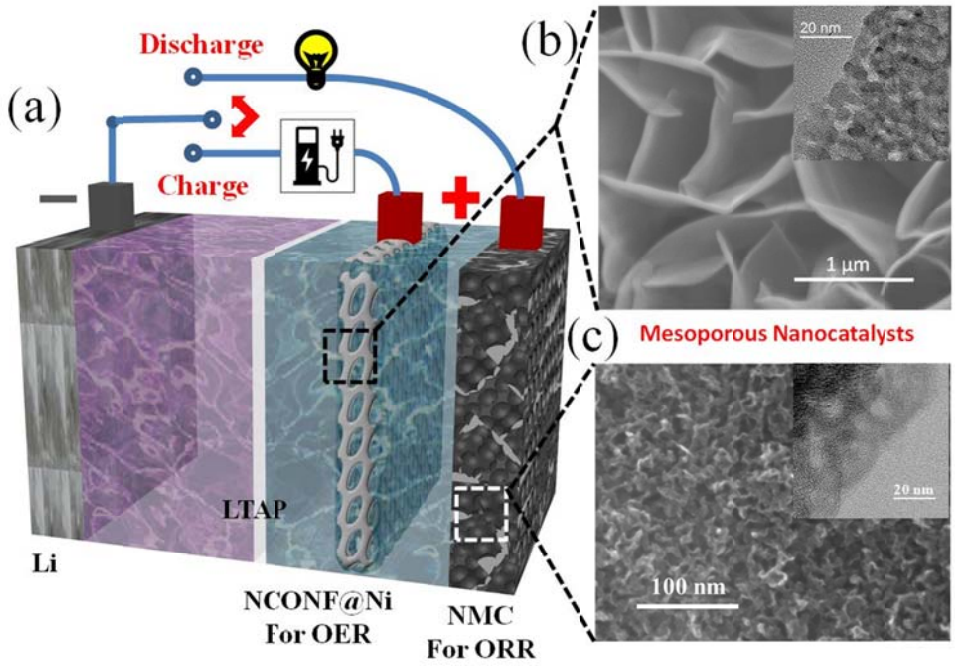

Figure 7.1. (a) Schematic representation of the hybrid Li-air cell with mesoporous nanocatalysts. (b) SEM and TEM images showing the mesoporous $NiCo_2O_4$ nanoflakes directly grown onto a nickel foam as the OER catalyst. (c) SEM and TEM images showing the N-doped mesoporous carbon as the ORR catalyst.

Upon charge, the NMC electrode is disengaged from the Li metal anode due to the vulnerability of carbon during the high-voltage charge process. Instead, the NCONF@Ni electrode is engaged with the Li metal anode during charging. With the high-voltage applied onto the NCONF@Ni electrode, oxygen bubbles will form on the NCONF@Ni electrode through the highly oxidizing intermediate species.[115] The NCONF@Ni electrode is totally carbon- and binder- free, with the mesoporous NiCo2O4 nanoflakes directly grown onto a nickel foam, which makes it highly durable in the high-voltage, oxidizing environment. The spinel $NiCo_2O_4$ is known for its low intrinsic electrical resistivity, fairly low oxygen overpotential, and high corrosion stability in

alkaline media.[164] In addition, the 3-D interconnected porous structure of the nickel foam substrate can reduce the polarization and improve the catalytic efficiency by increasing the active sites, enhancing the mass transfer of reactants or products, and keeping smooth electron pathways for the rapid electrochemical reactions.[165] The pure nickel form is not a good OER electrode because the overpotential for OER is high and stability is poor due to the formation of low-conductivity phases involving Ni^{4+} at high potentials.[156] These problems can be solved by applying highly active electrocatalysts onto the nickel surface. Each $NiCo_2O_4$ nanoflake is directly connected to the nickel foam backbone, which also acts as the current collector, indicating all the nanoflakes could participate in the OER during charge.

More detailed features of the $NiCo_2O_4$ nanoflakes were observed by SEM and TEM analysis (Figure 7.2a, Figure 7.3). The nanoflakes are of micron size and very thin as they appear in the low-magnification image. Well-crystallized $NiCo_2O_4$ nanocrystals can be clearly observed at high magnification. Two groups of crystal planes are indexed to be the (111) and (311) planes of the cubic spinel $NiCo_2O_4$, based on their interplanar spacings (0.472 nm and 0.245 nm). The X-ray diffraction (XRD) pattern of the electrode containing $NiCo_2O_4$ nanoflakes on nickel foam is shown in Figure 7.2b. Strong reflections of Ni(111) and Ni(200) planes in the nickel foam substrate can be seen along with the minor peaks of the spinel $NiCo_2O_4$ nanoflakes. From the TEM images, we can see that these nanosheets in fact possess uniformly distributed mesopores throughout the whole surface, which are consistent with the isotherm and pore size distribution results in Figure 7.2c. The diameter of these pores is about 5 nm, which are produced by the gas released during the post-calcination step. This nanoflake morphology and mesoporous mircostructure indicate the large specific surface area of this material, which is beneficial for the OER to occur mainly on the surface of the catalyst.[164]

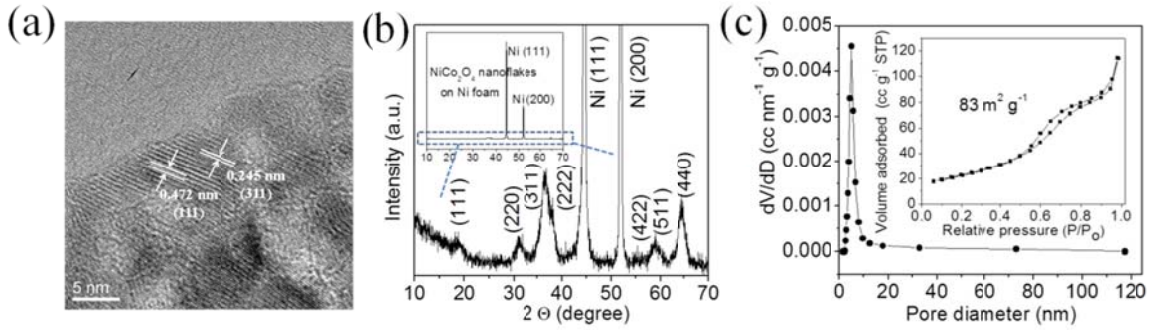

Figure 7.2. (a) TEM image of the synthesized mesoporus $NiCo_2O_4$ nanoflakes scratched from the nickel foam. (b) XRD of the nickel foam with $NiCo_2O_4$ nanoflakes grown on it. (c) N_2 adsorption-desorption isotherm and pore size distribution of the $NiCo_2O_4$ nanoflakes.

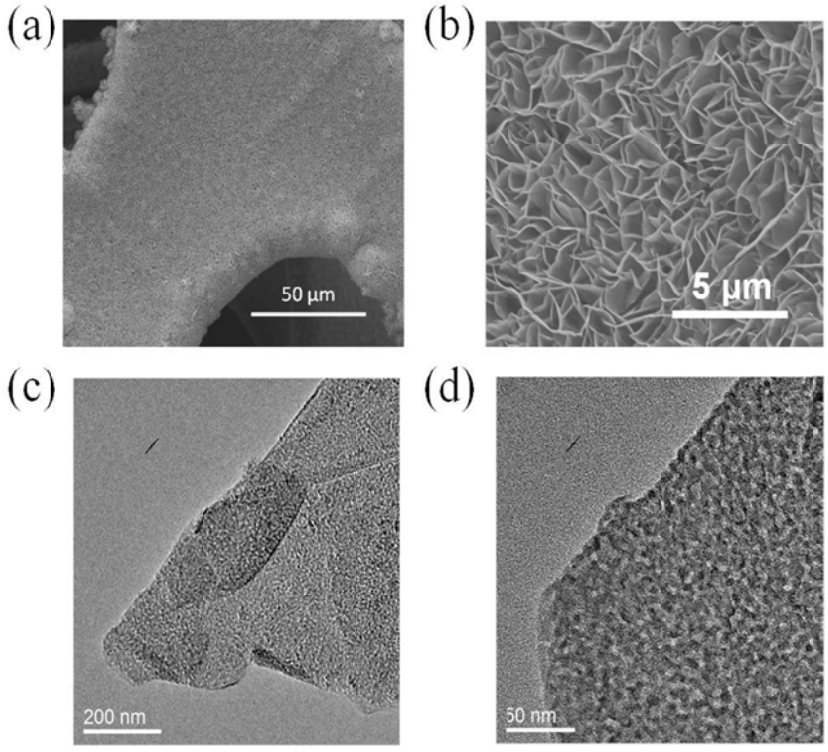

Figure 7.3. SEM and TEM images of the synthesized $NiCo_2O_4$ nanoflakes on the nickel foam.

The activity and durability of the synthesized NCONF@Ni electrode were tested in a three-electrode half-cell with a Hg/HgO reference electrode and a platinum flag counter electrode.[140] As a comparison, the OER activity and durability of a blank nickel foam and IrO_2 nanopowder (Adams fusion method) were also measured with the same half-cell configuration. The loadings of the catalysts were all controlled to be 1 ± 0.02 mg cm^{-2}. The exposed electrode area was 0.76 cm × 0.76 cm for all the electrodes. As we can see from Figure 7.4a, the pristine nickel foam has very low OER catalytic activity with an onset potential at 0.75 V vs. Hg/HgO. After growing the $NiCo_2O_4$ nanoflakes onto the nickel foam, the onset potential is lowered and the current densities are much higher than those of the pristine nickel foam. A small bump can be seen at around 0.55 V vs. Hg/HgO, corresponding to the M-O/M-O-OH redox couple (M represents Ni and Co ions).[158, 166] It is shown that the OER catalytic activity of the $NiCo_2O_4$ nanoflakes grown onto nickel foam is comparable to that of IrO_2 nanopowder loaded onto a carbon paper, which is the conventional OER electrode in metal-air batteries. This conclusion is valid with various loadings as shown in Figure 7.5. The 3-D interconnected porous structure of the nickel foam substrate can reduce the polarization and improve the catalytic efficiency by increasing the active sites, enhancing the mass transfer of reactants or products, and keeping smooth electron pathways for the rapid electrochemical reactions.[165]

The durability of NCONF@Ni as shown in Figure 7.4b was tested by the chronopotentiometry (voltage vs. time) method at an anodic current density of 20 mA cm^{-2} in the half-cell. IrO_2 and NCONF@Ni have the lowest charge potential, while the pristine nickel foam has the highest charge potential, which is consistent with the OER activity of these materials in Figure 7.4a. The fluctuation on the voltage profiles is due to oxygen bubble formation and detachment from the electrode surface. While all the electrodes show gradual increase in charge potential, the pristine Ni foam shows a higher rate of increase than other electrodes due to the low OER activity and instability of the nickel metal under the high-voltage charge process. Repeated tests showed the same results presented in Figure 7.4a and b.

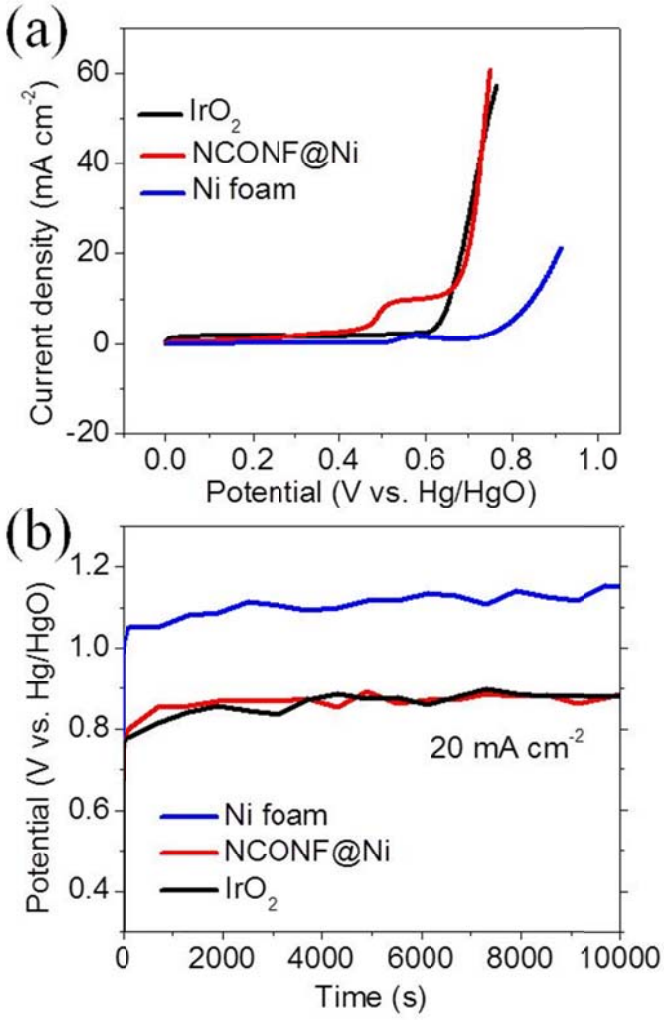

Figure 7.4. OER performance of the catalysts: (a) polarization curves and (b) chronopotentiometry plots.

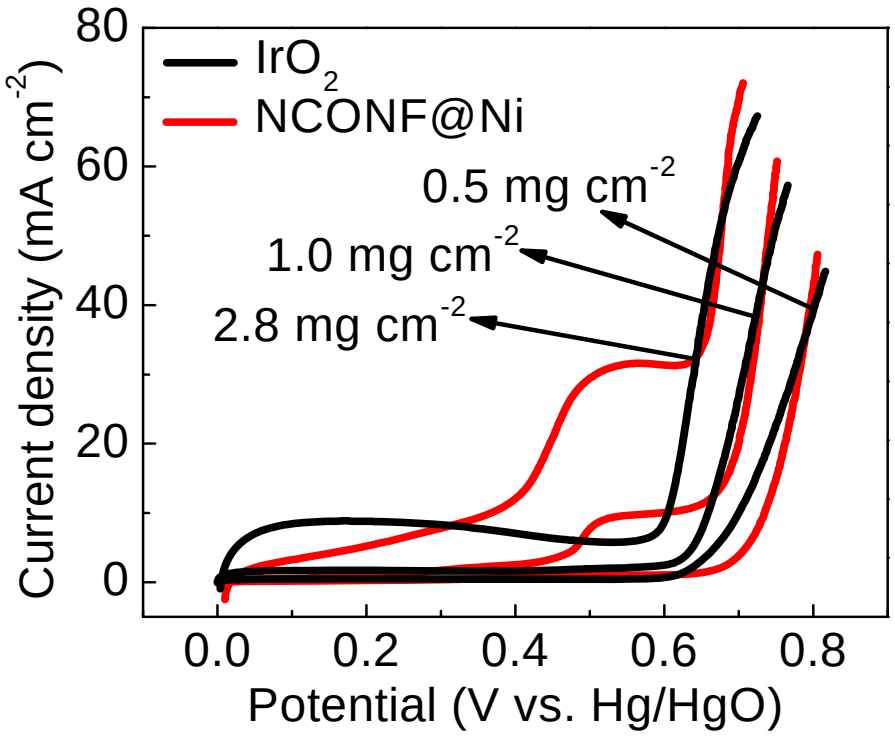

Figure 7.5. Loading-dependent polarization curves of IrO_2 and NCONF@Ni.

The nitrogen-doped mesoporous carbon (NMC) is a highly active ORR catalyst for hybrid Li-air batteries with activity similar to but stability better than that of Pt/C. The SEM and TEM images are shown in Figure 7.1c and Figure 7.6. The NMC contains a large amount of irregular mesopores all over the carbon surface. Figure 7.7a shows the N_2 sorption isotherms and BJH mesopore size distribution plots of NMC. It possesses an extremely high BET surface area of 1520 m^2 g^{-1}, most of which are contributed by the mesopores (Figure 7.7b).[160] This high surface area acts as an ideal backbone support for a high density of catalytically active sites for ORR.[159] As we can see from the elemental mapping results in Figure 7.8, nitrogen has been uniformly doped into the mesoporous carbon. Based on the X-ray photoelectron spectroscopy (XPS) data, the nitrogen content is 3.9 wt. %. This doping content is within the range to achieve the largest improvement

in oxidation stability and conductivity of nitrogen doped mesoporous carbons.[167] The nitrogen functional groups are determined to contain mostly pyridinic and quaternary nitrogen (Figure 7.7c),[142] which are reported to possess high ORR activity.[168, 169] It also possesses a narrow mesopore size distribution with a large pore volume of 1.62 $cm^3 g^{-1}$. The peak pore size has been determined to be about 10 nm, which is in agreement with the TEM observation. The large pore volume contributes to fast transport of O_2 and aqueous electrolyte to active sites, leading to high activity.[161]

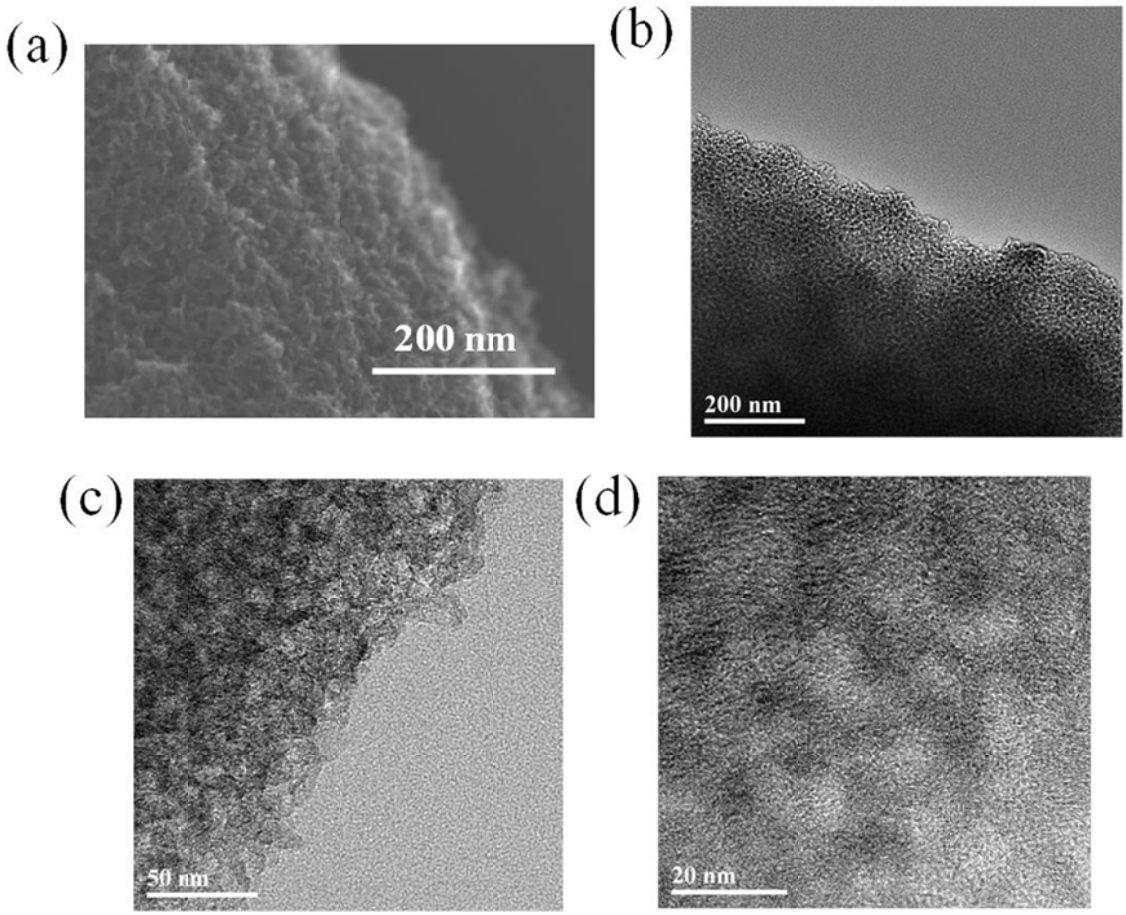

Figure 7.6. SEM and TEM images of the synthesized N-doped mesoporous carbon.

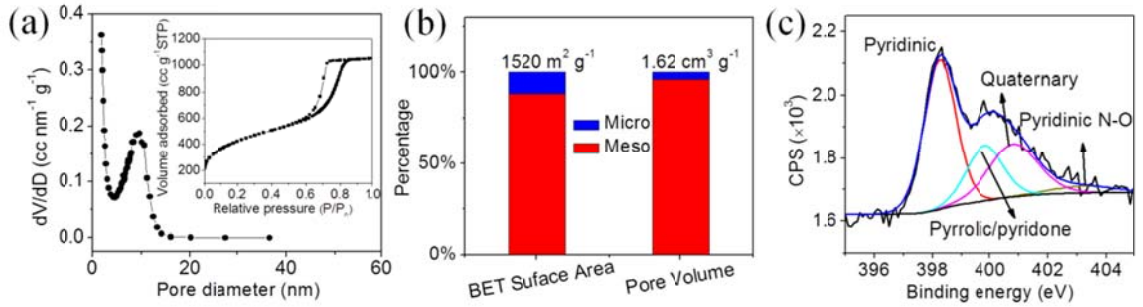

Figure 7.7. SEM and TEM images of the synthesized N-doped mesoporous carbon.

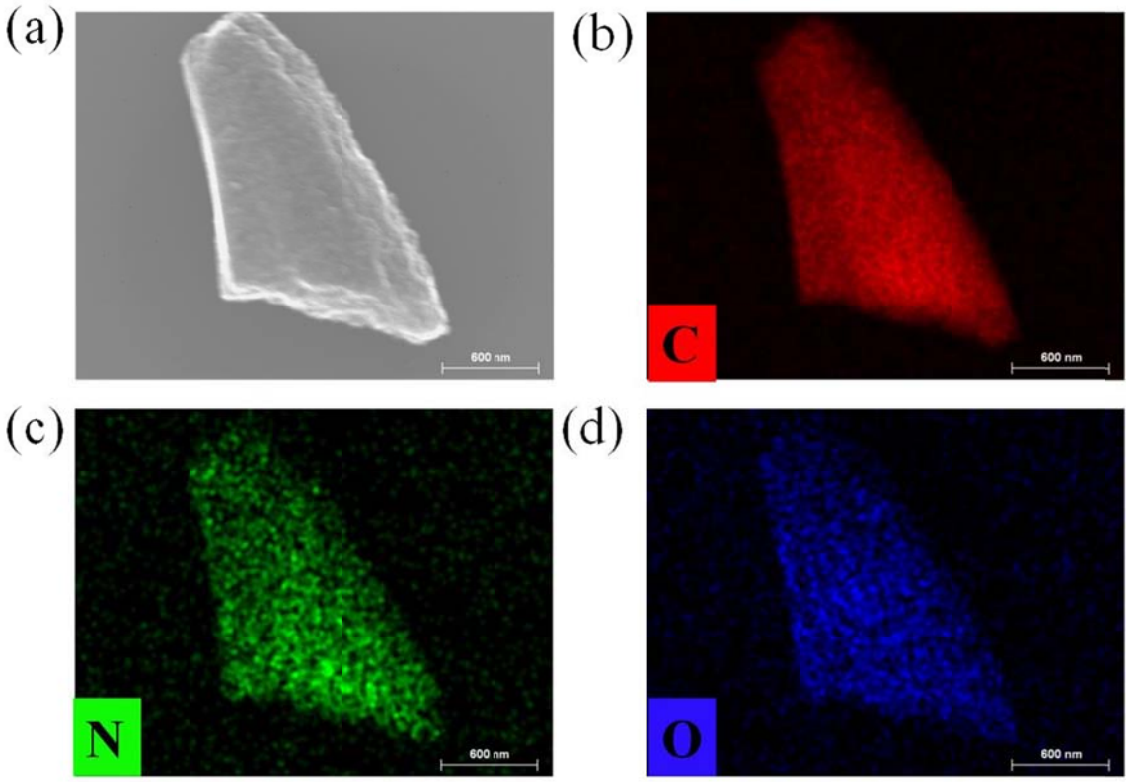

Figure 7.8. SEM image and EDX mappings of one single N-doped mesoporous carbon particle.

The activity and durability of the NMC were tested on a rotation disk electrode (RDE) shown in Figure 7.9. For a comparison, the curves of the commercial Pt/C catalyst are also shown. The loadings of catalysts were all controlled to be 128 μg cm^{-2}. At least three independent tests were conducted to confirm constant performance of catalysts. As can be seen from Figure 7.9a, although the onset potential of Pt/C is higher than that of NMC, the current densities of NMC increased faster than that of Pt/C, which surpasses Pt/C below -0.73 V vs. SCE. This "crossing" feature is widely reported for highly active metal-free ORR catalysts.[126, 169, 170] Although the current density of NMC is less than that of Pt/C at low overpotentials, its higher current at higher overpotentials has special advantages in hybrid Li-air batteries with a wide range of operating voltage. The loading dependent polarization curves were also measured as shown in Figure 7.10. The limiting current of Pt/C remained relatively constant with various loadings, which is in agreement with previous studies.[171] However, the limiting current of NMC increased with increasing loading, which is possibly due to an enlarged thickness of the catalyst layer enhancing the "pseudo" 4-electron ORR path on the carbon-based catalyst surface.[172, 173] The durabilities of NMC and commercial Pt/C catalyst are compared in Figure 7.9b in an O_2 saturated 0.1 M KOH solution at -0.28 V and 1000 rpm. Although the current densities of both NMC and Pt/C decrease with time, the NMC exhibits a much slower decrease compared to commercial Pt/C, indicating that NMC is much more stable than Pt/C.[174]

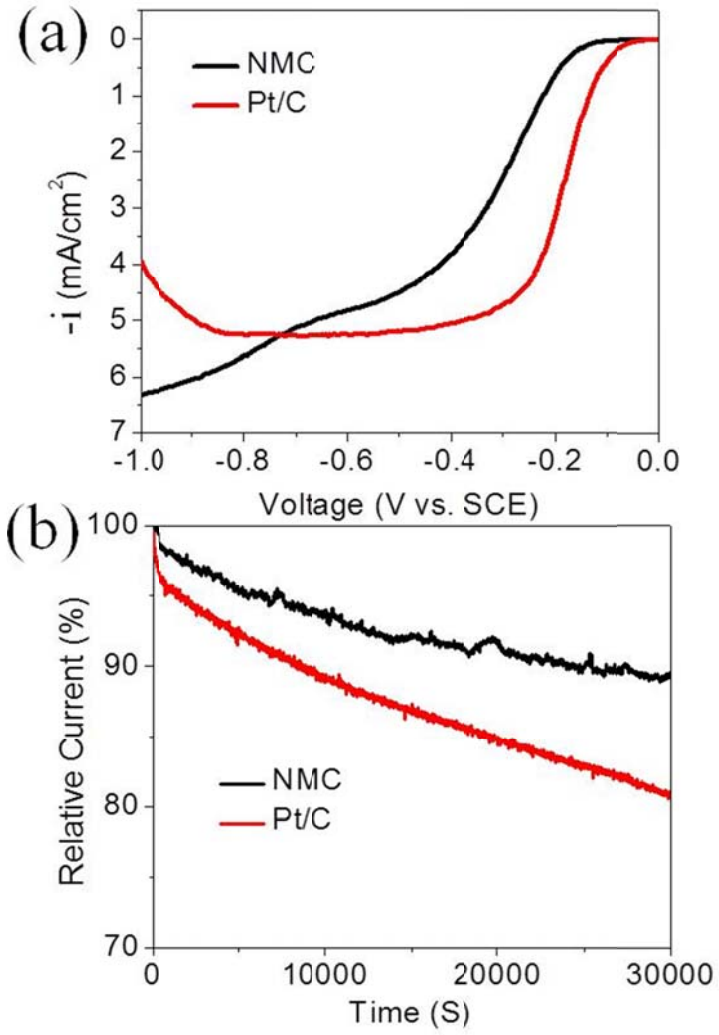

Figure 7.9. Comparison of the ORR performances of NMC and Pt/C: (a) linear sweep voltammetry curves and (b) chronopotentiometry plots.

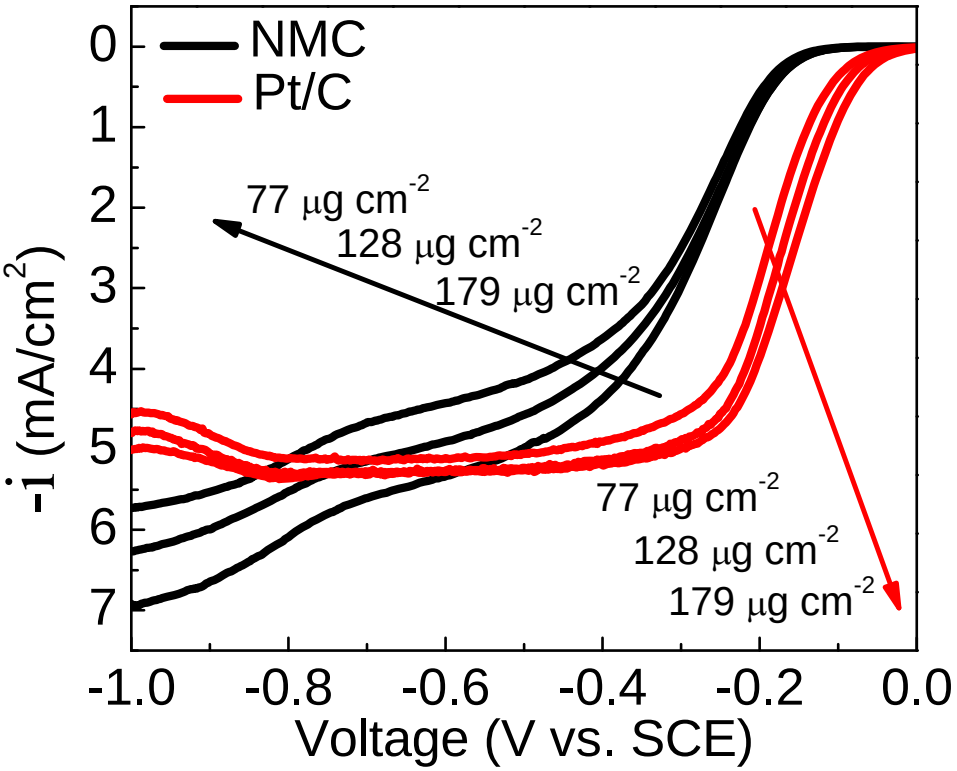

Figure 7.10. Loading-dependent polarization curves of NMC and Pt/C.

Figure 7.11a shows the charge and discharge polarization curves of a rechargeable hybrid Li-air battery with the mesoporous nanocatalysts; NMC and NCONF@Ni served as, respectively, the ORR and OER catalysts. As a comparison, the cell performance with Pt/C + IrO_2 is also shown in Figure 7.11a. Pt/C and IrO_2 are among the most active catalysts for ORR and OER, respectively.[171] The NMC + NCONF@Ni air electrodes show current densities similar to the Pt/C + IrO_2 air electrode for both discharge and charge in the hybrid Li-air batteries. In our previous report, the OER polarization curves with insufficient OER catalyst were bent due to the oxidation of the carbon support.[140] Here, we have sufficient IrO_2 loading in the Pt/C + IrO_2 bifunctional electrode and no carbon in the NCONF@Ni OER electrode so that both curves fulfill the linear

relationship between voltage and current. These two curves almost overlap with each other, proving that the OER activity of NCONF@Ni is similar to that of IrO_2 nanopowder in hybrid Li-air batteries. Pt/C and NMC have very close polarization curves toward ORR, indicating that the metal-free NMC has catalytic activity similar to the noble-metal Pt/C catalyst. Both curves feature an abrupt drop at the initial part due to the activation polarization and a linear increase in current density with decreasing cell voltage due to the large resistance of the solid electrolyte. The maximum power densities were 12.3 mW cm^{-2} and 11.5 mW cm^{-2}, respectively, for Pt/C and NMC.

Our results show the use of IrO_2 as an OER catalyst improves the cycling performance of hybrid Li-air batteries.[69, 140] It not only lowers the charge potential, but also suppresses carbon support corrosion. Although the degradation of Pt/C + IrO_2 is much slower than that of the Pt/C-only air electrode, the degradation is significant after long cycle tests. Figure 7.11b shows the cycling performance of the hybrid Li-air batteries with the Pt/C + IrO_2 air electrode. The cells were cycled at a current density of 0.5 mA cm^{-2} for 2 h discharge and 2 h charge per cycle, contributing to a capacity of 500 mAh g^{-1} based on the total mass of the ORR and OER catalysts (2 mg cm^{-2}). The discharge voltage of acetylene black (AB, 2.78 V) and the charge voltage of pristine nickel foam (4.05 V) at the same current density were selected as the discharge and charge cut-offs. We can see from Figure 7.11b that both the discharge and charge performances degrade apparently upon cycling. The discharge overpotential increases upon cycling and the discharge voltage drops below the discharge voltage of AB in 40 cycles, which means the air electrode somehow lost the catalytic activity of Pt. The charge overpotential also increases substantially in 40 cycles. Repeated tests showed similar cycling performance, which exclude the influence of other factors (*i. e.* cell assembling, catalyst coating, *etc.*) on the cell performance. The SEM images of the Pt/C + IrO_2 electrode before and after cycling are shown in Figure 7.12. A lot of damage to the catalyst layer could be found, leading to the decreased cell performance.

The cycling performance of the mesoporous nanocatalysts with NCONF@Ni as the OER catalyst and NMC as the ORR catalyst is shown in Figure 7.11c. The discharge and charge voltge profile is split into two branches because the discharge and charge data were collected by two independent Arbin channels alternatively. We can see that both the discharge and charge performances are very stable on cycling over 100 cycles, which is a substantial improvement compared with the conventional Pt/C + IrO_2 bifunctional air electrode. The discharge voltage of NMC is well above that of AB (2.78 V) through 100 cyles, indicating its high activity and durability due to the nitrogen-doping and highly mesoporous structure. The charge voltage of NCONF@Ni is well below that of the nickel foam (4.05 V) through 100 cycles, showing the NCONF coating is the active part catalyzing OER with high efficiency and long-tern stability. The round-trip overpotential based on discharge/charge end voltage is 0.92 V (efficiency 76.1 %) intially and it increases only slightly to 1.00 V at the 100^{th} cycle (efficiency 74.4 %), attributing to only 0.017 % decrease in efficiency per cycle. Repeated tests showed the same excellent cycling performance. This extraordinary activity and stability is due to the highly active and durable mesoporous nanocatalysts employed in the battery.

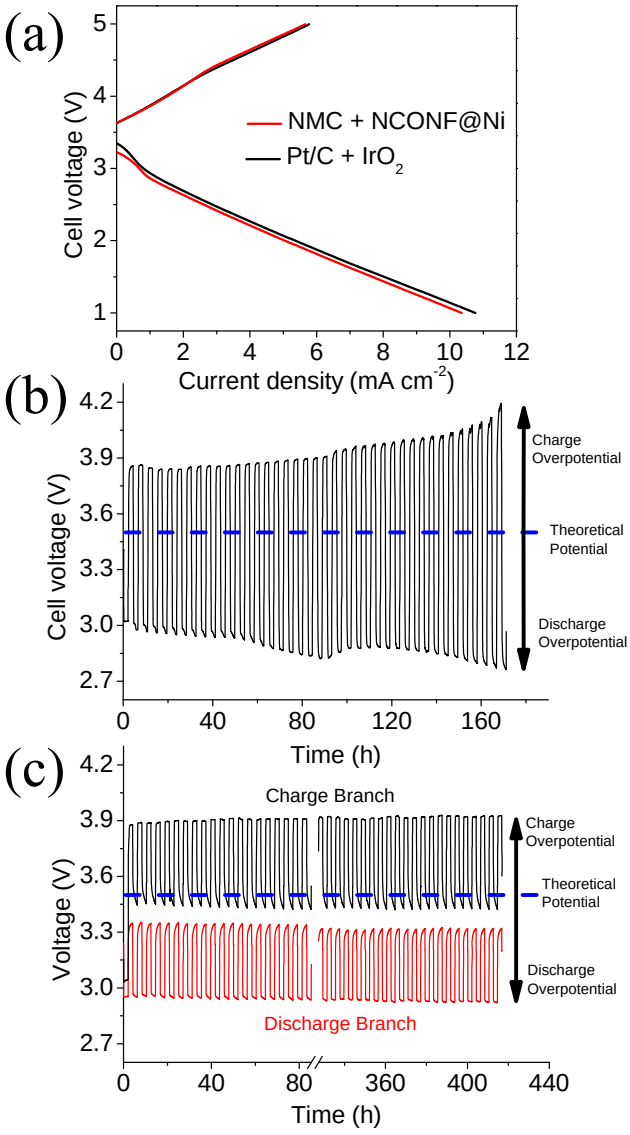

Figure 7.11. (a) Discharge and charge polarization curves of the conventional Pt/C + IrO2 air electrode and NMC + NCONF@Ni air electrode. (b) Cycling performance of the hybrid Li-air batteries with the conventional Pt/C + IrO2 air electrode at 0.5 mA cm-2 and 2-h cycle period for 40 cycles. (c) Cycling performance of the hybrid Li-air batteries with the NMC + NCONF@Ni air electrode at 0.5 mA cm-2 and 2-h cycle period for 100 cycles.

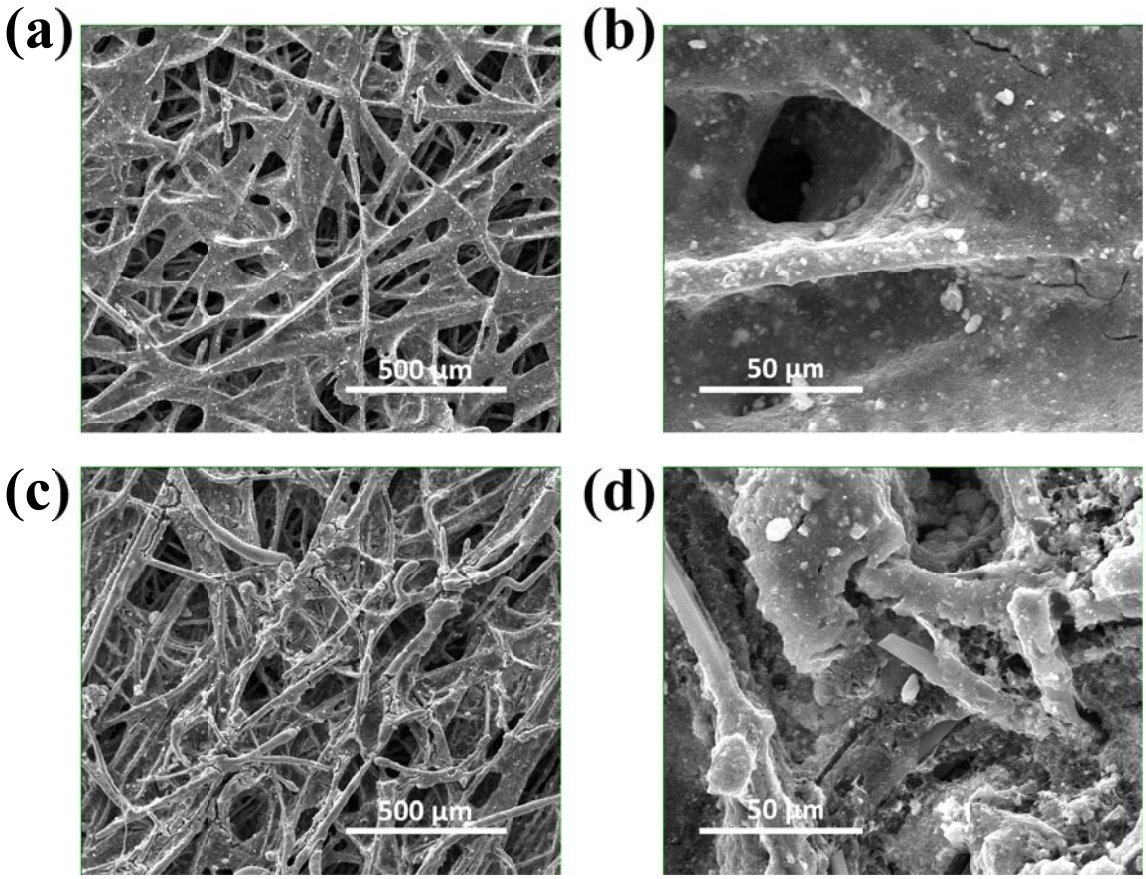

Figure 7.12. SEM images of Pt/C + IrO_2 air electrode (a,b) before and (c,d) after the cycling test.

7.4 CONCLUSION

In summary, mesoporous nanocatalysts have been developed to improve substantially the efficiency and cyclability of hybrid Li-air batteries. Mesoporous $NiCo_2O_4$ nanoflakes were directly grown onto the nickel foam to form a carbon-free 3-D OER air electrode, offering high OER activity and good electrochemical and mechanical stability during the OER process. The instability and high-cost issue of Pt/C has also been solved by replacing it with a highly active and stable nitrogen-doped mesoporous carbon possessing an extremely high surface area of 1520 $m^2 g^{-1}$ and a pore volume of 1.62 cm^3

g^{-1}. We believe the mesoporous nanocatalysts with the NCONF@Ni for OER and NMC for ORR catalyst provide a practical solution for low-cost, highly active, durable bifunctional air electrodes for hybrid Li-air batteries and other metal-air batteries.

Chapter 8: Summary

This dissertation focused on an exploration of the design and development of hybrid Li-air batteries. As a possible candidate for the next-generation high-energy batteries, the hybrid Li-air batteries are an emerging research area in recent years. The goal of this dissertation was to explore the challenges that limit the performance of hybrid Li-air batteries and put forward possible solutions. Several persistent problems have been identified. Novel design features and new materials have been employed to improve significantly the power density, efficiency, and cycle life, while lowering the cost of hybrid Li-air batteries. The approaches developed in this dissertation will be of great value to researchers in hybrid Li-air batteries and other metal-air batteries.

- *Buffer catholoytes*: Since the solid electrolytes made of oxides are the most practical choice in hybrid Li-air batteries and most oxides are only stable in a limited pH range, the use of buffer catholytes is preferable to keep the pH value of catholytes relatively constant while the discharge process continuously consumes acids or produce LiOH. Currently, buffer catholytes that have been used include acidic H_3PO_4-LiH_2PO_4, CH_3COOH-CH_3COOLi and alkaline LiOH-LiCl. Buffers with imidazole additive are more versatile (a variety of strong acids can be used), but electrochemical charging should be avoided due to the instability of imidazole at high potentials.
- *Internal resistance*: The operation current density of hybrid Li-air batteries is fairly low (0.5 mA cm^{-2}) compared with competitors like Zn-air batteries. The problem is that the total internal resistance of a prototype hybrid Li-air battery is too high (around 200 Ω cm^2). For example, a current density of 15 mA cm^{-2} will result in an ohmic polarization of 3.0 V, which takes up most of the open-circuit cell voltage of hybrid Li-air batteries. Most of the internal resistance comes from the bulk and grain boundary resistance of the solid electrolyte and interfacial resistance associated with the solid electrolyte. Increasing the operating temperature, as shown in this

dissertation, decreases the internal resistance significantly. However, the ultimate solution has to be the development of a more conductive solid electrolyte.

- *Bifuncational air electrodes*: All metal-air batteries share the same problem in the bifunctional air electrodes. Any reversible metal-air batteries will require high activity and stability of the bifunctional air electrodes for ORR during discharge and OER during charge. However, ORR and OER are both sluggish, which often require the use of noble-metal catalysts, *e.g.* Pt and IrO_2. Non-noble-metal or metal-free catalysts are needed to lower the cost of the catalysts without sacrificing the cell performance. N-doped carbon materials are promising candidates as ORR catalysts for their high activity and good stability. However, since carbon is not stable at high potential, the ORR electrode needs to be decoupled from the OER electrode during charging. In this case, a free-standing carbon- and binder-free OER electrode has special advantage as the OER electrode, as shown in this dissertation. Nanostructured non-noble metal oxides directly grown onto a metal mesh substrate is an ideal strategy due to the high catalytic surface area and strong connection with the highly conductive metal substrate.

The approaches described in this dissertation have achieved considerable improvements with hybrid Li-air batteries. However, the hybrid Li-air battery is still at its infant stage. More efforts beyond this dissertation should be devoted to the development of a more conductive and stable solid electrolyte that is selective only to Li^+-ion transport, a CO_2 filter membrane on the air electrode, and dendrite-free lithium anode.

Appendix: List of Publications

1. L. Li, X. Zhao and A. Manthiram, "A hybrid rechargeable Li-air battery with phosphate buffer catholyte," *Electrochem. Commun.*, 2012, **14**, 78-81.

2. L. Li, X. Zhao, Y. Fu and A. Manthiram, "Polyprotic acid catholyte for high capacity hybrid Li-air batteries," *Phys. Chem. Chem. Phys.*, 2012, **14**, 12737-12740.

3. L. Li and A. Manthiram, "Hybrid lithium-air batteries: influence of catalyst, temperature, and solid-electrolyte conductivity on the efficiency and power density," *J. Mater. Chem. A*, 2013, **1**, 5121-5127.

4. L. Li and A. Manthiram, "O- and N-doped carbon nanoweb as metal-free catalysts for hybrid Li-air batteries," *Adv. Energy Mater.*, DOI: 10.1002/aenm.201301795 (2014)

5. L. Li, S. -H. Cai, S. Dai, and A. Manthiram, "Advanced hybrid Li-air batteries with high-performance mesoporous nanocatalysts," *Energy Environ. Sci.*, under review.

6. A. Manthiram and L. Li, "Challenges and prospects of hybrid and aqueous lithium-air batteries," *Energy Environ. Sci.*, in preparation.

7. L. Li and A. Manthiram, "Effect of constructions of the bifunctional air electrodes on the performance of hybrid Li-air batteries," in preparation.

8. L. Li, S. Liu and A. Manthiram, "Co_3O_4 nanocrystals assembled on O- and N- doped carbon nanoweb as highly efficient catalysts for hybrid Li-air batteries," in preparation.

9. L. Li, Y. Fu and A. Manthiram, "Imidazole buffered catholyte for hybrid Li-air batteries with high practical energy density," in preparation.

Reference

1. A. Manthiram, *J. Phys. Chem. Lett.*, 2011, **2**, 176-184.

2. J. Goodenough, *J. Solid State Electrochem.*, 2012, **16**, 2019-2029.

3. K. Gallagher, T. Greszler, S. Goebel, M. Mathias, V. Srinivasan, presented at the 224th ECS Meeting, San Francisco, CA, October **2013**.

4. P. Stevens, G. Toussaint, G. Caillon, P. Viaud, P. Vinatier, C. Cantau, O. Fichet, C. Sarrazin and M. Mallouki, *ECS Trans.*, 2010, **28**, 1-12.

5. M. Matsui, A. Wada, Y. Maeda, H. Ohkuma, O. Yamamoto and N. Imanishi, presented at the 224th ECS Meeting, San Francisco, CA, October **2013**.

6. *US Pat.,* 7,282,296 B2, 2007.

7. P. Hartmann, T. Leichtweiss, M. R. Busche, M. Schneider, M. Reich, J. Sann, P. Adelhelm and J. Janek, *J. Phys. Chem. C*, 2013, **117**, 21064-21074.

8. H. Wang, N. Imanishi, A. Hirano, Y. Takeda and O. Yamamoto, *J. Power Sources*, 2012, **219**, 22-28.

9. M. Ishikawa, Y. Takaki, M. Morita and Y. Matsuda, *J. Electrochem. Soc.*, 1997, **144**, L90-L92.

10. H. Kim, G. Jeong, Y.-U. Kim, J.-H. Kim, C.-M. Park and H.-J. Sohn, *Chem. Soc. Rev.*, 2013, **42**, 9011-9034.

11. L. Jörissen, *J. Power Sources*, 2006, **155**, 23-32.

12. J. Lee, B. Jeong and J. D. Ocon, *Curr. Appl. Phys.*, 2013, **13**, 309-321.

13. G. Chen, D. A. Delafuente, S. Sarangapani and T. E. Mallouk, *Catal. Today*, 2001, **67**, 341-355.

14. J. Pettersson, B. Ramsey and D. Harrison, *J. Power Sources*, 2006, **157**, 28-34.

15. S. Liu, H. Wang, N. Imanishi, T. Zhang, A. Hirano, Y. Takeda, O. Yamamoto and J. Yang, *J. Power Sources*, 2011, **196**, 7681-7686.

16. Y. Wang and H. Zhou, *J. Power Sources*, 2010, **195**, 358-361.

17. H. Li, Y. Wang, H. Na, H. Liu and H. Zhou, *J. Am. Chem. Soc.*, 2009, **131**, 15098-15099.

18. D. Aurbach, A. Zaban, A. Schechter, Y. Ein‐Eli, E. Zinigrad and B. Markovsky, *J. Electrochem. Soc.*, 1995, **142**, 2873-2882.

19. V. R. Koch and J. H. Young, *J. Electrochem. Soc.*, 1978, **125**, 1371-1377.

20. I. Yoshimatsu, T. Hirai and J. i. Yamaki, *J. Electrochem. Soc.*, 1988, **135**, 2422-2427.

21. K. M. Abraham, J. S. Foos and J. L. Goldman, *J. Electrochem. Soc.*, 1984, **131**, 2197-2199.

22. J.-I. Yamaki, I. Yamazaki, M. Egashira and S. Okada, *J. Power Sources*, 2001, **102**, 288-293.

23. S. S. Zhang and C. A. Angell, *J. Electrochem. Soc.*, 1996, **143**, 4047-4053.

24. Y. Matsuda, M. Morita, K. Yamada and K. Hirai, *J. Electrochem. Soc.*, 1985, **132**, 2538-2543.

25. K. Naoi, M. Mori, Y. Naruoka, W. M. Lamanna and R. Atanasoski, *J. Electrochem. Soc.*, 1999, **146**, 462-469.

26. Z.-i. Takehara, *J. Power Sources*, 1997, **68**, 82-86.

27. S. Shiraishi, K. Kanamura and Z.-i. Takehara, *Langmuir*, 1997, **13**, 3542-3549.

28. P. C. Howlett, D. R. MacFarlane and A. F. Hollenkamp, *Electrochem. Solid-State Lett.*, 2004, **7**, A97-A101.

29. M. Mori, Y. Naruoka, K. Naoi and D. Fauteux, *J. Electrochem. Soc.*, 1998, **145**, 2340-2348.

30. J. O. Besenhard, J. Gürtler, P. Komenda and A. Paxinos, *J. Power Sources*, 1987, **20**, 253-258.

31. M. Morita, S. Aoki and Y. Matsuda, *Electrochim. Acta*, 1992, **37**, 119-123.

32. J. K. Stark, Y. Ding and P. A. Kohl, *J. Electrochem. Soc.*, 2011, **158**, A1100-A1105.

33. S. Yoon, J. Lee, S.-O. Kim and H.-J. Sohn, *Electrochim. Acta*, 2008, **53**, 2501-2506.

34. M. Ishikawa, M. Morita and Y. Matsuda, *J. Power Sources*, 1997, **68**, 501-505.

35. F. Ding, W. Xu, G. L. Graff, J. Zhang, M. L. Sushko, X. Chen, Y. Shao, M. H. Engelhard, Z. Nie, J. Xiao, X. Liu, P. V. Sushko, J. Liu and J.-G. Zhang, *J. Am. Chem. Soc.*, 2013, **135**, 4450-4456.

36. T. Zhang, N. Imanishi, A. Hirano, Y. Takeda and O. Yamamoto, *Electrochem. Solid-State Lett.*, 2011, **14**, A45-A48.

37. R. Bashyam and P. Zelenay, *Nature*, 2006, **443**, 63-66.

38. P. Knauth, *Solid State Ionics*, 2009, **180**, 911-916.

39. http://www.ohara-inc.co.jp/en/product/electronics/licgc.html.

40. H. Aono, E. Sugimoto, Y. Sadaoka, N. Imanaka and G. y. Adachi, *J. Electrochem. Soc.*, 1989, **136**, 590-591.

41. J. Fu, *J. Mater. Sci.*, 1998, **33**, 1549-1553.

42. K. Arbi, M. Ayadi-Trabelsi and J. Sanz, *J. Mater. Chem.*, 2002, **12**, 2985-2990.

43. H. Xie, Y. Li and J. B. Goodenough, *RSC Advances*, 2011, **1**, 1728-1731.

44. Y. Li, M. Liu, K. Liu and C.-A. Wang, *J. Power Sources*, 2013, **240**, 50-53.

45. V. Thangadurai, H. Kaack and W. J. F. Weppner, *J. Am. Ceram. Soc.*, 2003, **86**, 437-440.

46. R. Murugan, V. Thangadurai and W. Weppner, *Angew. Chem. Int. Ed.*, 2007, **46**, 7778-7781.

47. E. J. Cussen, *J. Mater. Chem.*, 2010, **20**, 5167-5173.

48. V. Thangadurai and W. Weppner, *Adv. Funct. Mater.*, 2005, **15**, 107-112.

49. S. Ohta, T. Kobayashi and T. Asaoka, *J. Power Sources*, 2011, **196**, 3342-3345.

50. Y. Li, J.-T. Han, C.-A. Wang, H. Xie and J. B. Goodenough, *J. Mater. Chem.*, 2012, **22**, 15357-15361.

51. S. Stramare, V. Thangadurai and W. Weppner, *Chem. Mater.*, 2003, **15**, 3974-3990.

52. H. Geng, J. Lan, A. Mei, Y. Lin and C. W. Nan, *Electrochim. Acta*, 2011, **56**, 3406-3414.

53. P. G. Bruce, *J. Solid State Chem.*, 1982, **44**, 354-365.

54. T. T. Truong, Y. Qin, Y. Ren, Z. Chen, M. K. Chan, J. P. Greeley, K. Amine and Y. Sun, *Adv. Mater.*, 2011, **23**, 4947-4952.

55. P. He, Y. Wang and H. Zhou, *Electrochem. Commun.*, 2010, **12**, 1686-1689.

56. J. Wolfenstine and J. L. Allen, *J. Mater. Sci.*, 2008, **43**, 7247-7249.

57. T. Zhang, N. Imanishi, Y. Takeda and O. Yamamoto, *Chem. Lett.*, 2011, **40**, 668-673.

58. J. Wolfenstine, *J. Mater. Sci.*, 2010, **45**, 3954-3956.

59. L. Sebastian, R. S. Jayashree and J. Gopalakrishnan, *J. Mater. Chem.*, 2003, **13**, 1400-1405.

60. C. Galven, J. Dittmer, E. Suard, F. Le Berre and M.-P. Crosnier-Lopez, *Chem. Mater.*, 2012, **24**, 3335-3345.

61. Y. Shimonishi, A. Toda, T. Zhang, A. Hirano, N. Imanishi, O. Yamamoto and Y. Takeda, *Solid State Ionics*, 2011, **183**, 48-53.

62. Y. Sun, *Nano Energy*, 2013, **2**, 801-816.

63. S. Hasegawa, N. Imanishi, T. Zhang, J. Xie, A. Hirano, Y. Takeda and O. Yamamoto, *J. Power Sources*, 2009, **189**, 371-377.

64. Y. Shimonishi, T. Zhang, P. Johnson, N. Imanishi, A. Hirano, Y. Takeda, O. Yamamoto and N. Sammes, *J. Power Sources*, 2010, **195**, 6187-6191.

65. L. Li, X. Zhao and A. Manthiram, *Electrochem. Commun.*, 2012, **14**, 78-81.

66. P. He, Y. Wang and H. Zhou, *Chem. Commun.*, 2011, **47**, 10701-10703.

67. T. Zhang, N. Imanishi, Y. Shimonishi, A. Hirano, Y. Takeda, O. Yamamoto and N. Sammes, *Chem. Commun.*, 2010, **46**, 1661-1663.

68. T. Zhang, N. Imanishi, Y. Shimonishi, A. Hirano, J. Xie, Y. Takeda, O. Yamamoto and N. Sammes, *J. Electrochem. Soc.*, 2010, **157**, A214-A218.

69. L. Li, X. Zhao, Y. Fu and A. Manthiram, *Phys. Chem. Chem. Phys.*, 2012, **14**, 12737-12740.

70. L. Li, Y. Fu and A. Manthiram, unpublished.

71. D. R. Lide, *CRC Handbook of Chemistry and Physics*, 82nd edn., CRC Press Inc., Florida, 2001.

72. P. J. Ferreira, G. J. la O', Y. Shao-Horn, D. Morgan, R. Makharia, S. Kocha and H. A. Gasteiger, *J. Electrochem. Soc.*, 2005, **152**, A2256-A2271.

73. A. V. Virkar and Y. Zhou, *J. Electrochem. Soc.*, 2007, **154**, B540-B547.

74. Z. Luo, D. Li, H. Tang, M. Pan and R. Ruan, *Int. J. Hydrogen Energy*, 2006, **31**, 1831-1837.

75. S. Mitsushima, S. Kawahara, K.-i. Ota and N. Kamiya, *J. Electrochem. Soc.*, 2007, **154**, B153-B158.

76. T. Akita, A. Taniguchi, J. Maekawa, Z. Siroma, K. Tanaka, M. Kohyama and K. Yasuda, *J. Power Sources*, 2006, **159**, 461-467.

77. K. H. Kangasniemi, D. A. Condit and T. D. Jarvi, *J. Electrochem. Soc.*, 2004, **151**, E125-E132.

78. L. M. Roen, C. H. Paik and T. D. Jarvi, *Electrochem. Solid-State Lett.*, 2004, **7**, A19-A22.

79. Y. Li, K. Huang and Y. Xing, *Electrochim. Acta*, 2012, **81**, 20-24.

80. K. Huang, Y. Li and Y. Xing, *Electrochim. Acta*, 2013, **103**, 44-49.

81. E. Yoo, J. Nakamura and H. S. Zhou, *Energy Environ. Sci.*, 2012, **5**, 6928-6932.

82. H. He, W. Niu, N. M. Asl, J. Salim, R. Chen and Y. Kim, *Electrochim. Acta*, 2012, **67**, 87-94.

83. P. He, Y. Wang and H. Zhou, *J. Power Sources*, 2011, **196**, 5611-5616.

84. Y. Shimonishi, T. Zhang, N. Imanishi, D. Im, D. J. Lee, A. Hirano, Y. Takeda, O. Yamamoto and N. Sammes, *J. Power Sources*, 2011, **196**, 5128-5132.

85. S. Wang, S. Dong, J. Wang, L. Zhang, P. Han, C. Zhang, X. Wang, K. Zhang, Z. Lan and G. Cui, *J. Mater. Chem.*, 2012, **22**, 21051-21056.

86. E. Yoo and H. Zhou, *ACS Nano*, 2011, **5**, 3020-3026.

87. Y. Li, Z. Huang, K. Huang, D. Carnahan and Y. Xing, *Energy Environ. Sci.*, 2013.

88. Y. Wang and H. Zhou, *Chem. Commun.*, 2010, **46**, 6305-6307.

89. W. Yang, J. Salim, S. Li, C. Sun, L. Chen, J. B. Goodenough and Y. Kim, *J. Mater. Chem.*, 2012, **22**, 18902-18907.

90. Y. Wang, R. Ohnishi, E. Yoo, P. He, J. Kubota, K. Domen and H. Zhou, *J. Mater. Chem.*, 2012, **22**, 15549-15555.

91. P. G. Bruce, L. J. Hardwick and K. M. Abraham, *MRS Bull.*, 2011, **36**, 506-512.

92. G. Girishkumar, B. McCloskey, A. C. Luntz, S. Swanson and W. Wilcke, *J. Phys. Chem. Lett.*, 2010, **1**, 2193-2203.

93. K. M. Abraham and Z. Jiang, *J. Electrochem. Soc.*, 1996, **143**, 1-5.

94. J. Read, *J. Electrochem. Soc.*, 2002, **149**, A1190.

95. T. Kuboki, T. Okuyama, T. Ohsaki and N. Takami, *J. Power Sources*, 2005, **146**, 766-769.

96. T. Ogasawara, A. Debart, M. Holzapfel, P. Novak and P. G. Bruce, *J. Am. Chem. Soc.*, 2006, **128**, 1390-1393.

97. A. Débart, J. Bao, G. Armstrong and P. G. Bruce, *J. Power Sources*, 2007, **174**, 1177-1182.

98. Y. Lu and J. B. Goodenough, *J. Mater. Chem.*, 2011, **21**, 10113-10117.

99. T. Zhang, N. Imanishi, S. Hasegawa, A. Hirano, J. Xie, Y. Takeda, O. Yamamoto and N. Sammes, *J. Electrochem. Soc.*, 2008, **155**, A965-A969.

100. Y. Wang, P. He and H. Zhou, *Energy Environ. Sci.*, 2011, **4**, 4994-4999.

101. Y. Lu and R. G. Reddy, *Int. J. Hydrogen Energy*, 2011, **36**, 822-829.

102. S.-D. Yim, W.-Y. Lee, Y.-G. Yoon, Y.-J. Sohn, G.-G. Park, T.-H. Yang and C.-S. Kim, *Electrochim. Acta*, 2004, **50**, 713-718.

103. T. Zhang, N. Imanishi, S. Hasegawa, A. Hirano, J. Xie, Y. Takeda, O. Yamamoto and N. Sammes, *Electrochem. Solid-State Lett.*, 2009, **12**, A132-A135.

104. P. G. Bruce, S. A. Freunberger, L. J. Hardwick and J.-M. Tarascon, *Nat. Mater.*, 2012, **11**, 19-29.

105. R. Adams and R. L. Shriner, *J. Am. Chem. Soc.*, 1923, **45**, 2171-2179.

106. Y. Lu, J. B. Goodenough and Y. Kim, *J. Am. Chem. Soc.*, 2011, **133**, 5756-5759.

107. B. Dunn, H. Kamath and J.-M. Tarascon, *Science*, 2011, **334**, 928-935.

108. S. A. Freunberger, Y. Chen, Z. Peng, J. M. Griffin, L. J. Hardwick, F. Bardé, P. Novák and P. G. Bruce, *J. Am. Chem. Soc.*, 2011, **133**, 8040-8047.

109. W. Xu, K. Xu, V. V. Viswanathan, S. A. Towne, J. S. Hardy, J. Xiao, Z. Nie, D. Hu, D. Wang and J.-G. Zhang, *J. Power Sources*, 2011, **196**, 9631-9639.

110. D. D. Perrin, *Ionization Constants of Inorganic Acids and Bases in Aqueous Solution*, 2nd edn., Pergamon, Oxford, 1982.

111. A. J. Bard, L. R. Faulkner, *Electrochemical Methods Fundamentals and Applications*, John Wiley & Sons, Inc., New York, 2001.

112. C. E. Housecroft, A. G. Sharpe, *Inorganic Chemistry*, 2nd edn., Prentice Hall/Pearson Education, Essex, 2005.

113. J.-G. Oh, W. H. Lee and H. Kim, *Int. J. Hydrogen Energy*, 2012, **37**, 2455-2461.

114. S. Dong, X. Chen, S. Wang, L. Gu, L. Zhang, X. Wang, X. Zhou, Z. Liu, P. Han, Y. Duan, H. Xu, J. Yao, C. Zhang, K. Zhang, G. Cui and L. Chen, *ChemSusChem*, 2012, **5**, 1712-1715.

115. J. Ludwig, *J. Power Sources*, 2006, **155**, 23-32.

116. S. Zhang, X.-Z. Yuan, J. N. C. Hin, H. Wang, K. A. Friedrich and M. Schulze, *J. Power Sources*, 2009, **194**, 588-600.

117. S. Song, H. Zhang, X. Ma, Z. Shao, R. T. Baker and B. Yi, *Int. J. Hydrogen Energy*, 2008, **33**, 4955-4961.

118. F. A. Frame, T. K. Townsend, R. L. Chamousis, E. M. Sabio, T. Dittrich, N. D. Browning and F. E. Osterloh, *J. Am. Chem. Soc.*, 2011, **133**, 7264-7267.

119. S.-E. Jang and H. Kim, *J. Am. Chem. Soc.*, 2010, **132**, 14700-14701.

120. T. Cochell and A. Manthiram, *Langmuir*, 2011, **28**, 1579-1587.

121. T. Ioroi, N. Kitazawa, K. Yasuda, Y. Yamamoto and H. Takenaka, *J. Electrochem. Soc.*, 2000, **147**, 2018-2022.

122. J. Larminie and A. Dicks, *Fuel Cell Systems Explained*, 2nd edn., John Wiley & Sons, Inc., Chichester, 2003.

123. U. A. Paulus, T. J. Schmidt, H. A. Gasteiger and R. J. Behm, *J. Electroanal. Chem.*, 2001, **495**, 134-145.

124. J. Suntivich, H. A. Gasteiger, N. Yabuuchi, H. Nakanishi, J. B. Goodenough and Y. Shao-Horn, *Nat. Chem.*, 2011, **3**, 546-550.

125. K. Gong, F. Du, Z. Xia, M. Durstock and L. Dai, *Science*, 2009, **323**, 760-764.

126. L. Qu, Y. Liu, J.-B. Baek and L. Dai, *ACS Nano*, 2010, **4**, 1321-1326.

127. Y. Tang, B. L. Allen, D. R. Kauffman and A. Star, *J. Am. Chem. Soc.*, 2009, **131**, 13200-13201.

128. S. Maldonado and K. J. Stevenson, *J. Phys. Chem. B*, 2005, **109**, 4707-4716.

129. W. Wei, H. Liang, K. Parvez, X. Zhuang, X. Feng and K. Müllen, *Angew. Chem. Int. Ed.*, 2014, **53**, 1570-1574.

130. Y. Cheng, H. Zhang, C. V. Varanasi and J. Liu, *Sci. Rep.*, 2013, **3**, 3195-1 - 3195-5.

131. F. Gao, G.-L. Zhao, S. Yang and J. J. Spivey, *J. Am. Chem. Soc.*, 2012, **135**, 3315-3318.

132. Q. Li, S. Zhang, L. Dai and L.-s. Li, *J. Am. Chem. Soc.*, 2012, **134**, 18932-18935.

133. H. Kim, K. Lee, S. I. Woo and Y. Jung, *Phys. Chem. Chem. Phys.*, 2011, **13**, 17505-17510.

134. S. Shanmugam and T. Osaka, *Chem. Commun.*, 2011, **47**, 4463-4465.

135. W. Xiong, F. Du, Y. Liu, A. Perez, M. Supp, T. S. Ramakrishnan, L. Dai and L. Jiang, *J. Am. Chem. Soc.*, 2010, **132**, 15839-15841.

136. S. Guo, S. Dong and E. Wang, *ACS Nano*, 2009, **4**, 547-555.

137. Y.-C. Yong, X.-C. Dong, M. B. Chan-Park, H. Song and P. Chen, *ACS Nano*, 2012, **6**, 2394-2400.

138. Z. Liu, X. Zhang, S. Poyraz, S. P. Surwade and S. K. Manohar, *J. Am. Chem. Soc.*, 2010, **132**, 13158-13159.

139. L. Qie, W.-M. Chen, Z.-H. Wang, Q.-G. Shao, X. Li, L.-X. Yuan, X.-L. Hu, W.-X. Zhang and Y.-H. Huang, *Adv. Mater.*, 2012, **24**, 2047-2050.

140. L. Li and A. Manthiram, *J. Mater. Chem. A*, 2013, **1**, 5121-5127.

141. J. R. Pels, F. Kapteijn, J. A. Moulijn, Q. Zhu and K. M. Thomas, *Carbon*, 1995, **33**, 1641-1653.

142. R. Silva, D. Voiry, M. Chhowalla and T. Asefa, *J. Am. Chem. Soc.*, 2013, **135**, 7823-7826.

143. S.-H. Yoon, S. Lim, Y. Song, Y. Ota, W. Qiao, A. Tanaka and I. Mochida, *Carbon*, 2004, **42**, 1723-1729.

144. M. Matsumoto, M. Yamada and N. Watanabe, *Chem. Commun.*, 2005, 483-485.

145. A. Morozan, P. Jegou, S. Campidelli, S. Palacin and B. Jousselme, *Chem. Commun.*, 2012, **48**, 4627-4629.

146. T. S. Olson, S. Pylypenko, P. Atanassov, K. Asazawa, K. Yamada and H. Tanaka, *J. Phys. Chem. C*, 2010, **114**, 5049-5059.

147. L. Li, S. -H. Cai, S. Dai and A. Manthiram, unpublished.

148. A. Débart, A. J. Paterson, J. Bao and P. G. Bruce, *Angew. Chem. Int. Ed.*, 2008, **47**, 4521-4524.

149. Y.-C. Lu, Z. Xu, H. A. Gasteiger, S. Chen, K. Hamad-Schifferli and Y. Shao-Horn, *J. Am. Chem. Soc.*, 2010, **132**, 12170-12171.

150. S. A. Freunberger, Y. Chen, N. E. Drewett, L. J. Hardwick, F. Bardé and P. G. Bruce, *Angew. Chem. Int. Ed.*, 2011, **50**, 8609-8613.

151. H. Wang and K. Xie, *Electrochim. Acta*, 2012, **64**, 29-34.

152. F. Mizuno, S. Nakanishi, Y. Kotani, S. Yokoishi and H. Iba, *Electrochemistry*, 2010, **78**, 403-405.

153. R. Black, S. H. Oh, J.-H. Lee, T. Yim, B. Adams and L. F. Nazar, *J. Am. Chem. Soc.*, 2012, **134**, 2902-2905.

154. T. Sakai, T. Iwaki, Z. Ye and D. Noreus, *J. Electrochem. Soc.*, 1995, **142**, 4040-4045.

155. H. Zhou, Y. Wang, H. Li and P. He, *ChemSusChem*, 2010, **3**, 1009-1019.

156. P. W. T. Lu and S. Srinivasan, *J. Electrochem. Soc.*, 1978, **125**, 1416-1422.

157. Y. Li, Z. Huang, K. Huang, D. Carnahan and Y. Xing, *Energy Environ. Sci.*, 2013, **6**, 3339-3345.

158. G. Zhang and X. W. Lou, *Adv. Mater.*, 2013, **25**, 976-979.

159. X. Wang, J. S. Lee, Q. Zhu, J. Liu, Y. Wang and S. Dai, *Chem. Mater.*, 2010, **22**, 2178-2180.

160. X. Wang, J. S. Lee, C. Tsouris, D. W. DePaoli and S. Dai, *J. Mater. Chem.*, 2010, **20**, 4602-4608.

161. H. Jiang, Y. Su, Y. Zhu, J. Shen, X. Yang, Q. Feng and C. Li, *J. Mater. Chem. A*, 2013, **1**, 12074-12081.

162. H.-W. Liang, W. Wei, Z.-S. Wu, X. Feng and K. Müllen, *J. Am. Chem. Soc.*, 2013, **135**, 16002-16005.

163. L. Wang, A. Ambrosi and M. Pumera, *Angew. Chem. Int. Ed.*, 2013, **52**, 13818-13821.

164. P. Rasiyah, A. C. C. Tseung and D. B. Hibbert, *J. Electrochem. Soc.*, 1982, **129**, 1724-1727.

165. Y.-L. Wang, Y.-Q. Zhao, C.-L. Xu, D.-D. Zhao, M.-W. Xu, Z.-X. Su and H.-L. Li, *J. Power Sources*, 2010, **195**, 6496-6499.

166. H. Wang, Q. Gao and L. Jiang, *Small*, 2011, **7**, 2454-2459.

167. H. Chen, F. Sun, J. Wang, W. Li, W. Qiao, L. Ling and D. Long, *J. Phys. Chem. C*, 2013, **117**, 8318-8328.

168. G. Liu, X. Li, P. Ganesan and B. N. Popov, *Electrochim. Acta*, 2010, **55**, 2853-2858.

169. V. Nallathambi, J.-W. Lee, S. P. Kumaraguru, G. Wu and B. N. Popov, *J. Power Sources*, 2008, **183**, 34-42.

170. Z. Zuo, W. Li and A. Manthiram, *J. Mater. Chem. A*, 2013, **1**, 10166-10172.

171. E. Higuchi, H. Uchida and M. Watanabe, *J. Electroanal. Chem.*, 2005, **583**, 69-76.

172. N. Gavrilov, I. A. Pašti, M. Mitrić, J. Travas-Sejdić, G. Ćirić-Marjanović and S. V. Mentus, *J. Power Sources*, 2012, **220**, 306-316.

173. J. D. Wiggins-Camacho and K. J. Stevenson, *J. Phys. Chem. C*, 2011, **115**, 20002-20010.

174. S. Wang, D. Yu, L. Dai, D. W. Chang and J.-B. Baek, *ACS Nano*, 2011, **5**, 6202-6209.

Vita

Longjun Li was born in 1988, in Nanchang, China. He grew up in the same city until he attended Huazhong University of Science and Technology (HUST) in Wuhan in 2006. He obtained his B. Eng. in Materials Science and Engineering in 2010. Then he joined professor Manthiram's group at the University of Texas at Austin (UT Austin) in the same year. His research at UT Austin focuses on the design and development of hybrid Li-air batteries.

Email Address: longjunli@utexas.edu

This dissertation was typed by the author.